

1

[ATLAS Semivisible Jets]

2

[Elena Laura Busch]

3

Submitted in partial fulfillment of the  
requirements for the degree of  
Doctor of Philosophy  
under the Executive Committee  
of the Graduate School of Arts and Sciences

4

5

6

7

8

COLUMBIA UNIVERSITY

9

2024

10

© 2024

11

[Elena Laura Busch]

12

All Rights Reserved

13

## **Abstract**

14

[ATLAS Semivisible Jets]

15

[Elena Laura Busch]

16

Abstract of dissertation (place-holder).

## Table of Contents

18	Acknowledgments . . . . .	iv
19	Dedication . . . . .	v
20	Introduction or Preface . . . . .	1
21	<b>I Theory</b>	<b>2</b>
22	Chapter 1: The Standard Model . . . . .	3
23	1.1 Phenomenology: Particles and Forces . . . . .	3
24	1.1.1 Particles . . . . .	3
25	1.1.2 Forces . . . . .	5
26	1.2 QCD and Jets . . . . .	7
27	1.3 Symmetries . . . . .	8
28	1.3.1 Spontaneous Symmetry Breaking and The Higgs Mechanism . . . . .	9
29	1.4 Experimental Validation of the Standard Model . . . . .	10
30	1.5 Limitations of the Standard Model . . . . .	11
31	Chapter 2: Physics Beyond the Standard Model . . . . .	13
32	2.1 Hidden Valley Models . . . . .	13
33	2.2 Dark QCD . . . . .	14

34	2.3 Semi-visible Jets . . . . .	15
35	<b>II Experiment</b>	<b>17</b>
36	Chapter 3: The Large Hadron Collider . . . . .	18
37	3.1 Accelerator Physics . . . . .	19
38	3.1.1 The Journey of a Proton . . . . .	19
39	3.1.2 Magnets . . . . .	20
40	3.2 Luminosity . . . . .	21
41	3.3 LHC Timeline . . . . .	24
42	Chapter 4: The ATLAS Detector . . . . .	26
43	4.1 Coordinate System and Geometry . . . . .	26
44	4.2 Inner Detector . . . . .	28
45	4.2.1 Pixel Detector . . . . .	28
46	4.2.2 Semiconductor Tracker . . . . .	29
47	4.2.3 Transition Radiation Tracker . . . . .	29
48	4.3 Calorimeters . . . . .	30
49	4.3.1 Liquid Argon Calorimeter . . . . .	31
50	4.3.2 Tile Calorimeter . . . . .	34
51	4.4 Muon Spectrometer . . . . .	35
52	4.5 Magnet System . . . . .	37
53	4.6 Forward Detectors . . . . .	38
54	4.7 Trigger and Data Acquisition . . . . .	39

55	Chapter 5: Particle Reconstruction and Identification . . . . .	41
56	5.1 Inner Detector Tracks . . . . .	41
57	5.2 Photons and Electrons . . . . .	42
58	5.3 Muons . . . . .	44
59	5.4 Jets . . . . .	46
60	5.4.1 Calorimeter Clusters . . . . .	47
61	5.4.2 Particle Flow Algorithm . . . . .	48
62	5.4.3 Jet Clustering . . . . .	49
63	5.4.4 Ghost Track Association . . . . .	52
64	5.5 Missing Transverse Energy . . . . .	53
65	<b>III Search</b>	<b>55</b>
66	Chapter 6: Monte Carlo and Data . . . . .	56
67	6.1 Data . . . . .	56
68	6.2 Simulation . . . . .	57
69	6.2.1 Simulated Backgrounds . . . . .	57
70	6.2.2 Signal Simulation . . . . .	58
71	Chapter 7: Machine Learning Tools . . . . .	61
72	7.1 Introduction . . . . .	61
73	7.1.1 Particle Flow Network (Supervised) . . . . .	62
74	7.1.2 ANTELOPE (Semi-supervised) . . . . .	72
75	Chapter 8: Analysis Strategy . . . . .	79

76	8.1 Preselection . . . . .	79
77	8.2 SVJ Fit and Discovery Analysis Strategies . . . . .	81
78	8.3 Analysis Regions . . . . .	85
79	8.3.1 Control and Validation Regions . . . . .	85
80	8.3.2 Signal Region . . . . .	87
81	8.4 Background Estimation . . . . .	88
82	8.5 Fit Strategy and Validation . . . . .	90
83	8.5.1 SVJ Fit Strategy . . . . .	90
84	8.5.2 Discovery Strategy) . . . . .	101
85	Chapter 9: Results . . . . .	106
86	Conclusion or Epilogue . . . . .	107
87	References . . . . .	111
88	Appendix A: Trigger Studies . . . . .	117
89	Appendix B: Machine Learning Approaches . . . . .	121
90	B.1 Unsupervised: AE vs. ANTELOPE . . . . .	121
91	B.2 PFN Optimality Checks . . . . .	122
92	B.3 Supervised: BDT vs. PFN . . . . .	125
93	B.4 Supervised: Variable Correlations . . . . .	125
94	B.5 Single Jet vs Jet System ML Approach . . . . .	127
95	B.6 PFN Training Composition . . . . .	128

96	B.7 $E_T^{miss}$ and $E_T^{miss}\phi$ Shapes . . . . .	131
97	B.7.1 NCB Preselection . . . . .	131
98	B.7.2 TileCal Correction . . . . .	133
99	Appendix C: Truth Studies . . . . .	136
100	C.1 Jet dR Matching . . . . .	136

101

## List of Figures

102	1.1	Diagram of the 17 particles comprising the Standard Model . . . . .	4
103	1.2	Fundamental particle interactions of the three fundamental forces described by the	
104		Standard Model [2]. . . . .	6
105	1.3	An example Feynmann diagram of jet production . . . . .	7
106	1.4	An illustration of the “hat shaped” potential of the Higgs field, resulting in a non-	
107		zero vacuum expectation value. . . . .	9
108	2.1	Illustration of the hidden valley potential. . . . .	14
109	2.2	The massive mediator particle $Z'$ of the s-channel realization of a HV model . . .	14
110	3.1	The LHC accelerator complex at CERN [29] . . . . .	20
111	3.2	The octants of the LHC and location of various beam activities [28]. Stars indicate	
112		the locations of beam collisions, and the associated detectors recording the	
113		outcome of those collisions. . . . .	21
114	3.3	(Left) Total integrated luminosity over the course of Run 2. (Right) Average num-	
115		ber of $pp$ interactions per bunch crossing in Run 2. Each curve is weighted by the	
116		integrated luminosity for the year. . . . .	23
117	3.4	Timeline of LHC and HL-LHC activities [31]. Integrated luminosity estimates are	
118		approximate, and not reflective of the exact amount delivered to each experiment. .	25
119	4.1	ATLAS coordinate system and geometry . . . . .	28
120	4.2	A 3D visualization of the structure of the ID in the barrel region [35] . . . . .	29
121	4.3	ATLAS calorimetery system [36] . . . . .	30

122	4.4	Diagram of a segment of the EMB, demonstrating the accordion plate arrangement [37] . . . . .	32
123			
124	4.5	A LAr pulse as produced in the detector (triangle) and after shaping (curve) [37] . . . . .	33
125			
126	4.6	Readout gap structure in HEC [37] . . . . .	33
127			
128	4.7	TileCal wedge module [40] . . . . .	35
129			
130	4.8	Cross section view of the muon spectrometer system [41] . . . . .	36
131			
132	4.9	Layout of the barrel and endcap toroid magnets [34] . . . . .	38
133			
134	5.1	Graphic illustrating the various objects and high level features identified by ATLAS object reconstruction, and their interaction with different systems of the ATLAS detector [44] . . . . .	42
135			
136	5.2	Track reconstruction seeding, finding and fitting illustration [45] . . . . .	43
137			
138	5.3	Three types of EM object candidates [47]. . . . .	44
139			
140	5.4	Four types of muon track candidates [49]. . . . .	46
141			
142	5.5	The fragmentation and hadronization processes undergone by a quark produced in a proton-proton collision [51]. . . . .	47
143			
144	5.6	A flow chart illustrating the particle flow algorithm progression [56]. . . . .	50
145			
146	5.7	A comparison of jet clustering with four different jet algorithms. The anti- $k_t$ algorithm is observed to create the most conical jets, where the shape of the jet is immune to the presence of soft radiation [52]. . . . .	51
147			
148	5.8	A comparison of MC simulation and data for $Z \rightarrow \mu\mu$ events where real $E_T^{\text{miss}} = 0$ [63]. The resolution of the missing energy in the transverse ( $x - y$ ) plane is observed to increase with increasing total $\sum E_T$ . . . . .	54
149			
150	6.1	The transverse momentum slices of the QCD MC simulation, overlayed to show how they come together to create a smooth distribution (left) once weighted properly. The original unweighted distribution is shown on the right, illustrating the enhanced statistics for the high $p_T$ range. . . . .	58
151			

148	6.2	Background processes relevant to the SVJ signal. The agreement between the black line (data) and grey line (all MC processes combined) illustrates that this collection of background processes is sufficient to model the expected $E_T^{\text{miss}}$ in the selected data events. . . . .	59
152	7.1	The Energy/Particle Flow Network concept, from Ref. [69]. . . . .	63
153	7.2	An annotated diagram of the PFN architecture. $y$ and $\phi$ represent geometric in- formation for the input particles, $z$ represents energy information, and PID encom- passes any other particle ID information in the input. . . . .	63
156	7.3	A illustration of the expected dijet behavior of semi-visible jets, where one jet is closely aligned with $E_T^{\text{miss}}$ . . . . .	64
158	7.4	Illustration of track coordinates $d_0$ and $z_0$ . . . . .	65
159	7.5	Distributions of the track multiplicity in the leading and subleading jets, comparing signal and background PFN training samples. . . . .	65
161	7.6	A diagram demonstrating how the two jet system is rotated in $(\phi, \eta)$ . . . . .	66
162	7.7	The 6 PFN track variables in background MC and signal MC. There are some differences between signal and background, but the track kinematics are largely similar. . . . .	66
165	7.8	The 6 PFN track variables in data and background MC, after the scaling and ro- tation procedure is applied. There is excellent modeling of the data by the MC within the track variables. The slight discrepancy in the phi distribution is due to the modeling of dead TileCal cells by the QCD MC, which will be discussed in Chapter 8. The level of discrepancy is determined to be within tolerance given that the final result will be data driven and the QCD model is used in the PFN training only. . . . .	67
172	7.9	PFN score for background MC, data, and signal, comparing a PFN training on QCD-only vs all-background MC samples. The average AUC for the QCD-only training (left) is 0.93, while the average AUC for the mixed background training (right) is 0.84. The sensitivity estimate across the grid is better for the QCD-only training - from the distribution we can conclude that this is because the sensitivity to MET enhanced signals is greatly reduced. . . . .	69
178	7.10	PFN architecture loss during training as a function of epoch (left) and the evaluated loss over the signal and background (right). . . . .	69

180	7.11 ROC the PFN score for combined signal (true positive) and QCD background (false positive). . . . .	70
182	7.12 AUC from the PFN score for each signal in the SVJ grid, shown versus the QCD- only training sample. . . . .	71
184	7.13 PFN score for two signals and the total background MC (top), and between data and MC (bottom). The difference between data and MC efficiency is minimal (< 5%). . . . .	71
187	7.14 A visual representation of the 64 PFN latent space variables which create the input of the VAE component of ANTELOPE. The left shows a 2D histogram of the PFN latent space index (0-63) versus the value assumed by that index. The right shows 1D histograms of two particular PFN latent space variables. . . . .	73
191	7.15 An annotated diagram of the ANTELOPE architecture. . . . .	74
192	7.16 ANTELOPE architecture loss during training as a function of epoch. . . . .	75
193	7.17 ANTELOPE score distribution comparing data and the total background MC (left), with good agreement observed between data and simulated background, and com- paring all background MC to signals (right), revealing good discrimination power. . . . . .	76
197	7.18 AUC from the ANTELOPE score for each signal in the SVJ grid. . . . .	77
198	7.19 Comparing data and the alternate signal models for the PFN score (left) and AN- TELOPE score (right). The emerging jet signal is an example of the gain of the model-independent ANTELOPE approach, where it has a bimodal shape in PFN score but is clearly tagged as anomalous by ANTELOPE. . . . .	78
202	7.20 Comparing data and the alternate signal models in terms of sensitivity ( $S/\sqrt{B}$ ) for the PFN and ANTELOPE tools, applying the selection that is used in the analysis. The ANTELOPE network is found to provide significant added sensitivity to alter- nate signals such as the gluino → R-hadron and emerging jets, which have higher $E_T^{\text{miss}}$ than the SVJs. . . . .	78
207	8.1 Preselection cutflow for data (left) and signal (right). . . . .	80
208	8.2 Energy and momentum analysis variables at preselection, for data, all background MC and representative signal models. $m_T$ is the key fit variable, and this plot illus- trates the smoothly falling background in comparison to the resonant shape of the signals. $m_T$ is further illustrated in Figure 8.9. . . . .	82

212	8.3 Orientation analysis variables at preselection, for data, all background MC and 213 representative signal models. While $\Delta\phi(E_T^{\text{miss}}, j)$ variables are not used explicitly 214 in the analysis flow, they help create a picture of the event. . . . .	83
215	8.4 Flow of analysis selections, regions, and background estimation/validation fitting 216 strategy. . . . .	84
217	8.5 Distributions of the subleading jet width <b>jet2width</b> in data vs. background MC 218 and signals at preselection (left) and background vs. representative signal models 219 following the PFN score selection (right). Background MC comprises the sam- 220 ples listed in Appendix ???. Demonstrates that jet2width remains a discriminating 221 variable after ML tool selection is made. . . . .	85
222	8.6 2D plots revealing correlations between jet2width and $m_T$ (left), jet2width and ML 223 score (middle), and $m_T$ with ML score (right). For the top row, the ML score is 224 the PFN score, and for the bottom three, the ML score is the ANTELOPE score. 225 Minimal correlations are observed and are shown to not sculpt $m_T$ , validating these 226 variables for analysis region construction and statistical treatment. . . . .	86
227	8.7 $m_T$ in simulation across the CR, VR, and SR for both PFN (left) and ANTELOPE 228 (right) selections. . . . .	87
229	8.8 Definition of CR, VR, and SR regions using JET2WIDTH and the PFN score, along 230 with the population of each region in data statistics for the PFN (top) and ANTE- 231 LOPE (bottom) analyses. . . . .	88
232	8.9 The resonant shape of the SVJ signals in $m_T$ , in contrast to the smoothly falling 233 $m_T$ background. The high $R_{inv}$ signals (right) boast a wider shape, making them 234 more difficult to detect, while the low $R_{inv}$ signals(left) produce a more narrow 235 resonance in $m_T$ . . . . .	89
236	8.10 Post-fit parameters for the PFN CR and VR. . . . .	90
237	8.11 Background-only $m_T$ fits using representative MC in the CR (left), VR (middle), 238 and SR (right). . . . .	91
239	8.12 Background-only $m_T$ fits using data in orthogonal but statistically identical samples 240 to the SR, obtained by downsampling the CR/VR statistics, for the CR (top) and 241 VR (bottom). . . . .	92
242	8.13 Background-only $m_T$ fits using data in the full statistics CR and VR regions. . . . .	92
243	8.14 $m_T$ distribution in the data CR, before (left) and after (right) smoothing. . . . .	93
244	8.15 $p$ -value histograms from 500 fits to Asimov data in the CR. . . . .	93

245	8.16 Example S+B fits on background only spectrum (without systematics) for a variety 246 of signal points. . . . .	94
247	8.17 Example S+B fits on a background $m_T$ spectrum with injected signal from the point 248 ( $2500 \text{ GeV}$ , $R_{inv}=0.2$ ). . . . .	95
249	8.18 Linearity of fitted vs. injected signal across $m_T$ , for signal points with $R_{inv}=0.2$ , 250 0.4, 0.6, and 0.8, with several $Z'$ masses (2500 GeV, 3500 GeV, and 5000 GeV top 251 to bottom) for a single CR template with no systematics. . . . .	96
252	8.19 Spurious signal at a variety of injected values (1, 2, and $5\sigma$ significant), for all 253 signal points in the grid, $R_{inv}=0.2$ (top left), 0.4 (top right), 0.6 (bottom left), and 254 0.8 (bottom right). i . . . . .	98
255	8.20 $S_{\text{spur}}/\sigma_{\text{fit}}$ at a variety of injected values (1, 2, and $5\sigma$ significant), for all signal 256 points in the grid, $R_{inv}=0.2$ (top left), 0.4 (top right), 0.6 (bottom left), and 0.8 257 (bottom right). i . . . . .	99
258	8.21 95% C.L. upper limits for signal models across $Z'$ mass, for four different $R_{inv}$ frac- 259 tions, from the CR region (without systematics). . . . .	100
260	8.22 Post-fit parameters for the ANTELOPE CR and VR. . . . .	101
261	8.23 Post-fit function and residuals for the ANTELOPE CR and VR. . . . .	102
262	8.24 Example determinations of the 60% mass window means for several signal points. .	103
263	8.25 Signal mass resolution for $m_T$ binning for the signal grid in ( $R_{inv}$ , mass) space. . .	103
264	8.26 $m_T$ bins based on the signal mass resolution and the minimum 100 GeV width 265 requirement, for each $R_{inv}$ signal category. . . . .	104
266	8.27 BumpHunter fits on the ANTELOPE $m_T$ spectra for both the CR and VR. In 267 a signal-depleted region, good agreement with the background estimation is ob- 268 served. . . . .	105
269	8.28 BumpHunter p-values extracted for 100 Asimov toys for both the ANTELOPE 270 CR (top) and VR (bottom) showing the highest (left) and lowest (right) p-value 271 fits. The number of events in the histogram deviates from 100 based on failed 272 background-only fits. . . . .	105
273	A.1 Trigger yield and efficiency for both the MET trigger and small-R jet trigger ap- 274 proach. Each entry represent a signal point, labelled by the $Z'$ mass and the 275 $R_{inv}$ fraction. . . . .	117

276	A.2 The factor of improvement in $S/\sqrt{B}$ for each trigger method compared to the un-triggered case. . . . .	118
277		
278	A.3 The ratio of $S/\sqrt{B}$ of jet trigger over $E_T^{\text{miss}}$ trigger selection. . . . .	118
279		
280	A.4 Analysis variables where high $R_{inv}$ signals a clearly distinct from background and low $R_{inv}$ variables. On the contrary, leading jet $p_T$ is one of the only variables where low $R_{inv}$ signals are distinct from background. . . . .	120
281		
282	A.5 OR of jet and $E_T^{\text{miss}}$ triggers. . . . .	120
283		
284	B.1 . . . . .	121
285		
286	B.2 . . . . .	122
287		
288	B.3 AUC from the PFN score for each signal in the SVJ grid, shown versus the QCD-only training sample (top) and the total MC background (bottom). Note the three missing points will be added shortly - they were delayed due to a DAOD production mistake. . . . .	123
289		
290	B.4 Comparison of PFN AUC (top), SIC (middle), and sensitivity in the $m_T$ mass window (bottom) for a single PFN model (left) vs. two models, trained on $R_{inv} < 0.5$ and $> 0.5$ separately. . . . .	124
291		
292	B.5 Preferred cuts on the PFN score for each point in the grid, comparing the effect of adding the NCB preselection. . . . .	125
293		
294	B.6 Scans done to check for optimality of PFN training parameters. . . . .	126
295		
296	B.7 . . . . .	126
297		
298	B.8 $\phi$ orientation variables in the CR and VR . . . . .	127
299		
300	B.9 Correlation between $\phi$ orientation variables and PFN score . . . . .	128
301		
302	B.10 $\phi$ Performance comparison between single jet and jet system ML approach . . . . .	129
303		
304	B.11 $\phi$ Comparison in the AUC score across the grid for the mixed background strategy vs the QCD only strategy. The bottom table highlights that the QCD only strategy gives superior sensitivity across the signal grid. . . . .	130
305		
306	B.12 $E_T^{\text{miss}}$ in data before and after Tight event cleaning is applied. . . . .	131
307		
308	B.13 $E_T^{\text{miss}}$ vs jet1 $p_T$ in data before and after Tight event cleaning is applied. . . . .	132
309		

304	B.14 $\eta$ vs $\phi$ for leading and subleading jets, before and after the application of tight 305 cleaning. . . . .	132
306	B.15 Added NCB preselection and impact on $E_T^{\text{miss}}$ shape. . . . .	133
307	B.16 NCB preselection impact on data and signal yields. . . . .	134
308	B.17 Impact of tight cleaning and non-collision background preselection. . . . .	135
309	B.18 $E_T^{\text{miss}}\phi$ in data, before (left) and after (right) application of the TileCal correction 310 tool. . . . .	135
311	C.1 Index of jets truth matched (by requirement of $\Delta R < 0.4$ ) with dark quark. . . . .	136
312	C.2 Percent of jets with $\Delta R(j, E_T^{\text{miss}}) < 0.4$ comparing two jet identification strategies. 313 Leading and subleading jets are seen to be the better metric for identifying jets 314 associated with the dark quark decay. . . . .	137

## List of Tables

316	6.1 Fixed parameters in the Pythia8 HV model . . . . .	60
317	6.2 Values for $m_{dark}$ . . . . .	60
318	6.3 Mass points and cross sections of the SVJ search signal grid . . . . .	60

319

## Acknowledgements

320        Insert your acknowledgements text here. This page is optional, you may delete it if not  
321        needed.

322

## **Dedication**

323

Dedicated to my friends and family

324

## **Introduction or Preface**

325        Insert your preface text here if applicable. This page is optional, you may delete it if not  
326        needed. If you delete this page make sure to move page counter comment in thesis.tex to correct  
327        location.

328

## **Part I**

329

## **Theory**

## Chapter 1: The Standard Model

332 The Standard Model of particle physics is a universally accepted framework which explains  
 333 the interactions of fundamental particles. All known fundamental particles, outlined in Figure  
 334 1.1, are represented in the Standard Model. The model describes three of the four known forces:  
 335 the electromagnetic force, the weak force, and the strong force. Gravity, the fourth fundamental  
 336 force, is not addressed by the Standard Model. The Standard Model was primarily developed over  
 337 the course of the 1960s and 1970s, by combining the work of many physicists into one coherent  
 338 model. The Standard Model has been established as a well-tested theory by decades of experimen-  
 339 tal physics research.

340 This chapter will seek to introduce the phenomenology and mathematical foundations of the  
 341 Standard Model, and present the supporting experimental evidence. Phenomenon which are unex-  
 342 plained by the Standard Model such as gravity will be considered at the end of the chapter, leading  
 343 to an exploration of theories beyond the Standard Model in the subsequent chapter.

344 **1.1 Phenomenology: Particles and Forces**

345 **1.1.1 Particles**

346 A classic representation of the particles comprising the Standard Model is shown in Figure  
 347 1.1. The two primary particles classes are bosons (gauge bosons and the scalar Higgs boson) and  
 348 fermions (leptons and quarks). The bosons are carriers of fundamental forces, while the fermions  
 349 are the building blocks of matter. Fermions are sorted into three *generations*, and each fermion is  
 350 identified by a unique *flavor*.

351 Each entry in the table in Figure 1.1 is accompanied by 3 characteristic numbers: mass, charge,  
 352 and spin. The mass of each particle is determined to limited precision by experimental observation,

## Standard Model of Elementary Particles

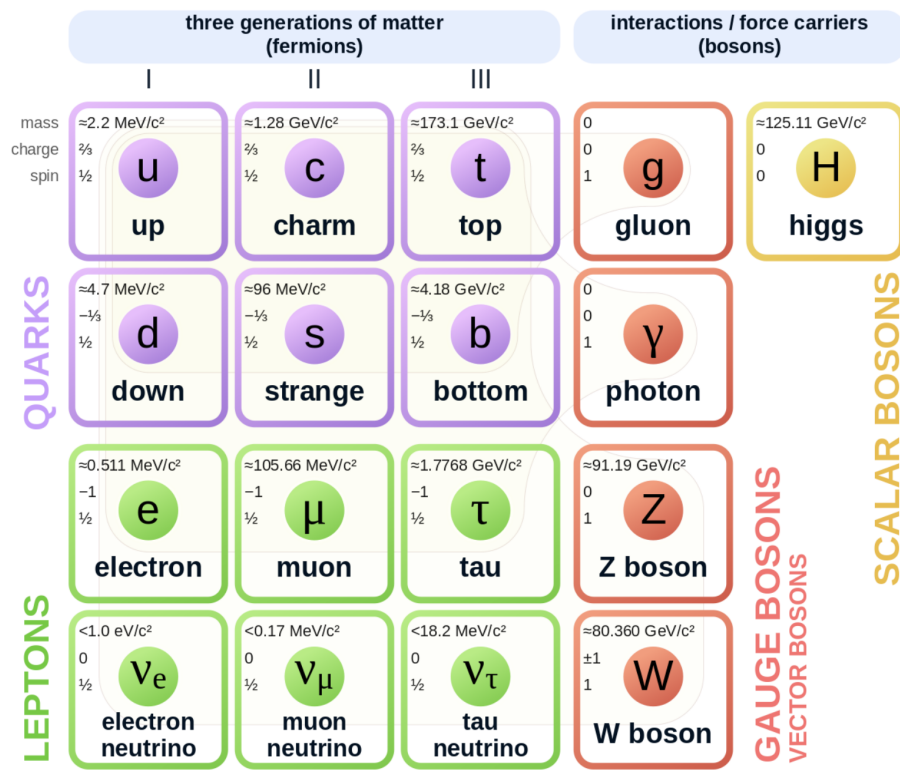


Figure 1.1: Diagram of the 17 particles comprising the Standard Model

353 with the exception of photons and gluons which are known to be massless. Charge refers to the  
354 electromagnetic charge, which is integer for leptons and fractional for quarks. Spin is an intrinsic  
355 form of angular momentum carried by fundamental particles; all fermions have half integer spin,  
356 while bosons have integer spin.

357 Each particle is also known to have an *antiparticle*. Each antiparticle has the same mass but the  
358 opposite charge of their Standard Model counter part; for example, the antiparticle of the electron  
359 is the positron, which has all the same properties but a positive charge. The photon, Z boson,  
360 and Higgs are each their own antiparticle. The nature of antineutrinos is an open question driving  
361 neutrino physics research, as it is not currently known whether neutrinos are their own antiparticle.

362 1.1.2 Forces

363 The three fundamental forces explained by the Standard Model are the electromagnetic force,  
364 the strong force, and the weak force. The photon is the carrier of the electromagnetic force, which  
365 dictates the nature of interactions between electrically charged particles, and is widely covered by  
366 introductory physics courses. The electromagnetic force has an infinite interaction range, a result  
367 of the massless and non-self interaction nature of the photon. The electromagnetic interaction is  
368 described by the theory of quantum electrodynamics (QED).

369 The weak force gives rise to atomic radiation and decay. It allows for the processes of beta  
370 decay, which enables conversion between neutrons and protons within the nucleus of an atom. In  
371 the process of beta decay, a proton decays into a neutron, a positron, and a neutrino; or, a neutron  
372 decays into a proton, an electron and an antineutrino. The weak interaction allows for quark flavor  
373 mixing, the which enables beta decay. The  $W^+$ ,  $W^-$ , and  $Z^0$  are the force carriers of the weak force.  
374 The effective range of the weak force is limited to subatomic distances, as a result of the massive  
375 nature of the mediator bosons. The unified theory of the electroweak interaction posits that at high  
376 enough energies the electromagnetic interaction and the weak force merge into the same force.  
377 This threshold is termed the unification energy and calculated to be about 246 GeV [1].

378 The strong force confines quarks into hadron particles, such as protons and neutrons. The

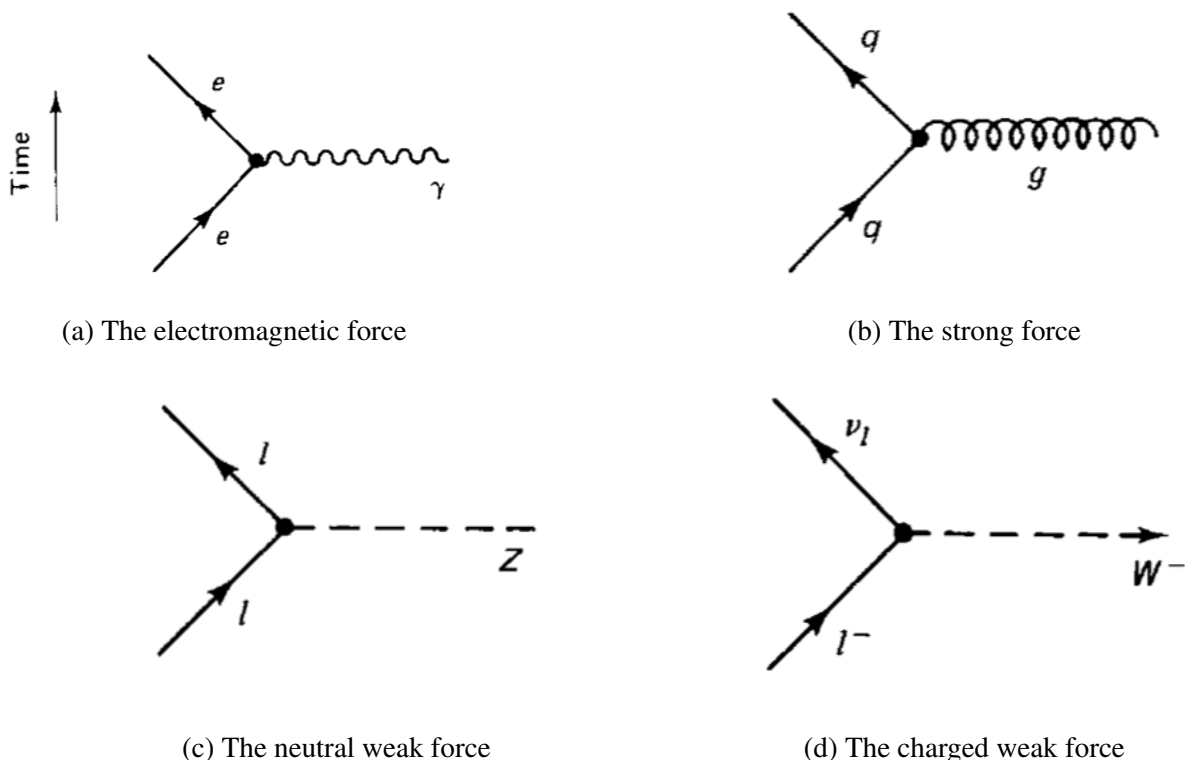


Figure 1.2: Fundamental particle interactions of the three fundamental forces described by the Standard Model [2].

379 strong force also allows for the creation of atomic nuclei by binding protons and neutrons together,  
380 and is generally referred to as the “nuclear force” in this context. The gluon is the mediator of  
381 the strong force, which is a short-range force which acts at subatomic distances on the order of  
382  $10^{-15}$  m. At this range, the strong force is about 100x as strong as the electromagnetic force,  
383 which allows for the creation of positively charged nuclei [2]. The strong force is described by the  
384 theory of quantum chromodynamics (QCD). In the same way that QED dictates the interaction of  
385 electrically charges particles, QCD dictates the interactions of *color-charged* particles. Due to the  
386 particular importance of QCD in this thesis, this topic will be explored in detail in section 1.2.

The fundamental Feynmann diagram for each of the three forces discussed here is depicted in Figure 1.2. The fourth fundamental force, gravity, is not currently explained by any known mechanism within the Standard Model.

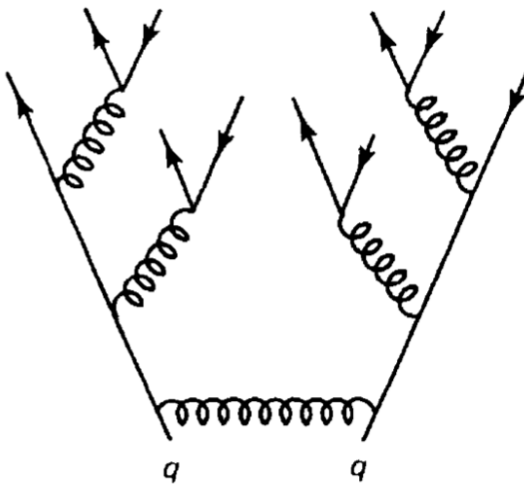


Figure 1.3: An example Feynmann diagram of jet production

## 390 1.2 QCD and Jets

391 While there is only one type of electric charge, there are three types of color charge; red, green,  
 392 and blue. In the process  $q \rightarrow q + g$ , the color of the quark can change. In order to conserve color  
 393 charge, gluons are bicolored, and always carry some positive color charge and some negative color  
 394 charge.

395 Color charged particles can only exist in bound states which result in a neutral total color  
 396 charge, a principle known as confinement. This requires that quarks and gluons exist in group  
 397 states known as hadrons; either mesons in the case of two quarks or baryons in the case of three  
 398 quarks. When a quark is separated from a hadron, confinement dictates that other colored objects  
 399 are produced around the quark to obey confinement. An example of this process is shown in  
 400 Figure 1.3. This ensemble of objects, generally a mixture of quarks and gluons, is termed a *jet*.  
 401 Jets are among the most common phenomenon observed by detectors at hadron colliders, and their  
 402 complex structure makes them a key focus of many physics analyses.

403    **1.3 Symmetries**

404    The Standard Model is a renormalizable quantum field theory that obeys the local symmetry

405     $G_{SM}$ :

$$G_{SM} = SU(3)_C \times SU(2)_L \times U(1)_Y. \quad (1.1)$$

406    The  $SU(3)_C$  symmetry component represents the non-Abelian gauge group of QCD. There  
407    are 8 generators for the  $SU_C(3)$  group which correspond to 8 types of gluon, each representing a  
408    different superposition of color charge [3]. The  $SU(2)_L \times U(1)_Y$  symmetry group represents the  
409    electroweak sector of the Standard Model, which can be spontaneously broken into the electromag-  
410    netic and weak sectors. There are 4 generators for this group, which correspond to four massless  
411    gauge bosons  $W^1$ ,  $W^2$ ,  $W^3$ , and  $B$ . From these massless gauge bosons are formed the massive  
412    mediators of the weak force, the  $W^-$ ,  $W^+$  and  $Z^0$  bosons, and the massless electromagnetic force  
413    carrier, the photon  $\gamma$ . Spontaneous symmetry breaking and the process by which gauge bosons  
414    acquire mass will be addressed in section 1.3.1.

415    Noether's theorem [4] stipulates that any continuous symmetry is associated with a conserved  
416    quantity. In the Standard Model, this means that the  $SU(3)_C$  symmetry gives rise to conservation of  
417    color charge. The  $SU(2)_L \times U(1)_Y$  symmetry gives rise to conservation of electromagnetic charge.  
418    Conservation of spin results from the Poincaré symmetry described by the theory of special rela-  
419    tivity, which combined with Noether's theorem gives us the conservation of energy, momentum,  
420    and angular momentum.

421    The SM Lagrangian is invariant under  $CPT$  symmetry, or charge, parity, and time reversal.  
422    Charge conjugation ( $C$ ) transform a particle into its corresponding antiparticle by reversing the  
423    charge and other quantum numbers. Parity conjugation ( $P$ ) reverses spatial coordinates, which  
424    transforms left-handed particles into right-handed particles and vice-versa. Time reversal ( $T$ ) is  
425    the theoretical process of reversing time. The  $L$  subscript in the  $SU(2)_L$  group indicates that this  
426    symmetry only applies to left-handed fermions. As a result, the  $W^{1,2,3}$  gauge bosons of  $SU(2)_L$

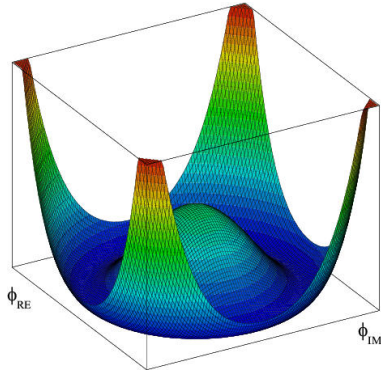


Figure 1.4: An illustration of the “hat shaped” potential of the Higgs field, resulting in a non-zero vacuum expectation value.

only interact with left handed particles, a process which maximally violates P-symmetry in the weak force. A small amount of the CP symmetry violation is also observed in the Standard Model, through the decays of strange flavored mesons [5] and  $b$ -mesons [6]. The CPT theorem posits that the violation of CP symmetry implies that T-symmetry must also be violated, so that CPT is a preserved symmetry.

### 1.3.1 Spontaneous Symmetry Breaking and The Higgs Mechanism

Spontaneous symmetry breaking is the process by which a Lagrangian obeys a symmetry at high energies, but exhibits asymmetric behavior at lower energies. The electroweak symmetry group is spontaneously broken as  $SU(2)_L \times U(1)_Y \rightarrow U(1)_{EM}$ . The quantity conserved by the  $SU(2)_L$  symmetry is weak isospin  $T_{1,2,3}$ , while the quantity conserved by  $U(1)_Y$  symmetry is weak hypercharge  $Y$ . Below very high energies, the presence of the Higgs field causes the electroweak symmetry to break. The Higgs field is a scalar field which forms a complex doublet of the  $SU(2)$  symmetry group, with four degrees of freedom. The shape of the Higgs field potential, shown in Figure 1.4, results in a ground state with a non-zero vacuum expectation value; thus the Higgs field takes a non-zero value throughout all space, which breaks the symmetry of the weak isospin  $SU(2)$  group.

The interaction with the Higgs field mixes the four massless gauge bosons  $W^{1,2,3}$  and  $B$ . Three Higgs field degrees of freedom mix with the massless gauge bosons, resulting in three massive

445 gauge bosons  $W^-$ ,  $W^+$  and  $Z^0$ . The massless photon  $\gamma$  is created from the components of the  
446 massless gauge bosons which do not interact with the Higgs field. The scalar Higgs boson arises  
447 from the one unmixed degree of freedom the Higgs field. Spontaneous symmetry breaking also  
448 violates the conservation of weak isospin and weak hypercharge, leaving only electromagnetic  
449 charge ( $Q = T_3 + \frac{1}{2}Y$ ) as a conserved quantity associated with the  $U(1)_{EM}$  symmetry.

## 450 1.4 Experimental Validation of the Standard Model

451 The theoretical framework of the Standard Model coalesced into a unified theory in the mid-  
452 20th century. A cascade of discoveries providing empirical evidence for the model followed  
453 closely. In the 1960s, three quarks (up, down and strange) and four leptons (electron, muon,  
454 and their associated neutrinos) were the known particulate building blocks of matter and the Stan-  
455 dard Model. The discovery of the charm quark in 1974, through the observation of the  $J/\psi$  meson  
456 [7][8], confirmed the existence of a fourth quark flavor. The discovery of the  $\tau$  in 1975 [9] provided  
457 the first evidence of a 3rd generation of matter. This was quickly followed by the observation of  
458 the  $\Upsilon$  meson in 1977 [10], which provided evidence for the existence of a fifth quark, the  $b$  quark  
459 (bottom, or beauty). The existence of a 3rd generation of fermion also explained the observation  
460 of CP violation in the weak force, as it allowed for the addition of a complex phase in the CKM  
461 matrix (a unitary matrix which describes flavor mixing in the weak interaction). The top quark  
462 ( $t$ ) and tau neutrino ( $\nu_\tau$ ) were predicted at this point as the final building blocks of three complete  
463 generations of fermions, and they were discovered by experimental observation around the turn of  
464 the 21st century [11] [12] [13].

465 The W and Z bosons were predicted by the Standard Model, but to observe them required the  
466 construction of a particle accelerator powerful enough to produce them. They were finally observed  
467 at CERN in 1983 by the UA1 and UA2 experiments [14] [15] at the newly constructed Super Proton  
468 Synchrotron (SPS). Their masses were observed to be compatible with the masses predicted by the  
469 Standard Model nearly a decade earlier. The final missing piece then was confirming the existence  
470 of the Higgs, which again required the construction of a newer and more powerful collider. CERN

<sup>471</sup> achieved this with the construction of the Large Hadron Collider (LHC), and in 2012 the ATLAS  
<sup>472</sup> and CMS experiments announced the discovery of the Higgs particle [16] [17].

<sup>473</sup> **1.5 Limitations of the Standard Model**

<sup>474</sup> While the Standard Model has enjoyed decades of experimental results which confirm its pre-  
<sup>475</sup> dictions, there are several glaring shortcomings. The observed phenomenon for which the Standard  
<sup>476</sup> Model provides no explanation are summarized below.

- <sup>477</sup> • Gravity - the Standard Model does not account for the fourth fundamental force of gravity.
- <sup>478</sup> • Dark Matter - there is no viable candidate to explain the existence of dark matter, a non-  
<sup>479</sup> interacting form of matter which must exist to account for gravitational observations which  
<sup>480</sup> cannot be explained by general relativity, such as the motion of galaxies, gravitational lens-  
<sup>481</sup> ing, and the structure of the universe [18].
- <sup>482</sup> • Matter-Antimatter asymmetry - the level of CP violation in the Standard Model isn't suf-  
<sup>483</sup> ficient to explain the large discrepancy between the amount of matter and the amount of  
<sup>484</sup> antimatter in the universe today, and the origins of this imbalance are not understood.
- <sup>485</sup> • Neutrino masses - the Standard Model assumes that neutrinos are massless and provides  
<sup>486</sup> no mechanism for them to acquire mass. However, observations of neutrino oscillations  
<sup>487</sup> indicates they posses some small non-zero mass [19].

<sup>488</sup> In addition to these unexplained natural phenomenon, there are several questions about the  
<sup>489</sup> *naturalness* of the Standard Model. The principle of naturalness states that dimensionless ratios  
<sup>490</sup> between physical constants should be of order 1, and that nature should not be arbitrarily fine-  
<sup>491</sup> tuned. While this is largely an aesthetic argument, it points to many aspects of the Standard Model  
<sup>492</sup> for which there exists no natural explanation.

- <sup>493</sup> • Strong CP - while CP symmetry is violated in the weak force, observations indicate that it  
<sup>494</sup> is preserved by the strong force [20]. The Standard Model predicts that CP violation in the

495 strong force is possible. There is no principle which motivates this incongruity between the  
496 weak force and strong force.

- 497 • Hierarchy Problem - The wide range of masses for elementary particles and the wide range of  
498 scales at which the four fundamental forces operate is not motivated by the SM. Specifically,  
499 it is not understood why the Higgs mass is observed to be well below the Plank scale  $\lambda$ ,  
500 which is the energy level at which the effects of quantum gravity become significant. QFT  
501 indicates that the Higgs mass is determined by contributions from all energy scales including  
502  $\lambda$ , meaning that its observed mass is inexplicably small.

503 The limitations of the Standard Model provide a road map for theoretical and experimental  
504 particle physicists, who seek to develop new theories which account for these observations, and  
505 then to find evidence which might support these *Beyond the Standard Model* (BSM) theories. The  
506 next chapter will introduce the BSM theories which motivate the physics search presented in this  
507 thesis.

## Chapter 2: Physics Beyond the Standard Model

510 In light of the various phenomenon unexplained by the Standard Model, physicists have pro-  
 511 posed various extensions to the Standard Model, collectively termed *Beyond the Standard Model*  
 512 (BSM) theories. A particular focus of the physics programs at the Large Hadron Collider (LHC)  
 513 are BSM models which suggest dark matter candidate particles. If these particles couple to Stan-  
 514 dard Model, they could be produced and observed at the LHC. This chapter will explore Hidden  
 515 Valley models, and in particular the potential for Hidden Valley models to produce *semi-visible*  
 516 *jets*. This will set the theoretical foundations for the experimental search presented in the later  
 517 chapters of this thesis. The mechanisms of dark QCD that arise from these models and allow for  
 518 the production of semi-visible jets will also be discussed.

519 **2.1 Hidden Valley Models**

520 Hidden Valley (HV) models are a category of BSM models that allow for dark matter (DM)  
 521 production at the LHC. They extend the Standard Model with an additional non-Abelian gauge  
 522 group [21]. This introduces the possibility of a complex dark sector, which mirrors the complexities  
 523 of Standard Model QCD, and introduces the possibility of dark quarks and gluons. The term  
 524 “hidden valley” refers to the idea that the DM is hidden from the SM by a high-energy barrier, as  
 525 illustrated in Figure 2.1. The dark sector is assumed to communicate with the Standard Model via  
 526 a “portal”, or “messenger particle”, that can interact with both Standard Model and HV forces. For  
 527 the s-channel scenario, the portal is considered to be a new massive mediator particle  $Z'$ .

528 The portal particle allows for the production of dark sector particles at hadron colliders. If  
 529 dark quarks are produced via the decay  $Z' \rightarrow q_D q_D$  they can hadronize and form dark jets. The  
 530 properties of the dark jets are determined by the dynamics of the dark sector, which are explored in

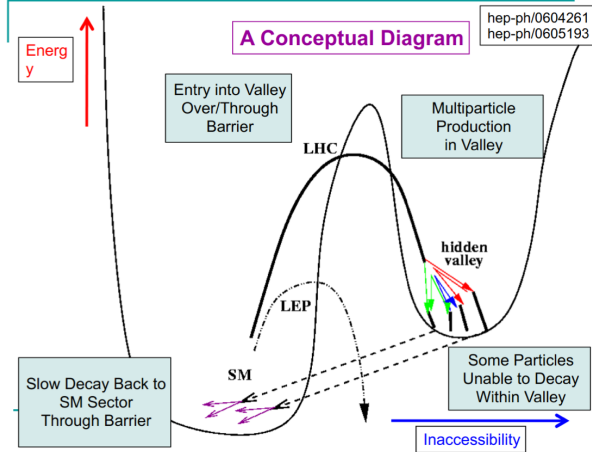


Figure 2.1: Illustration of the hidden valley potential.

531 the subsequent section. Depending on the details of the model, the jets formed by the dark hadrons  
 532 can be categorized as fully dark, semi-visible, leptonic, emerging, or other [21].

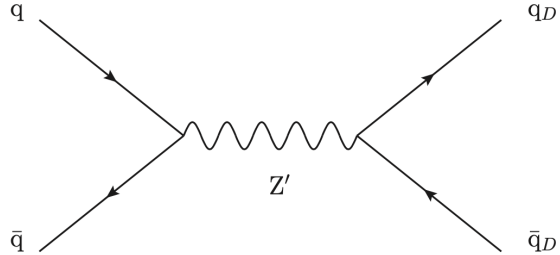


Figure 2.2: The massive mediator particle  $Z'$  of the s-channel realization of a HV model

## 533 2.2 Dark QCD

534 The theoretical underpinning of the semi-visible jet phenomenology is a dark sector with a  
 535 gauge group  $SU(N)_d$  leading to confinement at a scale  $\Lambda_d$ . For illustration, let's consider the  
 536 case of an  $SU(2)_d$  gauge theory, which gives rise to two dark fermionic generations  $\chi_a = \chi_1, \chi_2$ .  
 537 Following the work of Ref [22] we can write the fundamental dark Lagrangian as:

$$\mathcal{L}_{dark} \supset -\frac{1}{2} \text{Tr} G_{\mu\nu}^d G^{d\mu\nu} - \bar{\chi}_a (i\cancel{D} - M_{d,a}) \chi_a \quad (2.1)$$

538        The first term allows for the dark gluons to self-interact, while the second term enables the dark  
539        quarks to hadronize and acquire mass. The dark quarks are assumed to have a common mass  $M_d$ .  
540        The coupling strength of the strongly interacting dark quarks is termed  $\alpha_d$ . At the confinement  
541        scale  $\Lambda_d$ , the dark quarks can form bound states. At the scale  $M_d \approx \Lambda_d$  a QCD-like shower occurs.

542        The properties of the hadrons formed by the dark quarks are of particular importance to the  
543        observed dark QCD dynamics. Dark-isospin number  $U(1)_{1-2}$  and dark-baryon number  $U(1)_{1+2}$   
544        are accidental symmetries of the theory which determine the stability of the hadrons. In the case  
545        of two dark flavors, six dark hadrons can be formed: four mesons ( $\chi_1\bar{\chi}_1$ ,  $\chi_2\bar{\chi}_2$ ,  $\chi_1\bar{\chi}_2$ ,  $\bar{\chi}_1\chi_2$ ) and  
546        two baryons ( $\bar{\chi}_1\bar{\chi}_2$ ,  $\bar{\chi}_1\bar{\chi}_2$ ). The mesons  $\chi_1\bar{\chi}_2$  and  $\bar{\chi}_1\chi_2$  are charged under dark-isospin and will be  
547        stable if this symmetry is unbroken. The baryons would also be stable as they are charged under  
548        the dark-baryon number. These four stable hadrons become dark matter candidates of the theory.  
549        The  $\chi_1\bar{\chi}_1$  and  $\chi_2\bar{\chi}_2$  mesons are not charged under either symmetry and are thus expected to decay.  
550        The unstable mesons can decay into stable dark mesons, or into an off-shell  $Z'$ . The off-shell  $Z'$   
551        will then decay into two DM quarks or two SM quarks, and its products will continue to shower  
552        until the final state particles are stable.

553        The number of stable and unstable dark states varies substantially depending on the details  
554        of the model. The model discussed above can be generalized from  $SU(2)_d$  to  $SU(N)_d$ , with any  
555        number of colors  $N_c$  or flavors  $N_f$ . This affects the ratio of possible stable to unstable mesons,  
556        which can directly impact the amount of missing energy. The fraction of missing energy is a  
557        variable in many dark QCD models, and is especially important in the case of semi-visible jets.

### 558        2.3 Semi-visible Jets

559        A “semi-visible jet” occurs when the heavy  $Z'$  messenger particle decays into dark quarks,  
560        which then hadronize in a QCD-like shower. If some of the dark hadrons are stable while others  
561        decay to SM quarks via the off-shell  $Z'$ , a collimated mixture of visible and dark matter is formed  
562        – this is termed a semi-visible jet. If the  $Z'$  messenger particle is produced at rest, the two jets will  
563        be back-to-back in the transverse plane. If there is an imbalance in the amount of invisible particles

564 between the two jets, one of the jets will be observed to be aligned with missing transverse energy.

565 While there are a myriad of HV and dark QCD models, a handful of model parameters are most  
566 important in determining the observable of these showers within a particle detector. The coupling  
567 strength  $\alpha_d$  is one of the most important, as it controls the fraction of dark hadrons emitted in the  
568 shower and their average  $p_T$ . The mass of the dark quarks directly impacts the jet mass. If the  
569 masses of the dark quark flavors are comparable, the ratio of stable to unstable dark hadrons will  
570 be approximately 1:1. However, if there is a mass splitting, stable or unstable dark hadrons may  
571 be favored, which impacts the amount of missing energy observed.

572 The ratio of stable to unstable dark hadrons in the shower is a critical variable for capturing the  
573 behavior of dark showers. This value is termed  $R_{inv}$ :

$$R_{inv} = \frac{\# \text{ of stable hadrons}}{\# \text{ of hadrons}} \quad (2.2)$$

574 Events containing jets aligned with missing transverse momentum are generally considered to  
575 be misreconstructed by other DM searches, and therefore discarded. This class of final states is  
576 therefore largely uncovered by existing DM searches. The nature of the dark hadron shower is  
577 determined by the following parameters: the  $Z'$  mass  $m_{Z'}$ , the  $Z'$  couplings to visible and dark  
578 quarks  $g_q$  and  $g_{q_D}$ , the number of dark colors and flavors, the characteristic scale of the dark sector  
579 confinement  $\Lambda_D$ , the mass scale of the dark hadrons  $m_D$ , and the average fraction of stable hadrons  
580 in the decay  $R_{inv}$ . The coupling to SM quarks determines the  $Z'$  production cross section.

581

## Part II

582

## Experiment

## Chapter 3: The Large Hadron Collider

585       The Large Hadron Collider (LHC) is a 26.7 km circular high-energy particle accelerator, span-  
 586       ning the Swiss-French border near the city of Geneva, Switzerland [23]. The LHC occupies the  
 587       tunnel constructed in 1989 for the Large Electron-Positron (LEP) Collider, and reaches a maxi-  
 588       mum depth of 170m below the surface. The LHC is operated by the European Organization for  
 589       Nuclear Research (CERN), the largest international scientific collaboration in the world.

590       The LHC accelerates protons and heavy ions, and collides them at four interaction points  
 591       around the ring, with a design center-of-mass energy per collision of  $\sqrt{s} = 14$  TeV. Each interaction  
 592       point is home to one of four detector experiments, which study the products of the collisions. The  
 593       largest of these experiments is the ATLAS detector, a general purpose detector designed to study  
 594       the Standard Model and search for new physics that could be produced in LHC collisions [24].  
 595       The CMS detector is another general purpose detector, designed and operated independently of the  
 596       ATLAS detector, but intended to probe the same range of physics [25]. The ALICE experiment is  
 597       a dedicated heavy ion experiment, and the LHC-b experiment is a dedicated *b*-physics experiment  
 598       [26] [27].

599       This chapter will cover the multi-component accelerator complex powering the LHC, the state-  
 600       of-the-art magnets which steer the particle beams, measurements of the intensity and number of  
 601       collisions produced by the LHC, and finally an overview of LHC activities in the past, present, and  
 602       future.

603 **3.1 Accelerator Physics**

604 **3.1.1 The Journey of a Proton**

605 From 2010 - 2018, the protons which fed the LHC started as hydrogen gas. The electrons were  
606 removed from the hydrogen atoms through the use of strong electric fields. The linear accelerator  
607 LINAC2 then accelerated the protons to an energy of 50 MeV. Between 2018 and 2020, LINAC2  
608 was replaced with LINAC4, which instead accelerates  $H^-$  ions, hydrogen atoms with two electrons.  
609 LINAC4 is capable of accelerating the  $H^-$  ions to 160 MeV. Before injection to the next part of  
610 the acceleration chain, both electrons are stripped from the  $H^-$  ions, leaving just protons. From  
611 here the protons enter the Proton Synchrotron booster, where they are accelerated up to 1.4 GeV of  
612 energy. Subsequently they are sorted into bunches separated in time by 25 ns, where each bunch  
613 contains approximately  $10^{11}$  protons. Next the bunches pass through the Proton Synchrotron (PS)  
614 and the Super Proton Synchrotron (SPS), where they reach energies of 25 GeV and 450 GeV  
615 respectively. Finally they are injected into the LHC as two beams traveling in opposite direction.  
616 The original design allowed each beam to be accelerated up to 7 TeV of energy. Due to limitations  
617 in the performance of the superconducting LHC magnets, the highest energy actually achieved by  
618 the LHC beams during Run 2 was 6.5 TeV, giving a collision center-of-mass energy of  $\sqrt{s} = 13$   
619 TeV [28]. Figure 3.1 shows the full LHC accelerator complex.

620 Acceleration in the LHC is performed by eight radio frequency (RF) cavities located around the  
621 ring. Each RF cavity produces a 2 MV electric field oscillating at 40 MHz. The 40MHz oscillation  
622 produces a point of stable equilibrium every 2.5 ns. These points of equilibrium are synchronized  
623 with the occurrence of the proton bunches produced in the PS – a proton bunch occupies one out  
624 of every ten points of stable equilibrium, such that the bunches maintain a 25 ns spacing [28].

625

## The CERN accelerator complex Complexe des accélérateurs du CERN

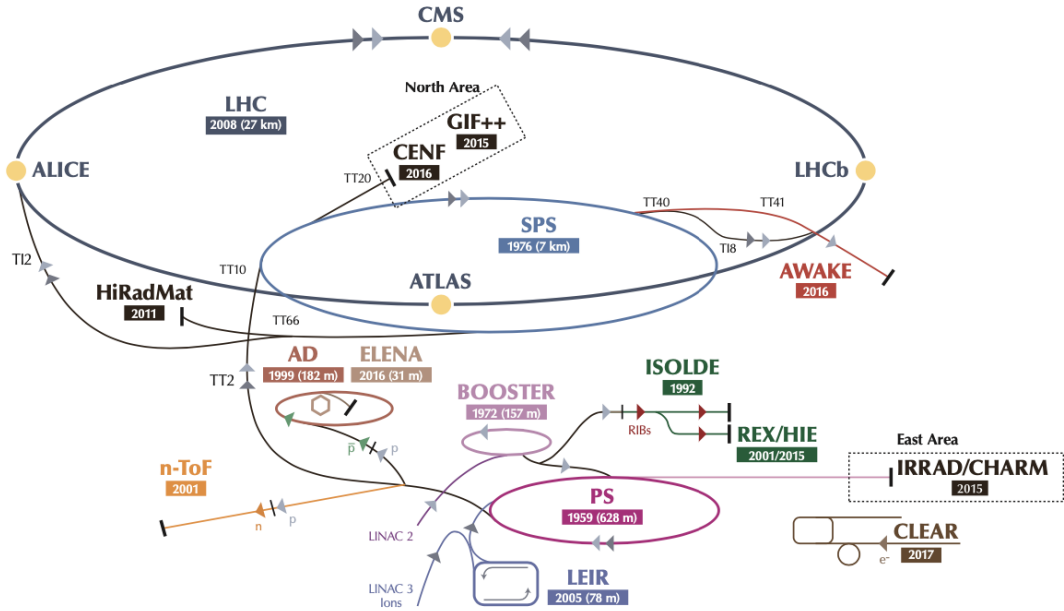


Figure 3.1: The LHC accelerator complex at CERN [29]

### 626 3.1.2 Magnets

627 In addition to the acceleration cavities, the LHC houses 9593 superconducting magnets which  
 628 direct and focus the proton beam on its 27 kilometer journey. The magnets are comprised of super-  
 629 conducting Niobium-Titanium coils cooled to 1.9K by superfluid helium. As the beams approach  
 630 one of the four collision points around the ring, multipole magnets focus and squeeze the beam for  
 631 optimal collisions [28].

632 The LHC is divided into sections, where each section contains an arc and a straight insertion. The arcs are composed of 1232 large dipole magnets which bend the beam  
 633 to follow the roughly circular 27 km path. The main dipoles generate powerful 8.3 tesla magnetic  
 634 fields to achieve this bend. Each dipole magnet is 15 meters long and weighs 35 tonnes. The  
 635 dipoles work in conjunction with quadrupole magnets, which keep the particles in a focused beam,  
 636 and smaller sextupole, octupole and decapole magnets which tune the magnetic field at the ends of  
 637 the dipole magnets [30].

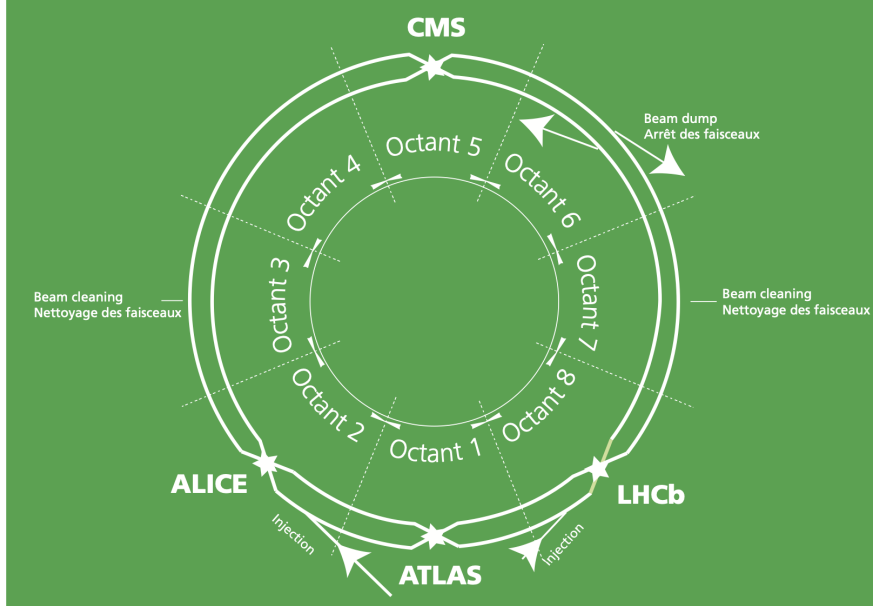


Figure 3.2: The octants of the LHC and location of various beam activities [28]. Stars indicate the locations of beam collisions, and the associated detectors recording the outcome of those collisions.

639        The straight insertion sections have different purposes depending on their location around the  
 640        ring: beam collisions, beam injection, beam dumping, or beam cleaning. At the four collision  
 641        points, insertion magnets squeeze the beam to ensure a highly focused collision. This is accom-  
 642        plished with a triplet of quadrupole magnets, which tighten the beam from 0.2 millimeters to just  
 643        16 micrometers in diameter. Insertion magnets also clean the beam, which prevents stray particles  
 644        from hitting sensitive components throughout the LHC. When the LHC is ready to dispose of a  
 645        beam of particles, beam dump magnets deflect the path of the beam into a straight line towards  
 646        a block of concrete and graphite that stops the beam. A dilution magnet then reduces the beam  
 647        intensity by a factor of 100,000 before the final stop [30]. Figure 3.2 shows the locations various  
 648        beam activities.

### 649        3.2 Luminosity

650        Collisions at the LHC occur when the two beams of proton bunches cross at one of the four  
 651        interaction points. The intensity of collisions is described by the instantaneous luminosity, the

652 formula for which is given in equation 3.1.

$$L = \frac{fN_1N_2}{4\pi\sigma_x\sigma_y} \quad (3.1)$$

653 Here  $f$  is the revolution frequency,  $N_1$  and  $N_2$  are the number of particle per bunch for each  
654 beam, and  $\sigma_x$ ,  $\sigma_y$  are the horizontal and vertical beam widths.

655 The instantaneous luminosity gives the number of the collisions that could be produced at the  
656 interaction point per unit of cross-sectional area per unit of time, generally expressed in  $\text{cm}^{-2}\text{s}^{-1}$ .  
657 The integrated luminosity is obtained by integrating the instantaneous luminosity over a given  
658 block of time, and measures the total number of collisions which have occurred during that op-  
659 eration period. The total integrated luminosity is directly correlated with the size of the datasets  
660 collected by the LHC experiments. Total integrated luminosity for Run 2 is illustrated in Figure  
661 3.3.

662 High levels of instantaneous luminosity result in multiple  $pp$  collisions per bunch crossing,  
663 which leads to an effect known as *pileup*. Pileup poses a challenge for detector physics, as recon-  
664 structing the products of multiple simultaneous events is far more challenging than reconstructing  
665 a single event with no pileup. Pileup conditions vary from year-to-year and run-to-run of LHC op-  
666 eration, and the impact of these conditions are taken into account when analyzing the data, as will  
667 be discussed further in Chapter 5. Measurement of pileup conditions during Run 2 are illustrated  
668 in Figure 3.3.

669 The design peak luminosity of the LHC is  $1.0 \times 10^{34} \text{ cm}^{-2}\text{s}^{-1}$ . During Run 1 of the LHC the  
670 peak instantaneous luminosity was  $0.8 \times 10^{34} \text{ cm}^{-2}\text{s}^{-1}$ . Over the course of Run 1 the LHC collected  
671 a total integrated luminosity of  $5.46 \text{ fb}^{-1}$  at  $\sqrt{s} = 7 \text{ TeV}$ , and  $22.8 \text{ fb}^{-1}$  at  $\sqrt{s} = 8 \text{ TeV}$ . Following the  
672 first long shutdown and upgrade phase of operations, the LHC achieved a center of mass energy  
673  $\sqrt{s} = 13 \text{ TeV}$  at the beginning of Run 2 in 2015. The LHC was also able to deliver  $2.0 \times 10^{34}$   
674  $\text{cm}^{-2}\text{s}^{-1}$  peak instantaneous luminosity, double the design value. During LHC Run 2, from 2015-  
675 2018, the LHC delivered  $156 \text{ fb}^{-1}$  of integrated luminosity for proton-proton collisions. Run 3 of

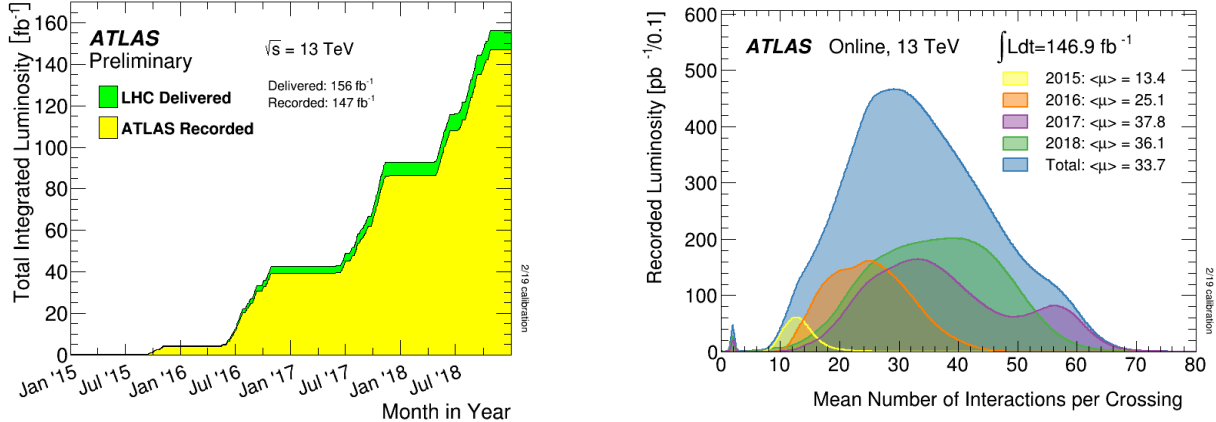


Figure 3.3: (Left) Total integrated luminosity over the course of Run 2. (Right) Average number of  $pp$  interactions per bunch crossing in Run 2. Each curve is weighted by the integrated luminosity for the year.

676 the LHC began in 2022, and is expected to deliver  $250 \text{ fb}^{-1}$  of integrated luminosity to the ATLAS  
 677 and CMS experiments by 2026 [31].

678 The goal of LHC physic analyses is to find and study rare events produced by interesting  
 679 physics processes. The cross section  $\sigma$  of a given process indicates the probability of that process  
 680 occurring given the beam conditions of the LHC. Multiplying the cross section by the integrated  
 681 luminosity of a dataset gives the expected number of events for that process within the dataset.

$$N_{\text{events}} = \int \sigma L(t) dt = \mathcal{L} \times \sigma \quad (3.2)$$

682 The cross section for most processes of interest, especially BSM processes, is several orders of  
 683 magnitude below the total cross section for the LHC. Therefore maximizing the number of events  
 684 produced in collisions is crucial to increase the likelihood of producing events from processes of  
 685 interest. For this reason, maximizing instantaneous luminosity is a key factor in accelerator design  
 686 and operation, while mitigating the resulting pileup effects is a key component in detector design  
 687 and operation.

688    **3.3 LHC Timeline**

689    The first proton-proton collisions at the LHC were achieved in 2010 with a center-of-mass  
690    energy of  $\sqrt{s} = 7$  TeV. Run 1 of the LHC took place between 2010 and early 2013, during which  
691    time the center-of-mass collision energy increased from 7 TeV to 8 TeV. Figure 3.4 shows an  
692    overview of LHC activities beginning in 2011, in the midst of Run 1. The data collected during  
693    Run 1 led to the discovery of the Higgs Boston in 2012 [32].

694    Between 2013 and 2015 the LHC underwent the first Long Shutdown (LS1) during which  
695    time maintenance and renovation was performed on the accelerator chain, including the repair and  
696    consolidation of the high-current splices which connect the super-conducting LHC magnets. Run  
697    2 of the LHC took place from 2015 to 2018 and achieved a center-of-mass energy of  $\sqrt{s} = 13$  TeV.  
698    Analysis of data collected in Run 2 is still on going, and is the subject of study in this thesis.

699    Between 2018 and 2022 the LHC underwent the second Long Shutdown (LS2), allowing for  
700    further detector and accelerator maintenance and upgrades. Key improvements to the LHC in-  
701    cluded the improvement of the insulation for over 1200 diode magnets, and the upgrade from  
702    LINAC2 to LINAC4 mentioned in Section 3.1.1. Run 3 of the LHC began in 2022 and achieved a  
703    center-of-mass energy of  $\sqrt{s} = 13.6$  TeV.

704    Run 3 is scheduled to continue through 2026, at which point the LHC machine and detectors  
705    will undergo upgrades for the *high luminosity* LHC (HL-LHC). The HL-LHC will increase the  
706    instantaneous machine luminosity by a factor of 5 - 7.5 with respect to the nominal LHC design.  
707    The bottom panel of Figure 3.4 shows an overview of the preparation work for the HL-LHC that  
708    has been going on concurrently with Run 1, 2, and 3 of the LHC [33].



Figure 3.4: Timeline of LHC and HL-LHC activities [31]. Integrated luminosity estimates are approximate, and not reflective of the exact amount delivered to each experiment.

## Chapter 4: The ATLAS Detector

711     The ATLAS detector (**A** Toroidal **L**H**C** Apparatu**S**) is one of two general purpose physics  
 712   detectors designed to study the products of proton-proton collisions at the LHC. The detector is  
 713   composed of a variety of specialized subsystems, designed to fully capture a wide array of physics  
 714   processes. The apparatus is 25m high, 44m in length, and weighs over 7000 tons [34]. The LHC  
 715   beam pipes direct proton beams to an interaction point at the center of ATLAS, and the cylindrical  
 716   detector design captures a complete 360° view of the *event*, tracking all particles that result from  
 717   the collision.

718     The main components of the ATLAS detector are the Inner Detector (ID) which provides high  
 719   precision tracking of charged particles leaving the collision vertex, the calorimeter system which  
 720   measures the energy of electromagnetic and hadronic objects, and the Muon Spectrometer (MS)  
 721   which gives detailed information about muons that reach the outer radii of the detector. Two  
 722   magnet systems, a 2 T solenoid magnet surrounding the ID, and a 0.5-1.0 T toroid magnet system  
 723   situated throughout the MS, produce magnetic fields which bend the trajectory of charged particles  
 724   traversing the detector. In addition to the main detector components, dedicated forward detectors  
 725   monitor beam conditions and instantaneous luminosity, and an online trigger system reduces the  
 726   data rate to a manageable level for storage. Each of these components will be discussed in further  
 727   detail in this chapter.

### 728   4.1 Coordinate System and Geometry

729     The ATLAS detector employs a right hand cylindrical coordinate system. The  $z$  axis is aligned  
 730   with the beam line, and the x-y plane sits perpendicular to the beam line. The coordinate system  
 731   origin is centered on the detector, such that the origin corresponds with the interaction point of the

732 two colliding beams. The detector geometry is usually characterized by polar coordinates, where  
733 the azimuthal angle  $\phi$  spans the x-y plane. The polar angle  $\theta$  represents the angle away from the  
734 beam line, or  $z$  axis.  $\theta = 0$  aligns with the positive  $z$ -axis, and  $\phi = 0$  aligns with the positive x-axis.

735 The polar coordinate  $\theta$  is generally replaced by the Lorentz invariant quantity *rapidity* or  $y$ :

$$y = \frac{1}{2} \ln\left(\frac{E + p_z}{E - p_z}\right). \quad (4.1)$$

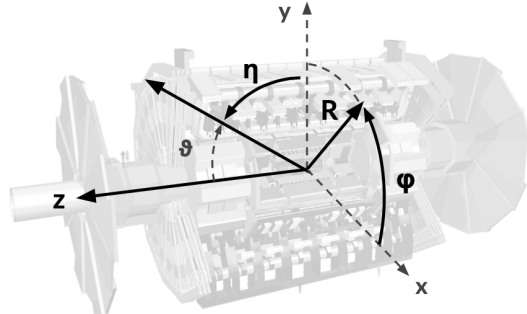
736 This substitution is advantageous because objects in the detector are traveling at highly rela-  
737 tivistic speeds. The relativistic speed also means that the masses of the particles are generally small  
738 compared to their total energy. In the limit of zero mass, the rapidity  $y$  reduces to the pseudorapid-  
739 ity  $\eta$ , which can be calculated directly from the polar angle  $\theta$ :

$$\eta = -\ln\left(\frac{\theta}{2}\right). \quad (4.2)$$

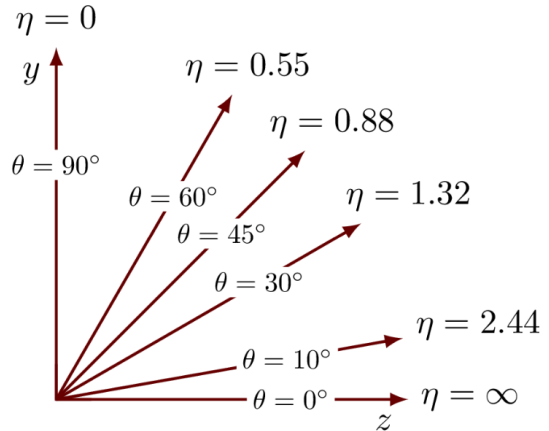
740 The distance between physics objects in the detector is generally expressed in terms of the solid  
741 angle between them  $\Delta R$ :

$$\Delta R = \sqrt{\Delta\phi^2 + \Delta\eta^2} \quad (4.3)$$

742 Figure 4.1a depicts the orientation of the coordinate system with respect to the ATLAS detector,  
743 while Figure 4.1b illustrates the relationship between  $\theta$ ,  $\eta$ , and the beamline axis  $z$ . Direct or “head  
744 on” proton-proton collisions are more likely to result in objects whose momentum is directed  
745 along transverse plane (low  $|\eta|$ ); glancing proton-proton collisions are more likely to result in  
746 objects whose momentum is directed along the  $z$ -axis (high  $|\eta|$ ). Due to the difference in the  
747 nature of these collisions, as well as the cylindrical design of the ATLAS detector, the detector  
748 is divided into regions of low and high  $\eta$ . Each subsystem has a “central” or “barrel” region  
749 covering low  $|\eta|$ , while the “forward” or “end-cap” regions cover the area up to  $|\eta| = 4.9$ . Each of  
750 the three main ATLAS subsystems will be discussed in the following sections.



(a) The ATLAS geometry



(b) Relationship between  $\eta$  and  $\theta$

Figure 4.1: ATLAS coordinate system and geometry

## 751 4.2 Inner Detector

752 The Inner Detector (ID) is the ATLAS subsystem closest to the interaction point. The primary  
 753 purpose of the ID is to determine the charge, momentum, and trajectory of charged particles pass-  
 754 ing through the detector. With this information the ID is also able to precisely determine interaction  
 755 vertices.

756 The ID is composed of three sub-detectors; the Pixel Detector, the Semiconductor Tracker  
 757 (SCT) and the Transition Radiation Tracker (TRT). Figure 4.2 shows the location of these three  
 758 subsystems with respect to each other and the interaction point.

### 759 4.2.1 Pixel Detector

760 The pixel detector is the first detector encountered by particles produced in LHC collisions.  
 761 The original pixel detector consists of 3 barrel layers of silicon pixels, positioned at 5 cm, 9 cm  
 762 and 12 cm from the beamline. There are also 3 disks on each end-cap positioned 50 - 65 cm from  
 763 the interaction point, providing full coverage for  $|\eta| < 2.2$ . The layers are comprised of silicon  
 764 pixels each measuring  $50 \times 400 \mu\text{m}^2$ , with 140 million pixels in total. The pixels are organized  
 765 into modules, which each contain a set of radiation hard readout electronics chips. In 2014, the  
 766 Insertable B-layer (IBL) was installed, creating a new innermost layer of the pixel detector sitting

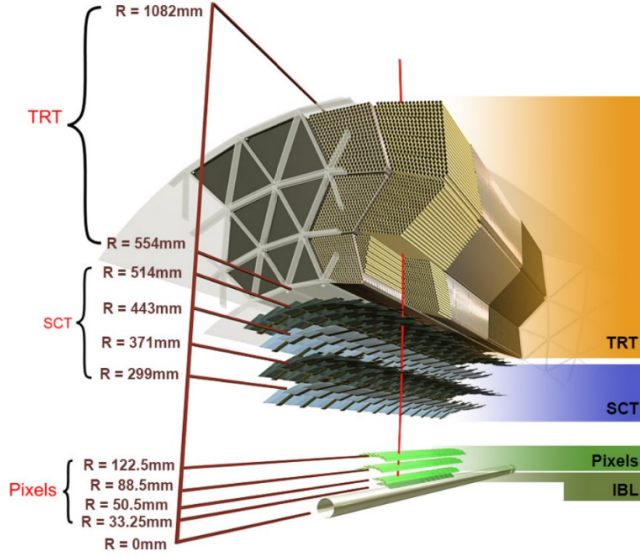


Figure 4.2: A 3D visualization of the structure of the ID in the barrel region [35]

just 3.3 cm from the beamline. The pixels of the IBL measure  $50 \mu\text{m}$  by  $250 \mu\text{m}$ , and cover a pseudo-rapidity range up to  $|\eta| < 3$ . The IBL upgrade enhances the pixel detector's ability to reconstruct secondary vertices associated with short-lived particles such as the b-quark. The improved vertex identification also helped compensate for increasing pile-up in Run 2 [34].

#### 4.2.2 Semiconductor Tracker

The SCT provides at least 4 additional measurements of each charged particle. It employs the same silicon technology as the Pixel Detector, but utilizes larger silicon strips which measure  $80 \mu\text{m}$  by  $12.4 \text{ cm}$ . The SCT is composed of 4 barrel layers, located between 30 cm and 52 cm from the beamline, and 9 end-cap layers on each side. The SCT can distinguish tracks that are separated by at least  $200 \mu\text{m}$ .

#### 4.2.3 Transition Radiation Tracker

The TRT provides an additional 36 hits per particle track. The detector relies on gas filled straw tubes, a technology which is intrinsically radiation hard. The straws which are each 4 mm in diameter and up to 150 cm in length and filled with xenon gas. The detector is composed of about

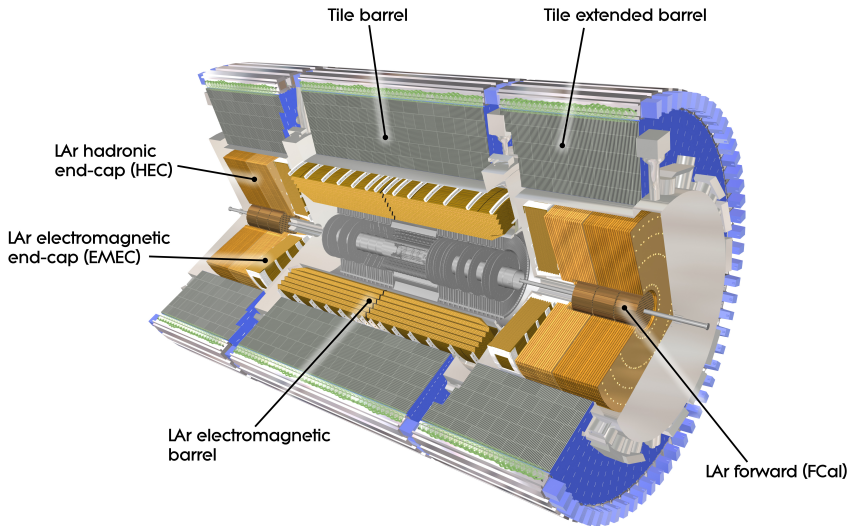


Figure 4.3: ATLAS calorimetry system [36]

781 50000 barrel region straws and 640000 end-cap straws, comprising 420000 electronic readout  
 782 channels. Each channel provides a drift time measurement with a spatial resolution of  $170\text{ }\mu\text{m}$  per  
 783 straw. As charged particles pass through the many layers of the detector, transition radiation is  
 784 emitted. The use of two different drift time thresholds allows the detector to distinguish between  
 785 tracking hits and transition radiation hits.

### 786 4.3 Calorimeters

787 The ATLAS calorimeter system is responsible for measuring the energy of electromagnetically  
 788 interacting and hadronically interacting particles passing through the detector. The calorimeters are  
 789 located just outside the central solenoid magnet, which encloses the inner detectors. The calorime-  
 790 ters also stop most known particles, which the exception of muons and neutrinos, preventing them  
 791 from traveling to the outermost layers of the detector. The ATLAS calorimetry system is composed  
 792 of two subsystems - the Liquid Argon (LAr) calorimeter for electromagnetic calorimetry and the  
 793 Tile calorimeter for hadronic calorimetry. The full calorimetry system is shown in Figure 4.3.

794 4.3.1 Liquid Argon Calorimeter

795 The LAr calorimeter is a sampling calorimeter designed to trigger on and measure the ener-  
796 gies of electromagnetic (EM) particles, as well as hadronic particles in the high  $\eta$  regions. It is  
797 divided in several regions, as shown in Figure 4.3. For the region  $|\eta| < 1.4$ , the electromagnetic  
798 barrel (EMB) is responsible for EM calorimetry, and provides high resolution energy, timing,  
799 and position measurements for electrons and photons passing through the detector. The elec-  
800 tromagnetic endcap (EMEC) provides additional EM calorimetry up to  $|\eta| < 3.2$ . In the re-  
801 gion  $1.4 < |\eta| < 3.2$ , the hadronic endcap (HEC) provides hadronic calorimetry. For hadronic  
802 calorimetry in the region  $|\eta| < 1.4$ , corresponding to a detector radii  $> 2.2$  m, the less expensive  
803 tile calorimeter (discussed in the next section) is used instead. A forward calorimeter (FCAL)  
804 extends the hadronic calorimetry coverage up to  $3.1 < |\eta| < 4.8$  [37].

805 The LAr calorimeter is composed of liquid argon sandwiched between layers of absorber mate-  
806 rial and electrodes. Liquid argon is advantageous as a calorimeter active medium due to its natural  
807 abundance and low cost, chemical stability, radiation tolerance, and linear response over a large  
808 energy range [38]. The calorimeter is cooled to 87k by three cryostats: one barrel cryostat encom-  
809 passing the EMB, and two endcap cryostats. The barrel cryostat also encloses the solenoid which  
810 produces the 2T magnetic field for the inner detector. Front-end electronics are housed outside the  
811 cryostats and are used to process, temporarily store, and transfer the calorimeter signals.

812 **Electromagnetic Calorimeter**

813 For the electromagnetic calorimeters, the layers of electrodes and absorber materials are ar-  
814 ranged in an an accordion shape, as illustrated in Figure 4.4. The accordion shape ensures that  
815 each half barrel is continuous in the azimuthal angle, which is a key feature for ensuring consistent  
816 high resolution measurements. Liquid argon permeates the space between the lead absorber plates,  
817 and a multilayer copper-polymide readout board runs through the center of the liquid argon filled  
818 gap.

819 The detection principle for the LAr calorimeter is the current created by electrons which are

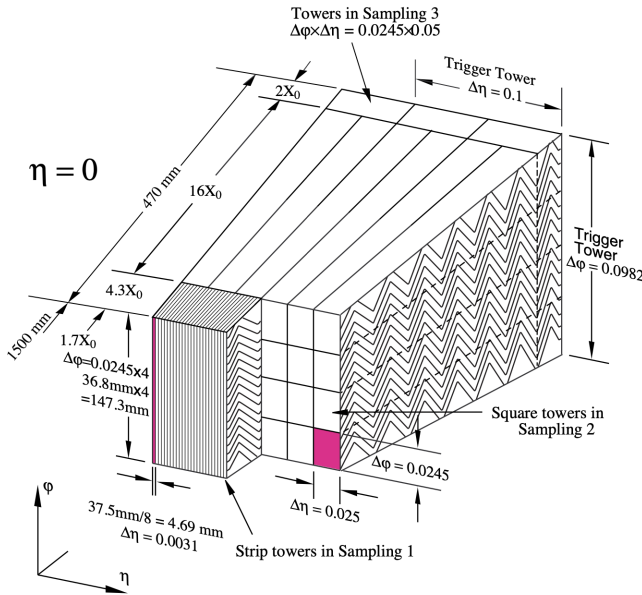


Figure 4.4: Diagram of a segment of the EMB, demonstrating the accordion plate arrangement [37]

820 released when a charged particle ionizes the liquid argon. In the barrel region, the electrons are  
 821 driven towards the center electrodes by a 2000 V potential with a drift time of less than 450 ns [39].  
 822 In the end-caps the voltage varies as a function of the radius in order to maintain a flat response  
 823 [37]. The amount of current produced by the ionized electrons is proportional to the energy of  
 824 the particle creating the signal. Figure 4.5 shows the shape of the signal produced in the LAr  
 825 calorimeter, before and after it undergoes shaping during the readout process. The shaping of the  
 826 pulse enforces a positive peak and a negative tail, which ensures that subsequence pulses can be  
 827 separated with the precision required for the 25 ns LHC bunch spacing [37].

## 828 Hadronic End-cap Calorimeter

829 The HEC sits radially beyond the EMEC. The copper absorber plates in the HEC are oriented  
 830 perpendicular to the beamline, with LAr as the active medium. Each end-cap is divided into two  
 831 independent wheels; the inner wheel uses 25 mm copper plates, while the outer wheel uses 50 mm  
 832 plates as a cost saving measure. In each wheel, the 8.5 mm plate gap is crossed by three parallel

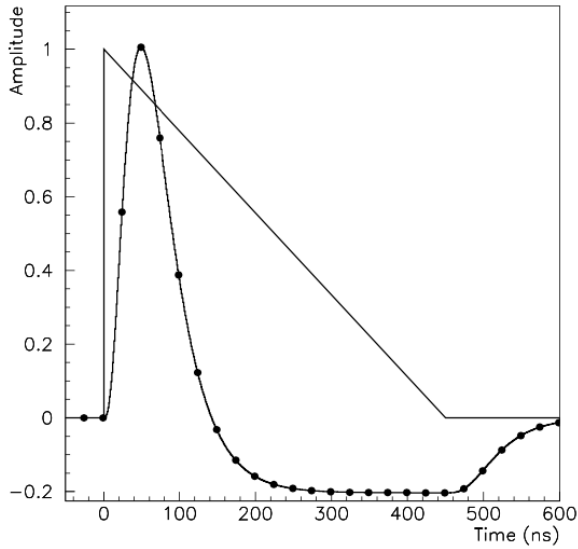


Figure 4.5: A LAr pulse as produced in the detector (triangle) and after shaping (curve) [37]

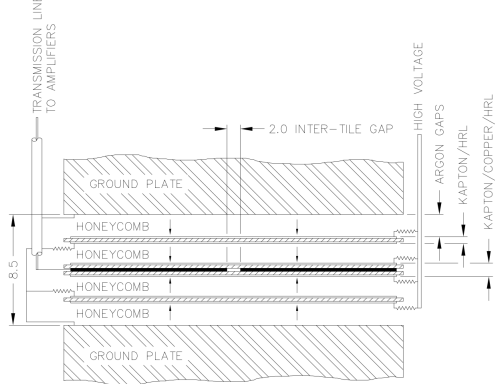


Figure 4.6: Readout gap structure in HEC [37]

833 electrodes, creating an effective drift distance of 1.8 mm. This gap is illustrated in Figure 4.6.  
 834 Each wheel is divided into 32 wedge-shaped modules, each containing their own set of readout  
 835 electronics.

### 836 **Forward Calorimeter**

837 The forward range is covered by the FCal, which provides both EM and hadronic calorimetry.  
 838 It is composed of three active cylindrical modules; one EM module with copper absorber plates,  
 839 and two hadronic modules with tungsten absorber plates. The plates are oriented perpendicular to

840 the beamline, and LAr is used as the active material throughout. The electrodes of the FCal consist  
841 of tubes that run parallel to the beam line, arranged in a honeycomb pattern. The resulting LAr  
842 gaps are as small as  $250 \mu\text{m}$ , which enables the FCal to handle the large influx of particles in the  
843 forward region [37].

844 4.3.2 Tile Calorimeter

845 The Tile Calorimeter (TileCal) provides hadronic calorimetry in the region  $\eta < 1.7$ , and sur-  
846 rounds the LAr calorimeter. It is responsible for measurements of jet energy and jet substructure,  
847 and also plays an important role in electron isolation and triggering (including muons) [40]. Tile-  
848 Cal is composed of 3 sections, as shown in Figure 4.3; a barrel calorimeter sits directly outside the  
849 LAr EMB and provides coverage up to  $\eta < 1.0$ . Two extended barrel sections sit outside the LAr  
850 endcaps and cover the region  $0.8 < \eta < 1.7$ .

851 TileCal is a sampling calorimeter composed of steel and plastic scintillator plates as illustrated  
852 in Figure 4.7. A total of 460,000 scintillators are read out by wavelength-shifting fibers. The  
853 fibers are gathered to define cells and in turn read out by photomultiplier tubes, which amplify  
854 the signal and convert it to an electrical signature. Each cell has an approximate granularity of  
855  $\Delta\eta \times \Delta\phi = 0.1 \times 0.1$ . Each barrel is divided azimuthally into 64 independent modules, an example  
856 of which is show in Figure 4.7. The modules are each serviced by front-end electronic housed in a  
857 water-cooled drawer on the exterior of the module.

858 The detection principle of the TileCal is the production of light from hadronic particles inter-  
859 acting with the scintillating tiles. When a hadronic particle hits the steel plate, a shower of particles  
860 are produced. The interaction of the shower with the plastic scintillator produces photons, the num-  
861 ber and intensity of which are proportional to the original particle's energy.

862

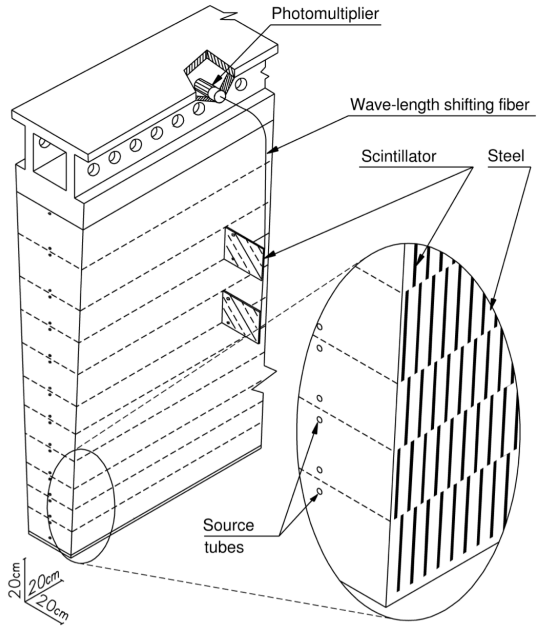


Figure 4.7: TileCal wedge module [40]

#### 863 4.4 Muon Spectrometer

864 Unlike electrons, photons, and hadrons, muons interact minimally with the ATLAS calorimeters, and can pass through large amounts of detector material without stopping. The ATLAS Muon  
 865 Spectrometer (MS) provides additional tracking information to improve the identification and measurement of muons. The MS comprises the outermost layers of the detector, and is interspersed  
 866 with toroid magnets (discussed in Section 4.5), which provide a magnetic field of approximately  
 867 0.5 T. The magnetic field bends the trajectory of the muons as they pass through the detector, and  
 868 the degree of the bend is directly correlated with the muon momentum. The path of the muon is  
 869 primarily measured by hits in three layers of Monitored Drift Tube (MDT) precision chambers,  
 870 which cover the range  $|\eta| < 2.7$ . The barrel layout of the MS is show in Figure 4.8.

873 Muon triggering is provided by three layers of Resistive Plate Chambers (RPC) in the barrel  
 874 ( $|\eta| < 1.05$ ), and 3 - 4 layers of Thin Gap Chambers (TGC) in the end-caps ( $1.05 < |\eta| < 2.4$ ).  
 875 RPCs and TGCs also provide muon track measurements in the non-bending coordinate ( $\phi$ ). RPCs  
 876 are constructed from two parallel resistive plates separated by a 2mm gap filled with a sensitive

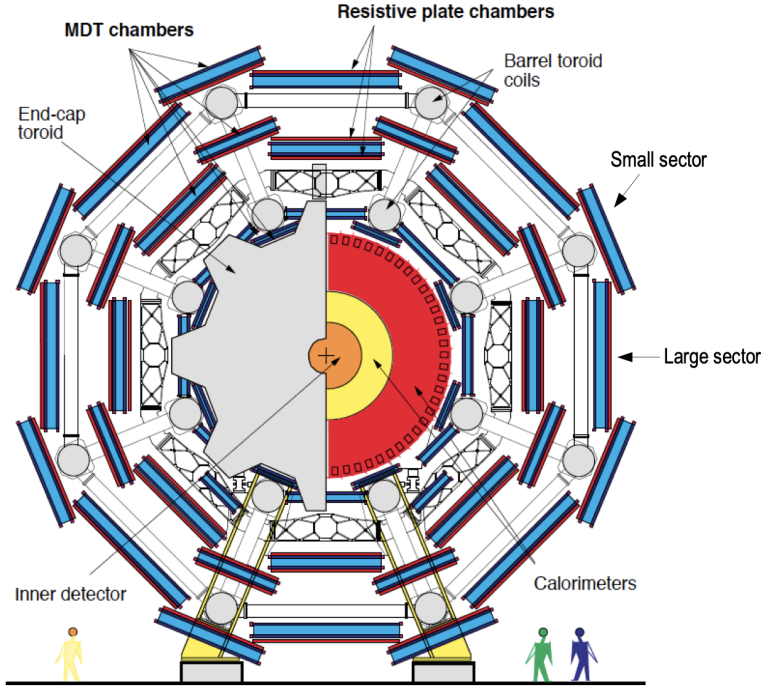


Figure 4.8: Cross section view of the muon spectrometer system [41]

gas mixture. This provides a total of six independent measurements for each muon track, with a spatial resolution of  $\sim 1$  cm and a time resolution of  $\sim 1$  ns. Time measurements from the RPCs are primarily associated to hits in the MDT precision chambers to determine the bunch crossing. The time measurement is also used to reject cosmic muons, and to search for delayed signals. TCGs provide triggering in the end-cap regions, and consist of parallel  $30\ \mu\text{m}$  wires suspended in a sensitive gas mixture. TCGs provide high radiation tolerance and a fast response time, both features that are necessary for handling the high flux of muons in the forward region [41].

Precision measurements of muon momentum and position are primarily achieved by MDTs. The MDTs are constructed from 30 mm diameter tubes, permeated by a gas mixture of 93% Ar and 7% CO<sub>2</sub>. The average single-tube spatial resolution is  $80\ \mu\text{m}$ . Each chamber consists of six drift tube layers, which together provide a muon track segment resolution of  $35\ \mu\text{m}$ . The momentum of the muons can be calculated from the bend in the muon trajectory as they pass through the 0.5T magnetic field provided by the toroids. For a  $p_T = 1$  TeV track, the average  $p_T$  resolution is 11%. In the inner most end-cap wheels, Cathode Strip Chambers (CSC) are used instead of MDTs,

891 covering the region  $2.0 < |\eta| < 2.7$ . CSCs are multi-wire proportional chambers, with a cathode  
892 strip readout. The CSCs have a spatial resolution in the range of  $50 \mu\text{m}$ , and a maximum drift time  
893 of about 30 ns, which makes them superior for handling the high flux of particles in the forward  
894 region [42].

895 **4.5 Magnet System**

896 The ATLAS magnet system consists of four sets of superconducting magnets: a barrel solenoid,  
897 a barrel toroid, and two end-cap toroids. The solenoid magnet produces a 2T magnetic field re-  
898 sponsible for bending the trajectories of charged particles as they pass through the inner detector.  
899 The three toroid magnets provide a field of 0.5 - 1 T and curve the path of muons passing through  
900 the muon spectrometer.

901 The inner solenoid magnet is composed of over 9 km of niobium-titanium superconductor  
902 wires, which are imbedded into strengthen pure aluminum strips. The solenoid is just 4.5 cm  
903 thick, which minimizes interactions between the magnet material and particles passing through the  
904 detector. It is housed in the LAr cryostat, as described in section 4.3.1, which further reduces the  
905 amount of non-detector material required to support the solenoid. The return yoke of the magnet  
906 is provided by the iron absorber of the TileCal [43].

907 The central ATLAS toroid magnet, providing the magnetic field for the barrel region of the MS,  
908 is the largest toroidal magnet ever constructed at 25 m in length. The toroid is composed of eight  
909 individual coils, each housed in their own cryostat. The toroidal magnetic field is advantageous  
910 as the direction of the field is almost perpendicular to the path of the charged particles. 56 km of  
911 aluminum stabilized niobium-titanium-copper superconductor wire compose the magnet. In each  
912 end-cap, eight smaller superconducting coils extend the toroidal magnetic field to particles leaving  
913 the detector in the forward direction [43]. Figure 4.9 shows the layout of the toroid magnets.

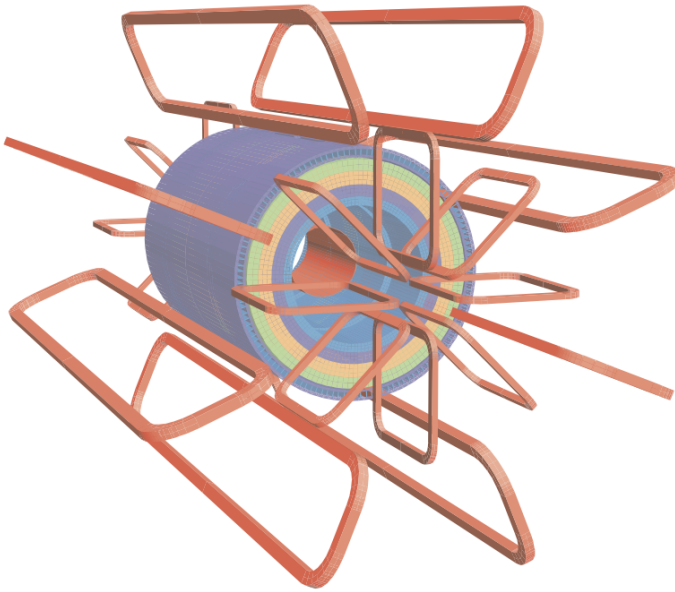


Figure 4.9: Layout of the barrel and endcap toroid magnets [34]

## 914 4.6 Forward Detectors

915 In addition to the inner detector, calorimeters, and muon spectrometer, three smaller detectors  
 916 provide coverage in the very forward region. The innermost forward detector, at 17 m from the  
 917 interaction point, is the **L**Uminosity measurement using **C**erenkov **I**ntegrating **D**etector (LUCID).  
 918 LUCID's primary purpose is to measure the relative online-luminosity for the ATLAS detector,  
 919 from inelastic  $p - p$  scattering. The detector is composed of 20 aluminum Cerenkov tubes which  
 920 surround the beam pipe and face towards the interaction point.

921 The second forward detector is the Zero-Degree Calorimeter (ZDC), located 140 m from the  
 922 interaction point in both directions, at the point where the LHC beam-pipe divides into two separate  
 923 pipes. The ZDC's primary purpose is to detect forward neutrons from heavy ion collisions.

924 The third forward detector is the Absolute Luminosity For ATLAS (ALFA) system, located 240  
 925 m from the interaction point in both directions. ALFA determines luminosity by measuring elastic  
 926 scattering at small angles, from which luminosity can be calculated via the optical theorem. The  
 927 detector is built from scintillating fiber trackers. These are connected to the accelerator vacuum

via Roman pots, which allow the detector to come as close as 1mm to the beam without disrupting the machine vacuum. The LUCID and ALFA detectors are crucial to determining the real-time conditions of the beams and the total luminosity delivered to the ATLAS detector [34].

## 4.7 Trigger and Data Acquisition

The trigger and Data Acquisition systems (TDAQ) are responsible for selecting the most viable events to save for further downstream processing. Because of the high luminosities delivered to the ATLAS detector, not all events recorded can be saved; the 40 MHz bunch crossing rate must be reduced by 5 orders of magnitude to an event storage rate of  $\sim 1$  kHz. The trigger system is composed of three distinct levels: Level 1 (L1), Level 2 (L2) and the event filter. Collectively the L2 trigger and the event filter form the High Level Trigger (HLT).

The L1 trigger is implemented in the hardware of the ATLAS calorimeter and muon systems. The primary modality of the L1 trigger is to identify muons, electrons, photons, jets, and  $\tau$ -leptons with high transverse momentum. Particles with high transverse momentum are more likely to originate from direct, high energy collisions, which are most likely to produce interesting physics processes. The L1 trigger also identifies events with large missing transverse energy, which could be indicative of new physics. The L1 muon trigger (L1Muon) relies on RPC and TGC trigger chambers in the barrel and end-cap regions of the muon spectrometer. The L1 Calorimeter Trigger (L1Calo) uses reduced granularity information collected by all the calorimeter subsystems. Results from the L1Muon and L1Calo triggers are combined by the Central Trigger Processor (CTP), which implements a trigger ‘menu’, listing various combinations of trigger requirements. The maximum L1 acceptance rate is 75 kHz, and the L1 trigger decision must reach the front-end electronics within  $2.5 \mu\text{s}$  of its associated bunch-crossing [34].

The L1 trigger defines a Region-of-Interest (RoI) for each passing event. The ROI is represented by the  $\eta$ - $\phi$  detector region where interesting features were identified by the L1 selection process. Information about the type of feature identified and the threshold which was exceeded to trigger the L1 response is also recorded. The ROI data is sent to the L2 trigger, which uses all of

954 the available information within the ROI at full granularity and precision. The L2 trigger reduces  
955 the event rate from 75 kHz to 3.5 kHz, with an average processing time of 40 ms. The final stage of  
956 the HLT is the event filter, which reduces the event rate to 200 Hz. The event filter uses an offline  
957 analysis process to select fully rebuilt events which will be saved for further analysis.

958 All levels of the ATLAS trigger system depend on specialized electronics. Each detector front-  
959 end system has a specialized Readout Driver (ROD) which collects information from several front-  
960 end data streams at once. The ROD is composed of front-end analogue processing, an L1 buffer  
961 which retains the information long enough for the L1 trigger decision, and dedicated links which  
962 send the front-end L1 triggered data to Data Acquisition System (DAQ). Any digital signals are  
963 formatted as raw data before being transferred to the DAQ. The first stage of the DAQ temporarily  
964 stores the L1 data in local buffers. The ROI data is then requested by the L2 trigger, after which  
965 selected events are transferred to an event building system, before events passing the event filter  
966 are sent to the CERN computer center for permanent storage. The DAQ system not only allows  
967 for the readout of detector data, but is also responsible for the monitoring and configuration of  
968 the hardware and software components which make up the data readout system via the Detector  
969 Control System (DCS).

970 The DCS allows centralized control of all detector subsystems simultaneously. It continually  
971 monitors operational conditions, reports any abnormal behavior to the operator, and can perform  
972 both automatic and manual interventions. The DCS reports on real time detector conditions such  
973 as high or low voltage detector electronics, gas and cooling systems, magnetic field conditions,  
974 humidity and temperature. This information is continually monitored by experts in the ATLAS  
975 control room, so that action can be taken immediately to correct any issues that arise. The DCS also  
976 handles communication between detector systems, and other systems such as the LHC accelerator,  
977 the ATLAS magnets, and CERN technical services [34].

## Chapter 5: Particle Reconstruction and Identification

With a design luminosity of  $1.0 \times 10^{34} \text{ cm}^{-2}\text{s}^{-1}$ , and a peak Run-2 instantaneous luminosity of  $2.0 \times 10^{34} \text{ cm}^{-2}\text{s}^{-1}$ , reconstructing and identifying the products of LHC  $pp$  collisions is one of the most complex tasks for each LHC experiment. The accurate reconstruction and identification of physics objects lays the ground work for all subsequent physics analyses, so it is also one of the most fundamentally important tasks performed by an experiment.

Reconstruction is the process of combining raw and uncalibrated hits across various subsystems into specific unique objects. Two particular subsystems, the Inner Detector (ID) tracker and the calorimeters play particularly important roles and will be discussed in detail. Analysis of the properties of the reconstructed objects identifies them as photon, electrons, muons, or jets. While photons, electrons, and muons are fundamental particles, jets represent a collimated shower of many hadronic particles, whose definition is more flexible. Jet reconstruction, clustering and track association are all of particular import to jet identification, and to the later content of this thesis. Finally, reconstruction also identifies missing transverse energy  $E_T^{\text{miss}}$  in events, which is a crucial variable for BSM physics searches. Figure 5.1 shows how the physics objects listed here interact with various systems in the ATLAS detector.

### 5.1 Inner Detector Tracks

As the inner most layer of the detector, the ID measures charged particles close to the interaction point. The various hits of these charged particles throughout the ID are used to reconstruct *tracks* which give the trajectories of charged particles [45]. Track reconstruction begins by clustering hits in the Pixel and SCT detectors, and combining clusters from different radial layers of these detectors. The multi-layer clusters form track *seeds*, which provide initial estimates of mea-

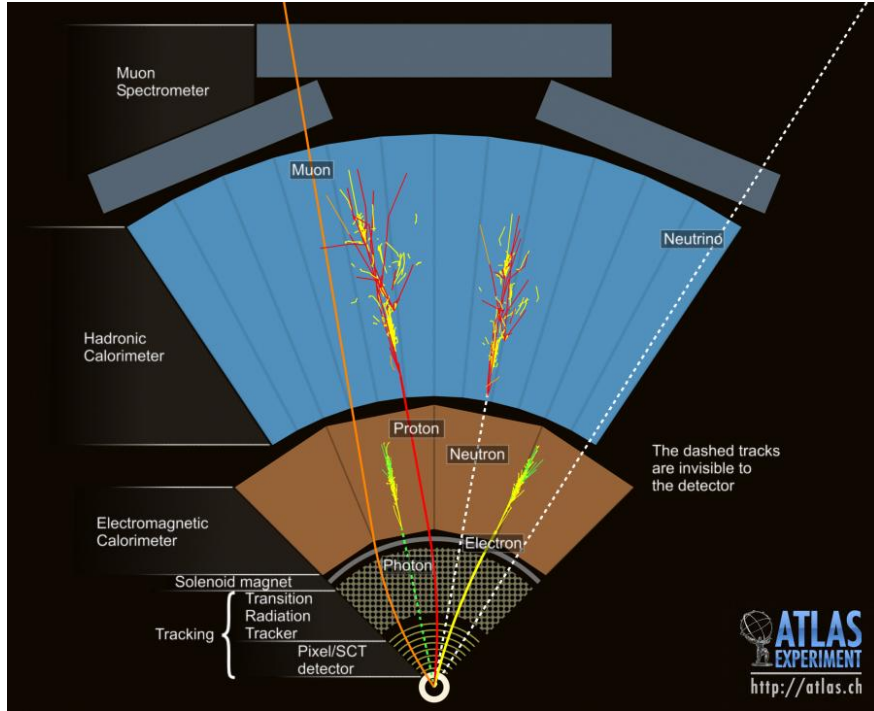


Figure 5.1: Graphic illustrating the various objects and high level features identified by ATLAS object reconstruction, and their interaction with different systems of the ATLAS detector [44]

1001   surements belonging to an individual track. The requirement of three points allows for a rough  
 1002   estimate of the track  $p_T$  to be made by calculating the curvature of the track and accounting of the  
 1003   magnetic field in the ID.

1004   Track seeds are subject to a variety of quality requirements, such as having a minimum esti-  
 1005   mated  $p_T$  and passing interaction region compatibility criterion. If these requirements are satisfied,  
 1006   the track seeds are passed to the track finding and fitting algorithms. The interplay of these three  
 1007   track reconstruction steps is illustrated in Figure 5.2.

## 1008   **5.2 Photons and Electrons**

1009   Photons and electrons shower in the LAr calorimeter, and are identified by the energy deposits  
 1010   they leave there. Energy deposits in a collection of nearby cells are termed *clusters*, which become  
 1011   the starting point for electron and photon reconstruction [46]. The clustering algorithm begins  
 1012   when the energy deposit in a certain cell exceeds the noise threshold with a significance of  $4\sigma$ .

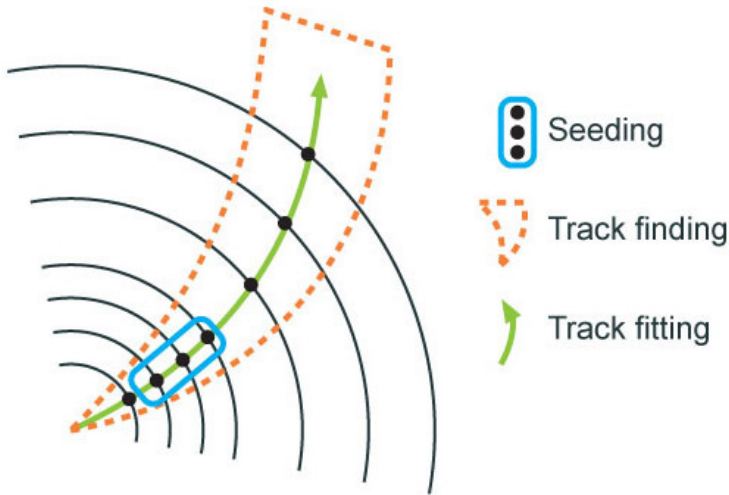


Figure 5.2: Track reconstruction seeding, finding and fitting illustration [45]

1013 The algorithm then collects neighboring cells which have an energy deposit exceeding the noise  
 1014 threshold with a significance of  $2\sigma$ , creating a topo-cluster. Next, these topo-clusters are matched  
 1015 to ID tracks, created as described in Section 5.1. The location of the topo-cluster defines a region  
 1016 of interest (ROI) in the ID, where additional modified track reconstruction algorithms are run in the  
 1017 case that no associated tracks are found. Any ID tracks associated to the topo-cluster are retrofitted to  
 1018 allow for additional energy loss due to bremsstrahlung. A converted photon track reconstruction  
 1019 algorithm is run to check for tracks coming from secondary vertices consistent with converted  
 1020 photons. The secondary vertices are constructed from two oppositely charged tracks consistent  
 1021 with a massless particle, or from one track without any hits in the innermost layer of the ID.

1022 For electron identification, the EM cluster is required to match ID tracks that originate from  
 1023 the primary vertex at the interaction point. For photon identification, the EM cluster can either be  
 1024 matched to tracks coming from a secondary vertex (converted photon), or matched to no tracks  
 1025 (unconverted photon). Figure 5.3 illustrates these three cases for EM object identification.

1026 *Superclusters* are built separately for photons and electrons, based on the combined topo-cluster  
 1027 and ID track information. First, the EM topo-clusters are tested to see if they meet the minimum  
 1028 requirements to become electron or photon seed clusters. For electrons, the cluster must have a  
 1029 minimum  $E_T$  of 1 GeV, and must be matched to a track with at least 4 hits in the silicon tracking

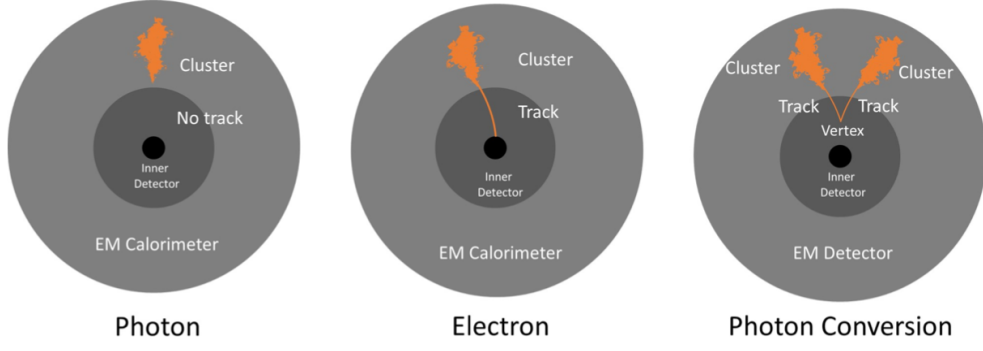


Figure 5.3: Three types of EM object candidates [47].

detectors. For photons, the cluster must have an  $E_T$  greater than 1.5 GeV. If the seed cluster requirements are met, the algorithm searches for satellite clusters, which can arise from bremsstrahlung radiation. If the satellite clusters pass the positional, energy and tracking requirements to be associated with the proto-cluster, they are combined into a supercluster.

Electron and photon objects are identified from the superclusters after energy calibration and position corrections are applied. Because photon and electron superclusters are built independently, some clusters can produce both a photon and an electron. In this case an ambiguity resolution procedure is applied to determine if the supercluster can be easily identified as only a photon (no tracks present) or only an electron (good tracks pointing to the primary vertex). In some cases, the identity of the cluster is still ambiguous, in which case both a photon and electron object are created for analysis and flagged as ambiguous. Energy, shower shape, and other analysis variables are calculated from the supercluster and saved with the electron or photon object.

### 5.3 Muons

Muons are identified through the tracks and energy deposits they leave in the ID, calorimeters, and Muon Spectrometer (MS). Muon identification begins in the Muon Drift Tube chambers by performing a straight line fit between the hits found in each layer, creating *segments*. Segments in the middle layers are then used as seeds for the track building algorithm, which searches for compatible combinations of segments based on their relative positions and angles [48]. A  $\chi^2$  fit is

1048 performed on each track candidate. Based on the  $\chi^2$  criteria, hits are removed or added such that  
1049 the track contains as many hits as possible while satisfying the fit criteria.

1050 The MS track candidates are combined with track information from the ID and calorimeters  
1051 according to various algorithms based on the information available from each subdetector. Four  
1052 different types of muons arise from the various reconstruction algorithms:

- 1053 • Combined muon: a muon track identified through independent track reconstruction in the  
1054 ID and MS, where the combined track is formed using a global refit that uses hit information  
1055 from both detectors. Most muons are constructed through an outside-in procedure, in which  
1056 a muon track candidate is identified in the MS and then an associated track is found in the ID.  
1057 A complementary inside-out procedure is also implemented and identifies additional muons.
- 1058 • Segment-tagged muon: an ID track is identified as a muon if when extrapolated out to the  
1059 MS (following the inside-out global fit procedure) it is matched to at least one local MS  
1060 segment.
- 1061 • Calorimeter-tagged muon: an ID track is identified as a muon if it is matched to a calorimeter  
1062 energy deposit that is compatible with a minimum-ionizing particle. This muon identifica-  
1063 tion has the lowest purity, but it used in regions where the MS has only partial coverage due  
1064 to cabling and service access routes.
- 1065 • Extrapolated muons: the muon is reconstruction only from the MS track and a requirement  
1066 on compatibility with the primary interaction point. The muon track is required to cross at  
1067 least two layers of the MS, and three layers in the forward region. These muons are mainly  
1068 used to extend muon acceptance into the region  $2.5 < |\eta| < 2.7$  where ID track information  
1069 is not available.

1070 Figure 5.4 illustrates the four types of muon reconstruction. Overlap between reconstructed  
1071 muons using ID tracks is resolved by giving preference to combined muons, then segment tagged  
1072 muons, and finally calorimeter tagged muons. Overlap with extrapolated muons is resolved by  
1073 giving preference to the muon with a better fit quality and higher number of tracks.

1074 All muon track candidates are required to pass a series of quality selections to be identified in  
 1075 the final muon collection. The primary qualities considered are the  $\chi^2$  goodness of fit for the global  
 1076 track, the difference in  $p_T$  measurement between the ID and MS tracks, and the ratio between the  
 1077 charge and momentum of the tracks. The quality requirements help reject hadrons, primarily from  
 1078 kaon and pion decays. Muons candidates consistent with cosmic rays are also rejected.

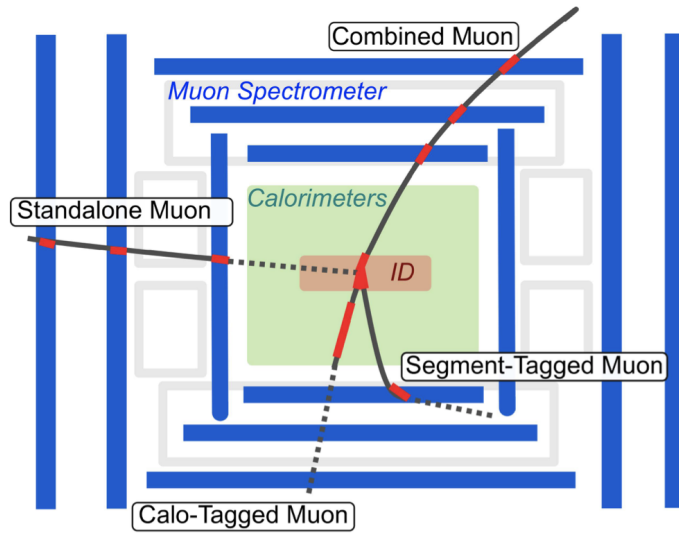


Figure 5.4: Four types of muon track candidates [49].

## 1079 5.4 Jets

1080 The protons accelerated in the LHC are composed of quarks and gluons, and thus their colli-  
 1081 sions often result in the release of energetic quarks and gluons, collectively termed *partons*. The  
 1082 energetic partons can radiate additional gluons, and these gluons can pair produce quarks in a pro-  
 1083 cess called *fragmentation*. Fragmentation continues until the energy drops sufficiently that color  
 1084 conservation plays a dominant role. At that point, additional quarks and gluons are produced from  
 1085 vacuum to create neutral color states for the fragmented collection of partons. This process is  
 1086 known as *hadronization* [50]. The hadronized partons compose a collimated stream of particles,  
 1087 known as a *jet*, which is then observed in the detector. The full process that produces jets is known  
 1088 as a *parton shower*, and is illustrated in Figure 5.5.

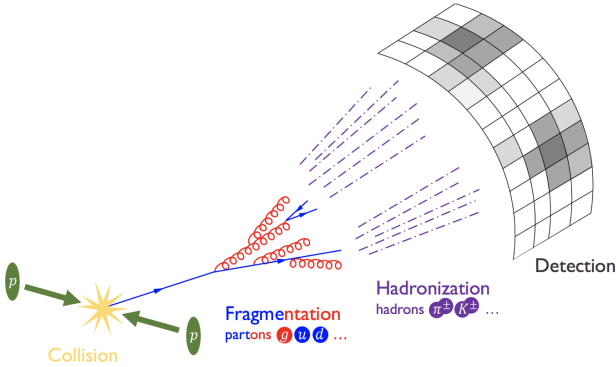


Figure 5.5: The fragmentation and hadronization processes undergone by a quark produced in a proton-proton collision [51].

1089     Jets are identified by the energy deposits they leave in the calorimeter, which are then matched  
 1090    to the tracks they leave in the ID. Jet reconstruction generally begins in the calorimeters, with the  
 1091    identification of *topo-clusters*. Then jet reconstruction algorithms combine calorimeter informa-  
 1092    tion with tracking information. The anti- $k_t$  algorithm [52] as provided by the FastJet library [53] is  
 1093    generally used by the ATLAS experiment, with varying reconstruction radius settings. There are a  
 1094    variety of jet collections depending on the exact usage of calorimeter and tracking information in  
 1095    the reconstruction. Some common collections include particle flow jets (PFlow), track calo-cluster  
 1096    jets (TCC), EM topo-cluster jets (EMTopo), and unified flow object jets (UFO). Only particle flow  
 1097    jets will be discussed in greater detail due to their importance in this analysis. The following sec-  
 1098    tions discuss jet identification in the calorimeters, particle flow jet construction using the anti- $k_t$   
 1099    algorithm, jet clustering and jet substructure characteristics.

1100    5.4.1 Calorimeter Clusters

1101    Jets are first identified by the energy deposits they leave in the calorimeters. The reconstruc-  
 1102    tion of jets in ATLAS begins with the construction of *topo-clusters*, which are topologically-grouped  
 1103    noise-suppressed clusters of calorimeter cells [54]. The topo-cluster seed is a cell with an energy  
 1104    that is at least 4× the average background noise level for the cell. Any cells adjacent to the seed  
 1105    cell in three dimensions are added to the cluster if they have an energy deposit that is at least 2x

1106 the average expected noise. This process is repeated, growing the cluster, until no adjacent cells  
1107 exceeding the energy deposit threshold remain. As a final step, all adjacent cells are added to the  
1108 topo-cluster, irrespective of their energy.

1109 The construction process for topo-clusters allows for the possibility that several independent  
1110 signatures are grouped into one topo-cluster. To correct for this, the topo-cluster is scanned for  
1111 local maximum, defined by any cell with energy  $> 500$  MeV, and no neighboring cells with greater  
1112 energy. If more than one local maximum is identified, the topo-cluster is split among the corre-  
1113 sponding energy peaks [55]. In the event that one cell neighbors two or more local maxima, the  
1114 cell is assigned to the two highest-energy clusters that is neighbors. This means each cell is shared  
1115 at most once, between at most two post-splitting topo-clusters.

1116 Two measurements for the total energy of the topo-cluster are considered. The raw, or electro-  
1117 magnetic (EM), scale simply considers the sum of energy from all cells in the topo-cluster. The  
1118 local cell weighting (LCW) scale first classifies clusters as electromagnetic or hadronic, and then  
1119 applies appropriate corrections for hadronic interactions in the jet energy calculation [54]. The  
1120 corrections are derived from Monte Carlo simulations, and account for the weaker response of  
1121 ATLAS calorimeters to hadronic interactions (ATLAS calorimeters are *non-compensating*), and  
1122 hadronic energy losses due to interactions with dead material [55].

#### 1123 5.4.2 Particle Flow Algorithm

1124 The calorimeters provide excellent jet energy resolution for high energy jets. However, the  
1125 granularity of the hadronic calorimeter is restricted to  $0.1 \times 0.1$  in  $\eta \times \phi$ . Combining the infor-  
1126 mation from the calorimeter with tracking information provides superior angular resolution and  
1127 energy resolution. The particle flow (PFlow) algorithm is one of a handful of algorithms which  
1128 can perform this task.

1129 An overview of the process is given in Figure 5.6. Tracks from the ID which are selected for the  
1130 PFlow algorithm are required to have at least 9 hits in the silicon detector, and missing pixel hits in  
1131 places where a hit would be expected. Additionally, the tracks have  $p_T > 0.5$  GeV, and  $|\eta| < 2.5$ .

1132 The algorithm then attempts to match these tracks to EM scale calorimeter topo-clusters. This  
1133 matching is performed using the distance metric

$$\Delta R' = \sqrt{\left(\frac{\Delta\phi}{\sigma_\phi}\right)^2 + \left(\frac{\Delta\eta}{\sigma_\eta}\right)^2} \quad (5.1)$$

1134 where  $\sigma_\eta$  and  $\sigma_\phi$  represent the angular widths of the topo-clusters, and  $\Delta\eta$  and  $\Delta\phi$  represent the  
1135 distance between the track, extrapolated to the second layer of the EM calorimeter, and barycenter  
1136 of the topo-cluster [56]. The topo-cluster closest to the track as measured by  $\Delta R'$  is considered  
1137 matched to the track. If no topo-cluster is found within the cone size of  $\Delta R' = 1.64$ , it is assumed  
1138 that particle which left the track did not form a topo-cluster in the calorimeter.

1139 The PFlow algorithm predicts the expected single topo-cluster energy for a given track, based  
1140 on the track momentum and topo-cluster position. This value is then compared to the observed  
1141 energy of the topo-cluster, and the probability that the particle energy was deposited in more than  
1142 one topo-cluster is evaluated. If necessary, the algorithm adds more topo-clusters to the track/topo-  
1143 cluster system, in order to account of the full shower energy of the track particle.

1144 To reduce the impact of double counting the energy of a given particle by including both its  
1145 tracker and calorimeter energy measurements, the calorimeter energy measurements associated to a  
1146 given track are subtracted from the total calorimeter measurement. If the expected energy deposited  
1147 by the particle exceeds the topo-cluster energy, the full topo-cluster is removed. If the expected  
1148 energy is less than the EM scale energy of all the considered topo-clusters, topo-cluster cells are  
1149 removed one by one, until the full expected energy deposit of the particle has been removed from  
1150 the calorimeter information. The resulting set of tracks and topo-clusters represent the event with  
1151 no double-counting of energy between subdetectors [56]. This information is passed to the jet-  
1152 finding algorithm.

#### 1153 5.4.3 Jet Clustering

1154 When a parton decays in the detector, its energy deposits often result in multiple calorimeter  
1155 clusters. For physics purposes, it is useful to combine clusters that likely resulted from an individ-

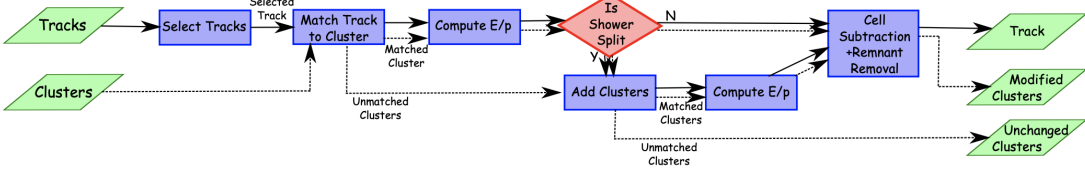


Figure 5.6: A flow chart illustrating the particle flow algorithm progression [56].

1156 ual parton decay, in order to reconstruct the parton. The process of grouping topo-clusters which  
 1157 were produced by the same parton decay is *jet clustering*.

1158       The anit- $k_t$  algorithm is the most commonly used algorithm for jet clustering in ATLAS. The  
 1159 anti- $k_t$  algorithm is based on sequential recombination algorithms [57]. A sequential recombina-  
 1160 tion considers the distance  $d_{ij}$  between objects  $i$  and  $j$  (particles or pseudojets), and the distance  
 1161  $d_{iB}$  between an object  $i$  and the beam line  $B$ . If  $d_{ij}$  between two objects is the smallest distance  
 1162 among those considered,  $i$  and  $j$  are combined into a pseudojet. The process continues until the  
 1163 smallest distance is  $d_{iB}$  at which point the object  $i$  is determined to be a jet and removed from the  
 1164 objects in consideration. The procedure is repeated with the remaining objects until there are none  
 1165 remaining [52].

1166       The anti- $k_t$  algorithm adopts this procedure, but modifies the distance measurements  $d_{ij}$  and  
 1167  $d_{iB}$  to consider the transverse momentum  $k_t$ :

$$d_{ij} = \min(k_{ti}^{2p}, k_{tj}^{2p}) \frac{\Delta_{ij}^2}{R^2}, \quad (5.2a)$$

$$d_{iB} = k_{ti}^{2p}. \quad (5.2b)$$

1168       The addition of the term  $p$  allows adjustments to algorithm which govern the relative power of  
 1169 the momentum versus the geometrical scale  $\Delta_{i,j}$ , which is defined as  $\Delta_{i,j} = (y_i - y_j)^2 + (\phi_i - \phi_j)^2$   
 1170 where  $y_i$  and  $\phi_i$  are respectively the rapidity and azimuth of particle  $i$  [52]. The radius parameter  
 1171  $R$  is chosen and determines the geometric cone size [57].

1172       In the case  $p = 1$  the inclusive  $k_t$  algorithm [57] is recovered, which is a standard sequential

combination jet clustering algorithm. In the case  $p = 0$ , the Cambridge/Aachen sequential combination algorithm [58] is recovered. The case  $p = -1$  gives rise to the anti- $k_t$  algorithm. The impact of this choice means that the distance  $d_{ij}$  between many soft particles is larger than between soft and hard particles. Therefore, soft particles tend to cluster with hard ones before they cluster with other soft particles. They key feature of this behavior is that soft particles do not modify the shape of the jets. This leads to the creation of circular conical jets, a desirable feature which sequential combination algorithms and cone algorithms struggle to achieve. Figure 5.7 compares anti- $k_t$  jet formation with the inclusive  $k_t$  and Cambridge/Aachen algorithms mentioned here, as well as the SIScone algorithm [59], which checks for sets of stable cones compatible with the observed radiation.

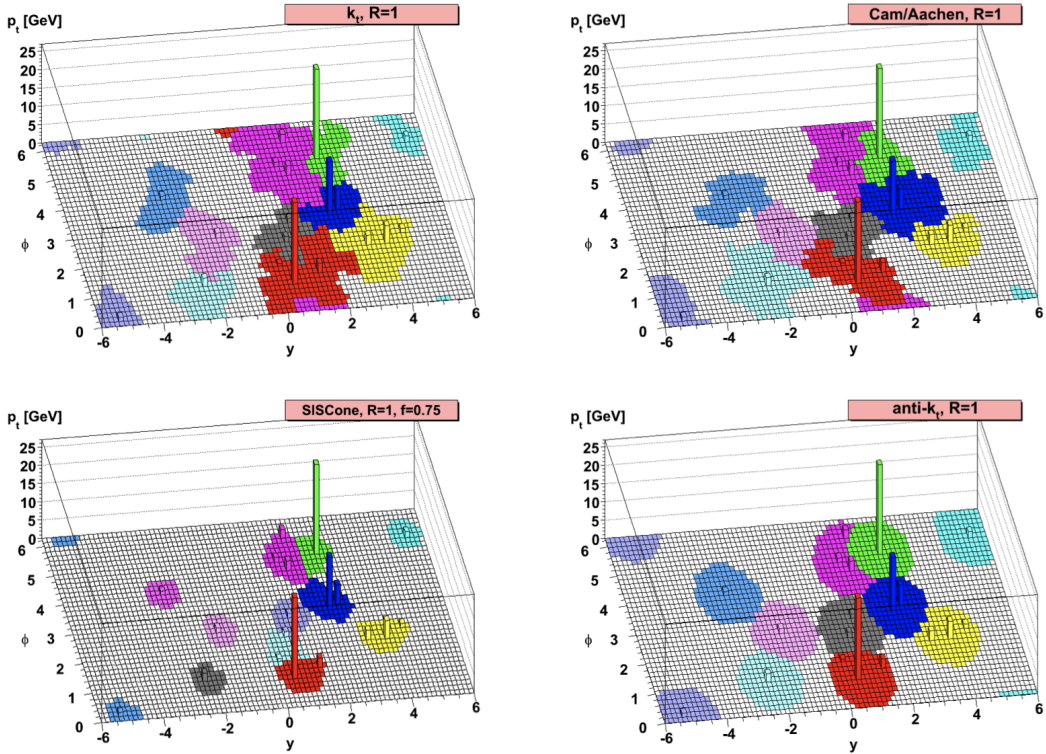


Figure 5.7: A comparison of jet clustering with four different jet algorithms. The anti- $k_t$  algorithm is observed to create the most conical jets, where the shape of the jet is immune to the presence of soft radiation [52].

Any useful jet clustering algorithm must satisfy the requirements of infrared safety and collinear

1184 (IRC) safety. Infrared safety implies that the resulting set of jets is unaltered by the presence of  
1185 additional soft particles in the list of seed clusters. As explained above, the anti- $k_t$  algorithm is  
1186 natural infrared safe. Collinear safety requires that the final set of jets is not impacted by collinear  
1187 splitting of one of the jets. If the hardest particle  $p_1$  is split into a collinear pair ( $p_{1a}, p_{1b}$ ) (as  
1188 is common in the fragmentation process for a hard parton), the jet clustering algorithm must  
1189 still recognize ( $p_{1a}, p_{1b}$ ) as the hardest jet in the collision. If another softer particle  $p_2$  with  
1190  $p_{t,1a}, p_{t,1b} < p_{t,2} < p_{t,1}$  is instead considered the hardest particle in the event, a different final  
1191 set of jets would be returned. Collinear safety is a requirement of perturbative QCD, to ensure  
1192 non-divergent higher-order calculations [60]. The anti- $k_t$  algorithm's tendency to cluster hard par-  
1193 ticles first ensures its collinear safety. By satisfying the IRC safety requirement, anti- $k_t$  jets can be  
1194 calculated using perturbative QCD, which improves comparisons with theory.

#### 1195 5.4.4 Ghost Track Association

1196 Once a collection of jets has been created, the jet objects can be studied at both the event-level  
1197 and the jet-level. In the event-level picture, the momentum, energy, and geometric orientation  
1198 of the jets within an event are considered. This yields important information about decay of any  
1199 resonant heavy objects, the total energy in the event, and the distribution of energy amongst the jets.  
1200 At the jet-level picture, the particles composing the jet are considered. The momentum, energy,  
1201 and geometric orientation of the particle tracks provides a low-level picture of the jet, which can  
1202 help determine if the properties of the jet are consistent with standard QCD, or if new physics  
1203 processes might be represented within the patterns found in the constituent particles. Jet-level  
1204 analysis is also widely used in flavor tagging.

1205 For anti- $k_t$  jets with a radius parameter  $R = 0.4$ , one way of studying the jet-level picture  
1206 is through considering the ghost-associated tracks. Track association is process of determining  
1207 which tracks should be considered associated with a given jet. In the ghost association algorithm,  
1208 the anti- $k_t$  clustering algorithm is used for the collection of tracks and calorimeter clusters [61].  
1209 However, the tracks are considered to have infinitesimal momentum (*ghosts*), so their addition to

1210 a jet object does not alter the four-momentum of the jet. This ensures the final jet collection is not  
1211 altered by the presence of the ghost tracks in the reclustering, but information about the associated  
1212 tracks for each reconstructed jet becomes available [62].

1213 Ghost tracks are of particular importance to this analysis, as a means of providing a low-level  
1214 picture of the shape of  $R = 0.4$  jets, and discriminating Standard Model QCD-like jets from dark  
1215 QCD-like jets.

## 1216 5.5 Missing Transverse Energy

1217 A simple principle leveraged in ATLAS physics analyses is checking for conservation of mo-  
1218 mentum among the products of any  $pp$  collisions. The initial state transverse momentum of any  
1219  $pp$  collision is always zero, so the transverse momentum of all final state particles should likewise  
1220 be zero. The missing transverse energy,  $E_T^{\text{miss}}$ , is determined by the magnitude of the negative  
1221 momentum vector sum of all final state objects resulting from the  $pp$  collision.

1222 Specifically, the objects considered in the  $E_T^{\text{miss}}$  calculation are photons, electrons, muons, jets,  
1223 and soft terms. The first four items comprise the hard components of the  $E_T^{\text{miss}}$  calculation, and  
1224 have been discussed previously in this chapter. The final item represents a collection of *soft terms*,  
1225 comprising any detector signals not associated to hard detector objects. These can be based on  
1226 unassociated tracks, or unassociated soft calorimeter clusters. Both are generally not used in the  
1227 same calculation to avoid double counting of soft terms. In this analysis the calorimeter cluster  
1228 soft terms are considered in the  $E_T^{\text{miss}}$  calculation.

1229  $E_T^{\text{miss}}$  can arise due to non-interacting Standard Model objects such as neutrinos, fake sources  
1230 such as mis-reconstructed objects and dead detector regions, or in some theories, non-interacting  
1231 BSM objects such as a dark matter candidate particles. To understand the amount of  $E_T^{\text{miss}}$  at-  
1232 tributable to detector noise and mis-reconstruction,  $E_T^{\text{miss}}$  is studied in  $Z \rightarrow \mu\mu$  where little real  
1233  $E_T^{\text{miss}}$  is expected [63]. As Figure 5.8 illustrates, the resolution of  $E_T^{\text{miss}}$  generally decreases as  
1234  $E_T^{\text{miss}}$  increases, due to detector resolution effects. As  $E_T^{\text{miss}}$  is an important quantity for most dark  
1235 QCD analyses, limitations in the accuracy of the  $E_T^{\text{miss}}$  calculation must be considered.

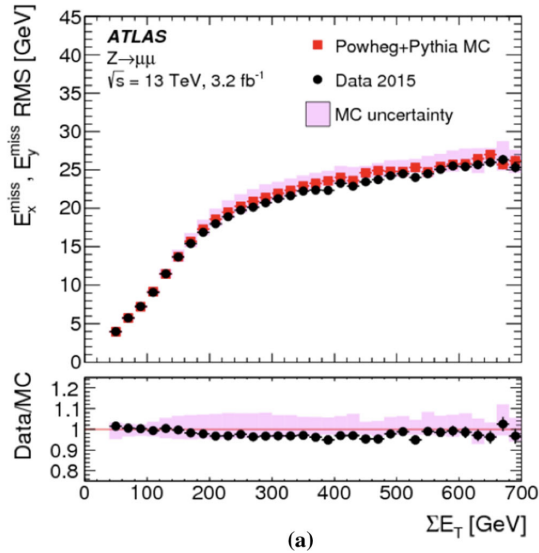


Figure 5.8: A comparison of MC simulation and data for  $Z \rightarrow \mu\mu$  events where real  $E_T^{\text{miss}} = 0$  [63]. The resolution of the missing energy in the transverse ( $x - y$ ) plane is observed to increase with increasing total  $\sum E_T$ .

1236

## **Part III**

1237

## **Search**

1238

1239

## Chapter 6: Monte Carlo and Data

1240 The search for semi-visible jets via s-channel production presented in the following chapters is  
1241 performed with  $139 \text{ fb}^{-1}$  of proton-proton collision data collected by the ATLAS detector during  
1242 Run 2 (2015 - 2018). The full Run-2 dataset is used for the final interpretation. Monte Carlo  
1243 (MC) simulations of background processes and the semi-visible jet signal process are used in the  
1244 development of the analysis strategy, and in the final interpretation to set limits on the observed  
1245 cross-section of the signal model. This chapter will provide details about the full Run-2 dataset,  
1246 and the background MC simulations, and the signal MC simulations used in this search.

1247 **6.1 Data**

1248 The  $139 \text{ fb}^{-1}$  of proton-proton collision data is selected according to the *good runs list* (GRL),  
1249 which identify runs with good detector conditions that are suitable for physics evaluation. Events  
1250 are further selected to pass a single-jet trigger selection, where events are required to have a jet at  
1251 trigger-level with a  $p_T$  that exceeds a certain value. The lowest  $p_T$  unprescaled single jet trigger  
1252 threshold for each period is as follows:

- 1253 • 2015:  $p_T \geq 360 \text{ GeV}$
- 1254 • 2016 & 2017:  $p_T \geq 380 \text{ GeV}$
- 1255 • 2017:  $p_T \geq 380 \text{ GeV}$
- 1256 • 2017 & 2018:  $p_T \geq 420 \text{ GeV}$

1257 A post-trigger selection of jet  $p_T > 450 \text{ GeV}$  ensures all these triggers are fully within their  
1258 efficiency plateaus. The jet collection used is anti- $k_t$  EM particle flow jets with a radius parameter  
1259 of  $R = 0.4$ , also referred to as small-R jets.

1260 Due to the variance in visible and invisible momenta due to the  $R_{inv}$  parameter of the signal  
1261 model, many signals also have significant  $E_T^{\text{miss}}$ . The use of a  $E_T^{\text{miss}}$  trigger to select events was  
1262 considered, and the single jet approach described here was found to preserve more signal events  
1263 across the grid, particularly in the high resonance mass and low  $R_{inv}$  region of phase space. These  
1264 studies are documented in Appendix A.

1265 The data are subject to a blinding strategy throughout the analysis design so as to mitigate  
1266 analyzer-induced bias. Blinded and unblinded region definitions are described further in Sec-  
1267 tion 8.1.

## 1268 6.2 Simulation

1269 Simulated events are generated with a variety of Monte Carlo (MC) generator processes that  
1270 run in stages. The  $pp$  hard scatter physics process is simulated, and the final state particles are  
1271 subsequently showered and decayed. This full description of the event is then propagated through  
1272 a detailed detector simulation based on GEANT4 [64]. The MC simulation is weighted to match  
1273 the distribution of the average number of interactions per bunch crossing  $\mu$  observed in collision  
1274 data.

1275 All simulated samples included in this analysis were produced with three different campaigns:  
1276 `mc20a` corresponds to 2015-2016 data-taking conditions, `mc20d` to 2017, and `mc20e` to 2018.  
1277 These three campaigns are weighted to the integrated luminosities of their respective data-taking  
1278 periods and combined to produce simulation for the entire Run 2 dataset. Simulated events are  
1279 reconstructed with the same algorithms run on collision data.

### 1280 6.2.1 Simulated Backgrounds

1281 Though the final background estimation is data-driven, background MC is studied for analysis  
1282 optimization and machine learning tool development.

1283 Dijet QCD is the dominant background process. QCD is simulated with PYTHIA8 [65], and  
1284 generated in approximate slices of  $p_T$ , to ensure high statistics across the momentum spectrum.

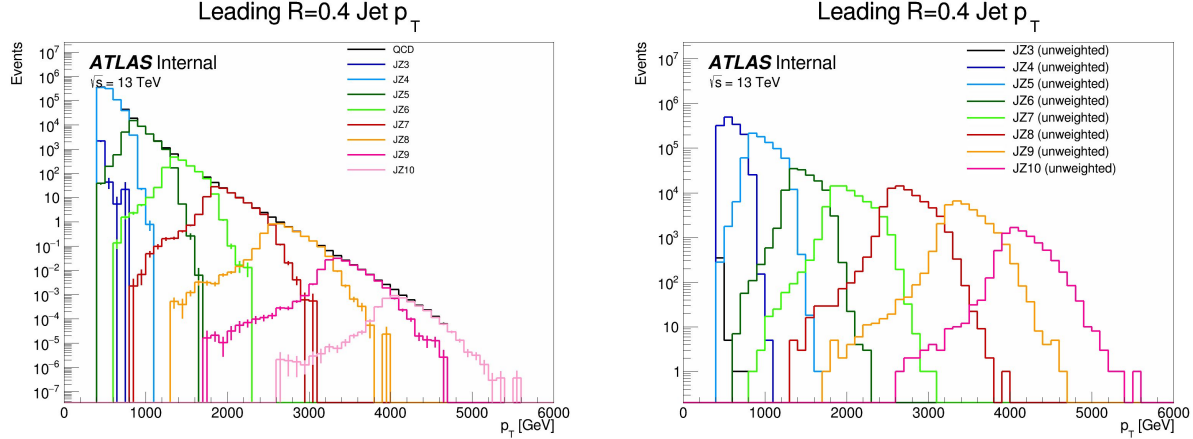


Figure 6.1: The transverse momentum slices of the QCD MC simulation, overlayed to show how they come together to create a smooth distribution (left) once weighted properly. The original unweighted distribution is shown on the right, illustrating the enhanced statistics for the high  $p_T$  range.

1285 The slices are then reweighted using MC generated event weights to create a physical distribution.

1286 Figure 6.1 illustrates the 8 momentum slices used in this analysis.

1287 Due to presence of  $E_T^{\text{miss}}$  in the SVJ signals, additional MC background processes are required  
 1288 to create a full picture of the relevant background. The  $Z \rightarrow vv$  process contributes to the back-  
 1289 ground due to its high missing energy. Leptonic W/Z decays and W/Z+jets are also included as  
 1290 they can contribute both additional missing energy and significant hadronic activity. Single top  
 1291 and  $t\bar{t}$  processes are also considered for their contribution to hadronic activity,. The background  
 1292 composition in the selected region (discussed in Section 8.1) is 76% QCD, 12% W/Z+jets, 8%  
 1293 top and  $t\bar{t}$  processes, and 4%  $Z \rightarrow vv$ . Figure 6.2 illustrates the background composition for the  
 1294 analysis.

## 1295 6.2.2 Signal Simulation

1296 The Hidden Valley signal model implementation is based on Ref [22]. The s-channel semi-  
 1297 visible jet model is governed by a number of parameters. The mass of the mediator  $m_{Z'}$  can be set,  
 1298 together with the couplings of the  $Z'$  to the visible and dark quarks  $g_q$  and  $g_{q_D}$ . The dark sector  
 1299 shower is governed by the number of dark colors  $N_{c_D}$ , the number of dark flavors  $N_{f_D}$ , and the

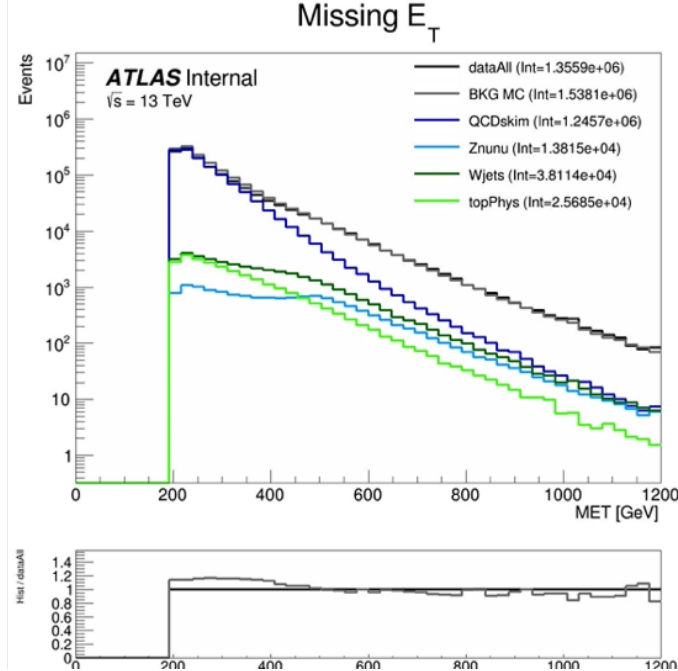


Figure 6.2: Background processes relevant to the SVJ signal. The agreement between the black line (data) and grey line (all MC processes combined) illustrates that this collection of background processes is sufficient to model the expected  $E_T^{\text{miss}}$  in the selected data events.

1300 dark sector confinement scale  $\Lambda_D$ . There is also the characteristic scale of the dark hadrons  $m_D$ ,  
 1301 which determines the mass of the dark hadrons, which can be pseudoscalars  $m_{\pi_D}$  or vectors  $m_{\rho_D}$ .  
 1302 Finally, the average fraction of invisible particles in the final state jet is dictated by  $R_{inv}$ .

1303 The chosen parameters for this model were carefully selected in collaboration with theorists to  
 1304 be compatible with the new benchmarks established in the 2021 Snowmass process [21]. These pa-  
 1305 rameters reflect extensive communication with the Snowmass, CMS, and theory teams. The signal  
 1306 generation allows for up to two initial state radiation jets, and uses an MLM merging scheme [65]  
 1307 to match jets to the original partons.

1308 The choices of fixed parameters for the Pythia8 HV model are summarized in Table 6.1. A  
 1309 detailed discussion of these parameters and their implications on the dark shower topology can be  
 1310 found in Ref. [21]. The mass choices for the dark quark and the dark hadrons are also summarized  
 1311 in Table 6.2.

1312 Note that the number of dark flavors differs from the Snowmass recommendation of  $N_{f_D} = 4$ .  
 1313 This change is minimal in impact because  $R_{inv}$  is set explicitly (rather than allowing it to arise

Parameter	Value
HiddenValley:Ngauge	3
HiddenValley:alphaOrder	1
HiddenValley:Lambda	10.0
HiddenValley:nFlav	2
HiddenValley:spinFv	0
HiddenValley:FSR	on
HiddenValley:fragment	on
HiddenValley:pTminFSR	1.1
HiddenValley:probVector	0.58

Table 6.1: Fixed parameters in the Pythia8 HV model

Parameter	Value [GeV]
$m_{\pi_D}$	17
$m_{\rho_D}$	31.77
$m_{q_D}$	10

Table 6.2: Values for  $m_{dark}$

naturally from the HV theory), and allows us to remain more comparable with the CMS semi-visible jets analysis and the ATLAS t-channel analysis.

The mediator mass  $m_{Z'}$  and the fraction of invisible particles in the final state  $R_{inv}$  vary, and are used to define the search grid.  $m_{Z'}$  varies between 2.0 TeV and 5.0 TeV, while  $R_{inv}$  varies from 0.2 to 0.8.  $R_{inv}$  values of 0.2, 0.4, 0.6, and 0.8 are generated for each  $m_{Z'}$  mass point. Table 6.3 illustrates the signal grid and the associated cross-section for each signal.

Samples are generated using MADGRAPH5 [66] version 2.9.9 interfaced to PYTHIA8.244P3 [65] for shower and hadronization with NNPDF23LO PDF [67] and the ATLAS A14 [68] to tune the underlying event data.

$m_{Z'}$ (GeV)	Cross section (fb)
2000	2.52e+2
2500	7.42e+1
3000	2.45e+1
3500	8.83e+0
4000	3.49e+0
5000	7.57e-1

Table 6.3: Mass points and cross sections of the SVJ search signal grid

1323

1324

## Chapter 7: Machine Learning Tools

1325 **7.1 Introduction**

1326 The search for semi-visible jets presents an opportunity to use novel machine learning (ML)  
1327 tools to uncover patterns in the behavior of dark QCD. The subtlety of the shower differences be-  
1328 tween dark and SM QCD motivates a complex model that can accept high-dimensional low-level  
1329 inputs to best understand key differences between signal and background correlations. Addition-  
1330 ally, the large number of theory parameters which can be chosen arbitrarily and affect the shape of  
1331 the dark QCD shower motivate exploring a data-driven machine learning approach, which could  
1332 be sensitive to a wider variety of dark QCD behavior.

1333 To this end, two machine learning approaches are developed for this search, which are used  
1334 in tandem. The first is a supervised ML method where the ML algorithm is built to maximize  
1335 exclusion sensitivity to the specific generated SVJ signal models used in this analysis. Here, su-  
1336 pervised refers to the use of full and correct labels for all events considered during model training,  
1337 which necessitates training over simulated data. The second is a semi-supervised method, where  
1338 training of the model is data-driven and labels are only partially provided during training. The  
1339 semi-supervised ML algorithm broadens the discovery sensitivity of the search, and reduces the  
1340 dependence on the exact theory parameters chosen for signal model simulation.

1341 The two different ML algorithms used in this approach will be explained in the following  
1342 sections, along with their application in the SVJ analysis strategy.

1343 7.1.1 Particle Flow Network (Supervised)

1344 **Architecture Fundamentals**

1345 A Particle Flow Network (PFN) [69] architecture is selected for two reasons: *permutation in-*  
1346 *variant input modeling* to best describe the events consisting of an unordered set of particles, and a  
1347 *low-level input modeling* using tracks to take advantage of the available high-dimensional informa-  
1348 tion to best exploit available correlations within the event. Permutation invariant input modeling  
1349 is an architecture priority as ordered input modeling has been observed to bias the performance of  
1350 low-level modeling tools as in [70]. Low-level input modeling is an architecture priority to capture  
1351 the intricacies of dark QCD showers which may not express themselves in higher level variables,  
1352 as explored in [22]. A comparison to a high-level *boosted decision tree* (BDT) is available in  
1353 Appendix B.3.

1354 The PFN is used to model input events as an unordered set of tracks. Given the inherently  
1355 unordered and variable-length nature of particles in an event, this choice of modeling as a *set*  
1356 can enable the model to better learn the salient features of the dataset that enable a signal-to-  
1357 background classification. Constructing the PFN involves the creation of new basis variables  $\oplus$   
1358 for each particle in the event. Permutation invariance is enforced by summing over the  $\oplus$  basis for  
1359 every particle in the event to create a new permutation invariant latent space basis  $O$ . Finally the  
1360 classifier  $F$  is a function of the sum over this new basis. The creation of the latent space basis  $O$   
1361 from  $M$  particles  $\vec{p}$  with  $d$  features each can be expressed as:

$$O(\{\vec{p}_1, \dots, \vec{p}_M\}) = \sum_{i=1}^M \Phi_i(\vec{p}_i) \quad (7.1)$$

1362 where  $\Phi : \mathbb{R}^d \rightarrow \mathbb{R}^l$  is a per particle mapping, with  $l$  being the dimension of the new basis  $O$ .  
1363 Figure 7.1 gives a graphical representation of the use of summation in the PFN over per-particle  
1364 information to create a permutation-invariant event representation.

1365 Figure 7.2 provides an annotated diagram of the PFN architecture as used in this analysis.

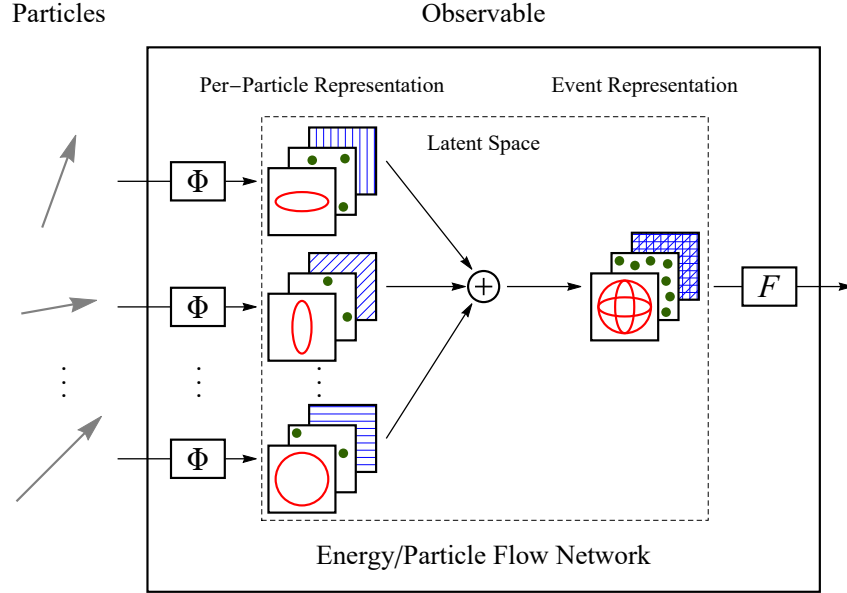


Figure 7.1: The Energy/Particle Flow Network concept, from Ref. [69].

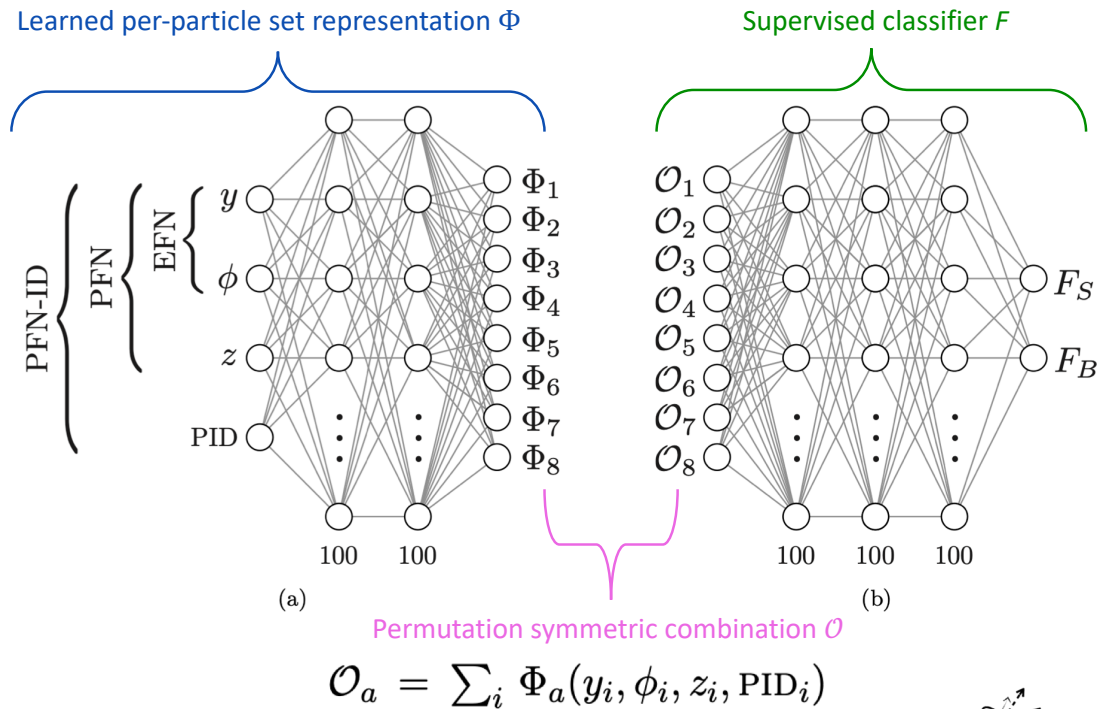


Figure 7.2: An annotated diagram of the PFN architecture.  $y$  and  $\phi$  represent geometric information for the input particles,  $z$  represents energy information, and PID encompasses any other particle ID information in the input.

1366 **Input Modeling, Scaling, and Rotation**

1367 In this implementation, the particle input information comes from all tracks associated to the  
1368 leading and subleading jets. The track association method is Ghost association, as discussed in  
1369 Section 5.4.4. A single jet tagger strategy was also considered, but utilizing tracks from both  
1370 leading jets creates a complete low-level picture of the event, which both focuses on the objects  
1371 most likely to be associated to the decay of the dark quark (as will be justified in Chapter 8)  
1372 and the relationship between those objects. If we consider the dijet topology of semi-visible jets  
1373 as illustrated in Figure 7.3, the advantage of modeling both leading jets simultaneously becomes  
1374 clear. In the semi-visible jet model presented in [22],  $E_T^{\text{miss}}$  in the event is expected to arise due to  
1375 an imbalance in the number of visible tracks of the two jets associated to the dark quark decay.

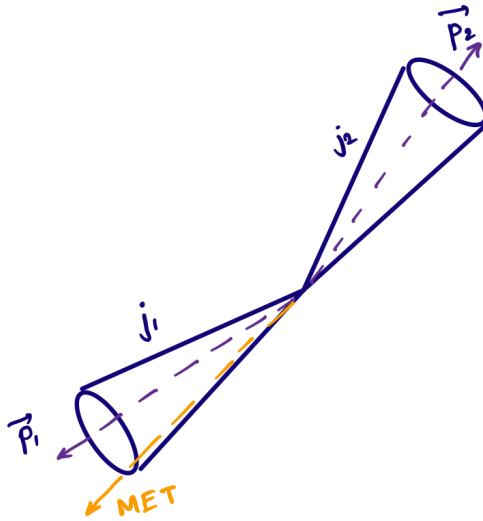


Figure 7.3: A illustration of the expected dijet behavior of semi-visible jets, where one jet is closely aligned with  $E_T^{\text{miss}}$ .

1376 Each track is described using six variables: the four-vector of the track ( $p_T$ ,  $\eta$ ,  $\phi$ , E), and the  
1377 track displacement parameters  $d_0$  and  $z_0$ , where  $d_0$  measures displacement in the radial direction  
1378 from the beamline and  $z_0$  measures displacement along the beamline from the primary interac-  
1379 tion point. Figure 7.4 illustrates these coordinates. Up to 80 tracks per jet are allowed, which is  
1380 a threshold chosen to generally include all the tracks in the jet, which leads to maximal perfor-

1381 mance. Figure 7.5 shows the track multiplicity in the leading and subleading jet for the signal and  
 1382 background samples used in training.

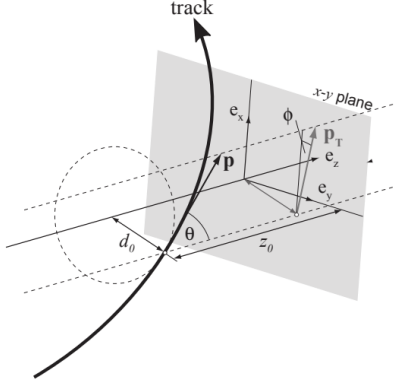


Figure 7.4: Illustration of track coordinates  $d_0$  and  $z_0$ .

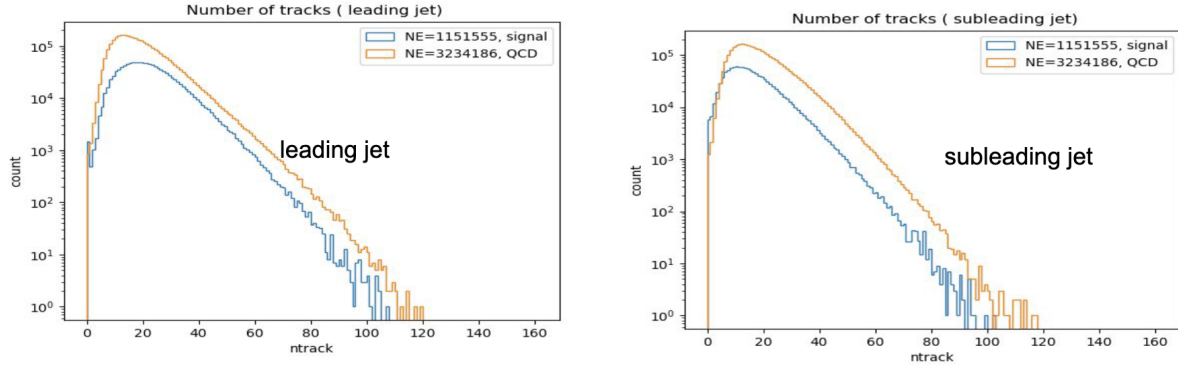


Figure 7.5: Distributions of the track multiplicity in the leading and subleading jets, comparing signal and background PFN training samples.

1383 These tracks (up to 160 total) are the input to the PFN. Referencing Equation 7.1, this corre-  
 1384 sponds to  $M = 160$  and  $d = 6$ . The two leading jets and their associated tracks are rotated so  
 1385 that the center of the system is aligned with  $(\eta, \phi) = (0, 0)$ . Each track is normalized to its relative  
 1386 fraction of the total dijet system energy and transverse momentum- this enforces agnosticism to the  
 1387 total energy and transverse momentum of the event. The rotation and scaling are motivated by the  
 1388 procedures described in [69] to improve the optimality of the PFN learning. Figure 7.6 illustrates  
 1389 the rotation process.

1390 Finally, each of the 6 track variables is scaled so that its range is  $[0,1]$ . This is a common

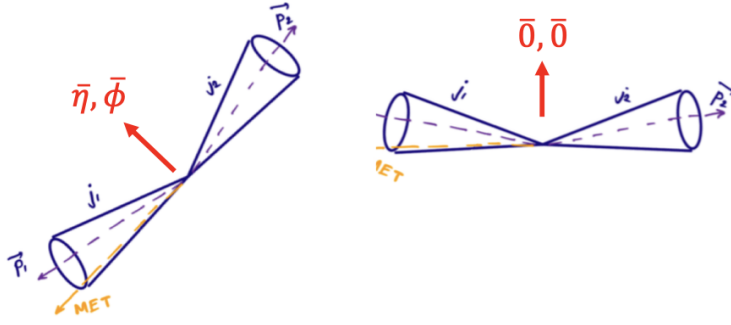


Figure 7.6: A diagram demonstrating how the two jet system is rotated in  $(\phi, \eta)$ .

1391 preprocessing step that ensures the input data is bounded over a similar range, so that arbitrarily  
 1392 large values don't develop an outsized impact on the model. Figure 7.7 show each of 6 track  
 1393 variables before and after scaling and rotation have been applied, demonstrating the impact of  
 1394 these procedures, as well as the track level similarities differences between the background SM  
 1395 QCD processes and the signal SVJ processes. Figure 7.8 illustrates that the data is well modeled  
 1396 by the MC at track level.

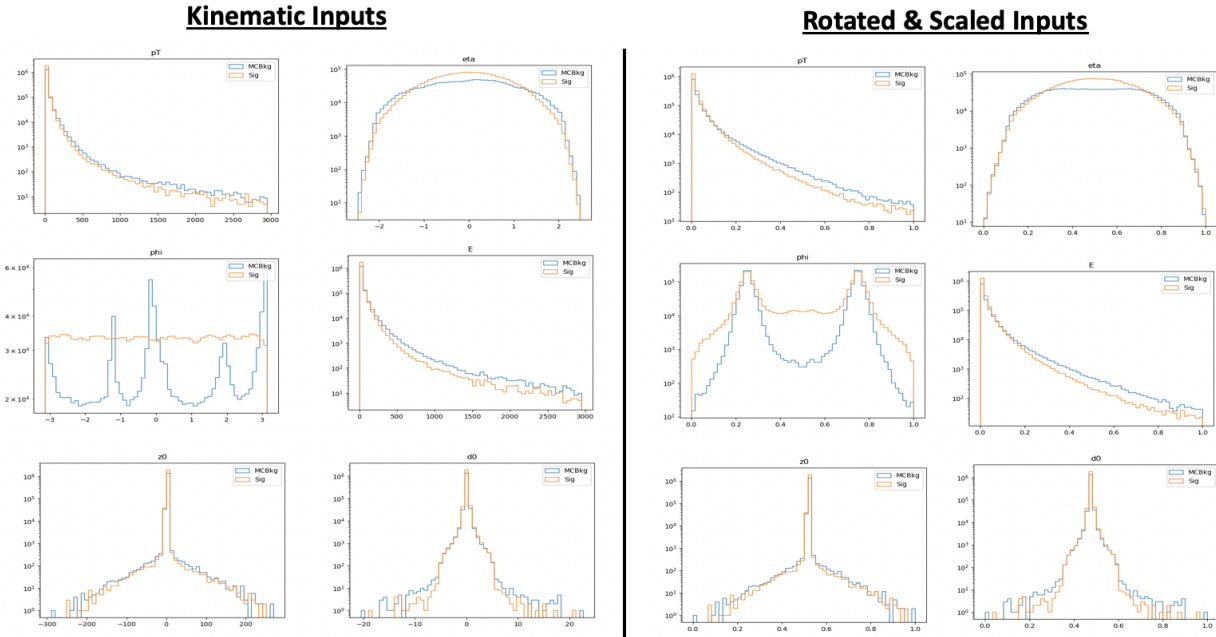


Figure 7.7: The 6 PFN track variables in background MC and signal MC. There are some differences between signal and background, but the track kinematics are largely similar.

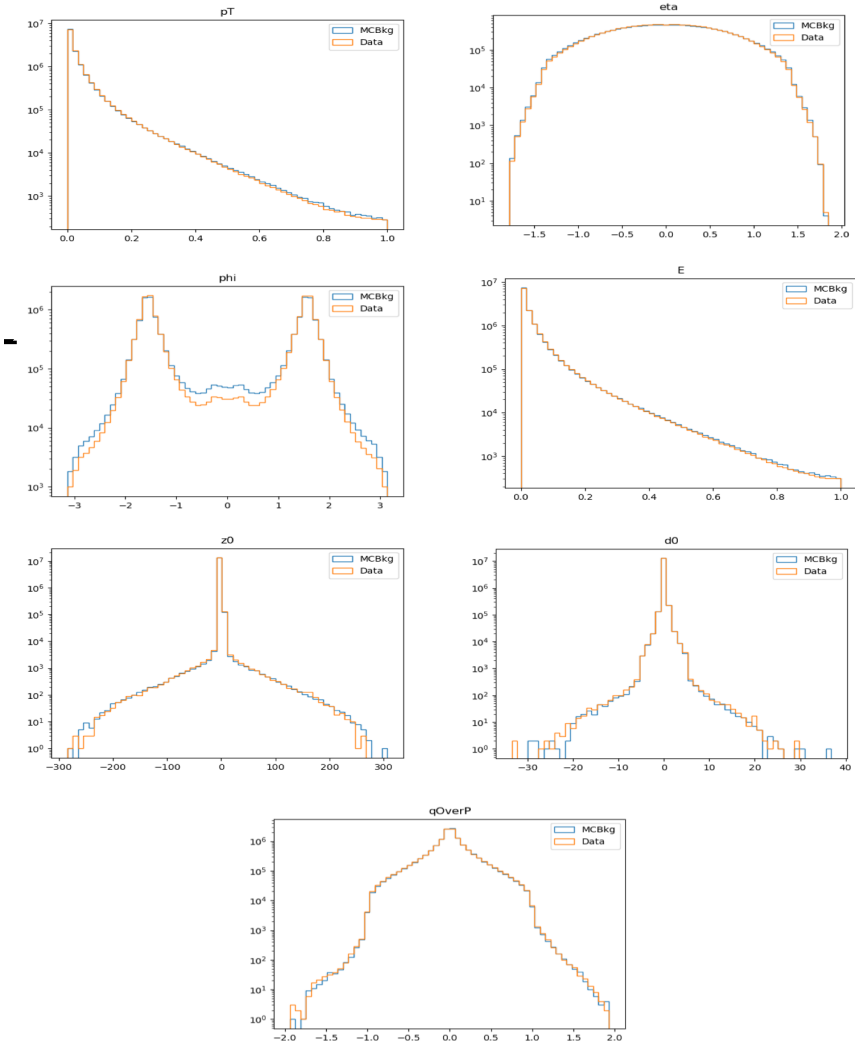


Figure 7.8: The 6 PFN track variables in data and background MC, after the scaling and rotation procedure is applied. There is excellent modeling of the data by the MC within the track variables. The slight discrepancy in the phi distribution is due to the modeling of dead TileCal cells by the QCD MC, which will be discussed in Chapter 8. The level of discrepancy is determined to be within tolerance given that the final result will be data driven and the QCD model is used in the PFN training only.

1397    **Training**

1398    As seen in Figure 7.2, two separate architectures are defined and combined to do the super-  
1399    vised training. The PFN uses a masking layer to suppress any zero-padded inputs, making the  
1400    architecture length agnostic. The masking layer ignores any all-zero inputs in the summation layer.  
1401    Additionally, The summation layer in the PFN enforces permutation invariance, so the network is  
1402    unordered. The  $\Phi$  network has 3 dense layers of dimensionality 75 with RELU activation, with  
1403    27.5k trainable parameters and an output  $\Phi$  latent space dimension of 64.

1404    The classifier  $F$  network similarly has 3 dense layers with 75 nodes with RELU activation, and  
1405    a final softmax layer to determine the event-level classification with a categorical cross-entropy  
1406    loss. The Adam optimizer is used with an initial learning rate of 0.001.

1407    The PFN is trained in a fully supervised way using SVJ signal MC and QCD MC events. Al-  
1408    though several SM processes are expected to contaminate the SR (see Chapter 8), QCD is the dom-  
1409    inant background. Training against a QCD-only sample is determined to produced better results  
1410    than training on a more complete background - when training with a background which repre-  
1411    sents samples that are more enriched in  $E_T^{\text{miss}}$ , the ability of the PFN to identify high  $E_T^{\text{miss}}$  signals  
1412    is reduced. When training with a QCD-only background, there is greater contamination from  
1413     $E_T^{\text{miss}}$  enhanced backgrounds in the final SR - however the increased signal acceptance means that  
1414    overall sensitivity is still higher with a QCD-only training. This can be seen in the comparison of  
1415    output classifier distributions in Figure 7.9.

1416    500k events from both background and signal are used in training, where the signal is a com-  
1417    bined file of all simulated signal points and the full QCD background which is sampled according  
1418    to it's MC weights to produce the proper  $p_T$  input shape. A study was done to check the optimality  
1419    of the inclusive signal model PFN as compared to one trained on high and low  $R_{inv}$  points sepa-  
1420    rately, to better capture the differences in high and low  $E_T^{\text{miss}}$  across signals and backgrounds, but  
1421    a small effect is found and the decision is taken to keep the inclusive model (Appendix B.2).

1422    The network is trained for 100 epochs. A train/test/validation split of 78%, 20%, and 2% is used  
1423    for the final PFN training. Figure 7.10 shows the loss during training, which is stable and flattens

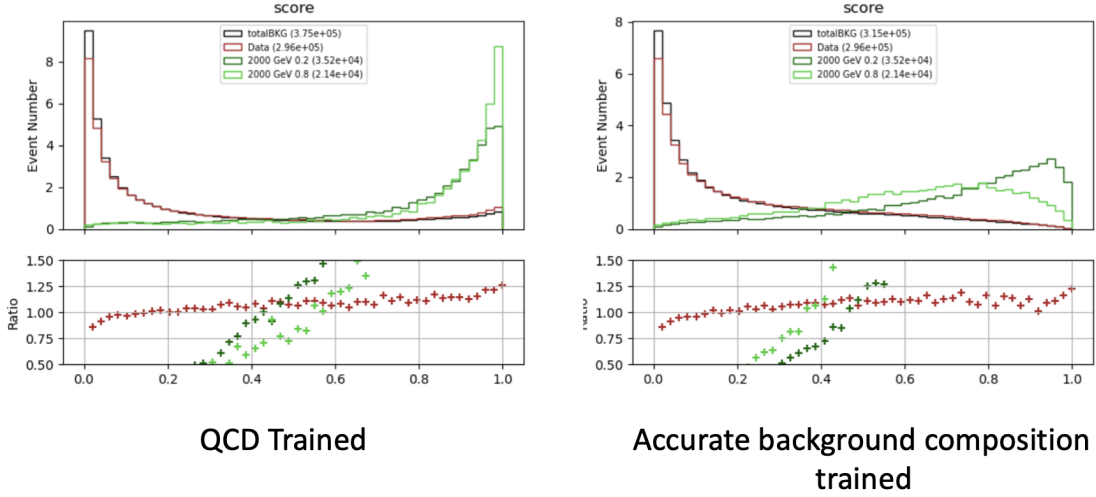


Figure 7.9: PFN score for background MC, data, and signal, comparing a PFN training on QCD-only vs all-background MC samples. The average AUC for the QCD-only training (left) is 0.93, while the average AUC for the mixed background training (right) is 0.84. The sensitivity estimate across the grid is better for the QCD-only training - from the distribution we can conclude that this is because the sensitivity to MET enhanced signals is greatly reduced.

1424 by the end of training, and the final evaluated losses that provide signal-background discrimination  
 1425 over the test set.

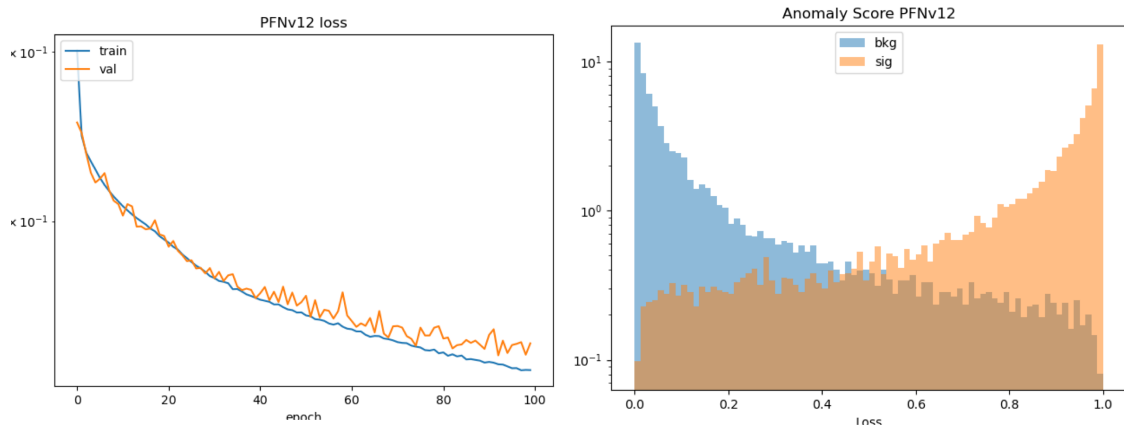


Figure 7.10: PFN architecture loss during training as a function of epoch (left) and the evaluated loss over the signal and background (right).

1426 Optimization studies were performed on the PFN, varying the number of training epochs, num-  
 1427 ber of training events, batch size, learning rate, number of neurons, and dimension of the  $\Phi$  space.  
 1428 A summary of these studies is presented in Appendix B.2. The model presented here represents an  
 1429 optimal choice across these parameters.

1430 **Performance**

1431 The performance of the PFN can be assessed via the area-under-curve (AUC) of the receiver  
1432 operating characteristic (ROC) associated to evaluating the PFN on the test set of signal and back-  
1433 ground events. Figure 7.11 shows the ROC curve of the PFN when classifying the QCD back-  
1434 ground from the combined signal, with an AUC of 0.93. Figure 7.12 shows the AUC of the PFN  
1435 across the SVJ signal grid, demonstrating strong discrimination capability even in the varying cor-  
1436 ners of phase space. Figure 7.13 shows the output score distribution in two signals, data, and the  
1437 total background MC. A selection of PFN score  $> 0.6$  for all SR events is chosen to maximize  
signal sensitivity across the grid.

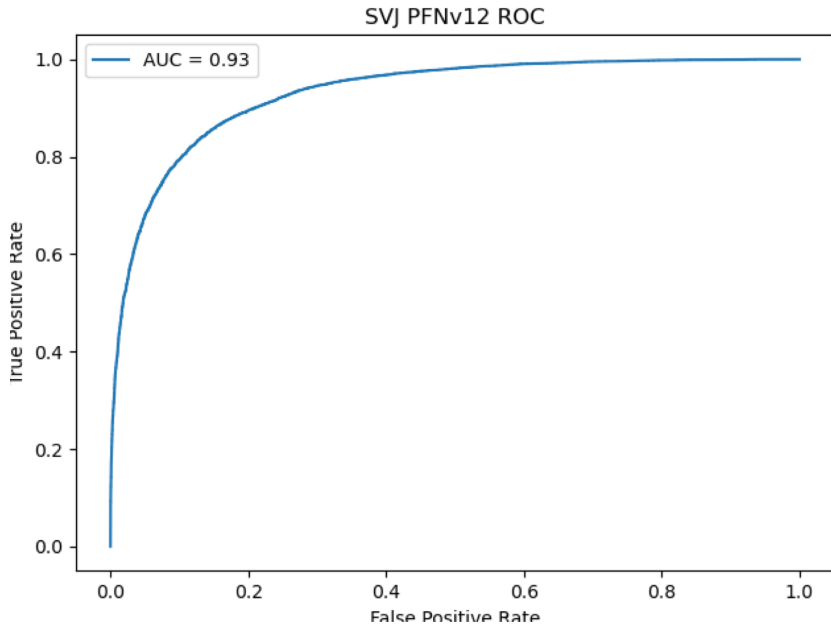


Figure 7.11: ROC the PFN score for combined signal (true positive) and QCD background (false positive).

1438

1439 Another supervised approach was studied using a BDT as the primary selection tool, trained  
1440 over high-level variables describing each event. Studies comparing the PFN and BDT approaches  
1441 are provided in Appendix B.3. Ultimately the low-level high-dimensional approach offered by the  
1442 PFN was selected for its increased performance and lessened kinematic dependence.

1443 Appendix B shows more studies on the ML methods and comparisons of varying approaches.

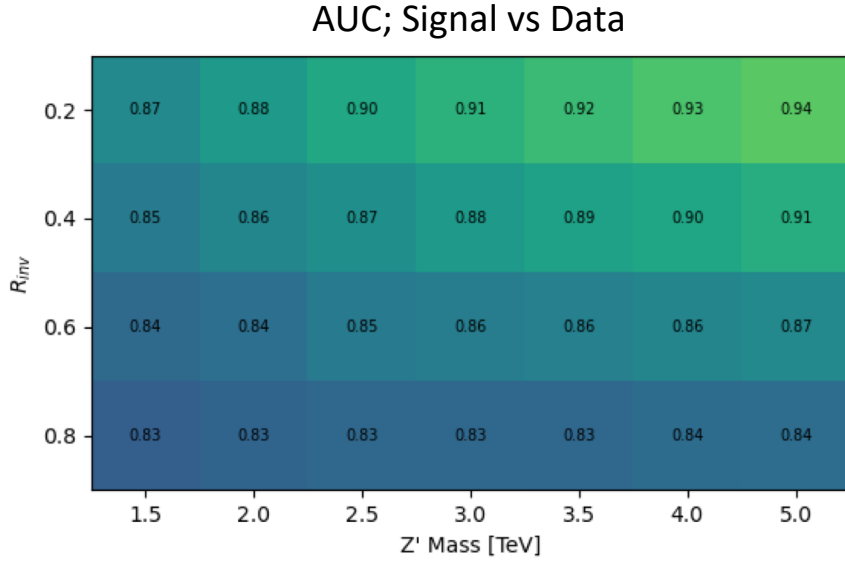


Figure 7.12: AUC from the PFN score for each signal in the SVJ grid, shown versus the QCD-only training sample.

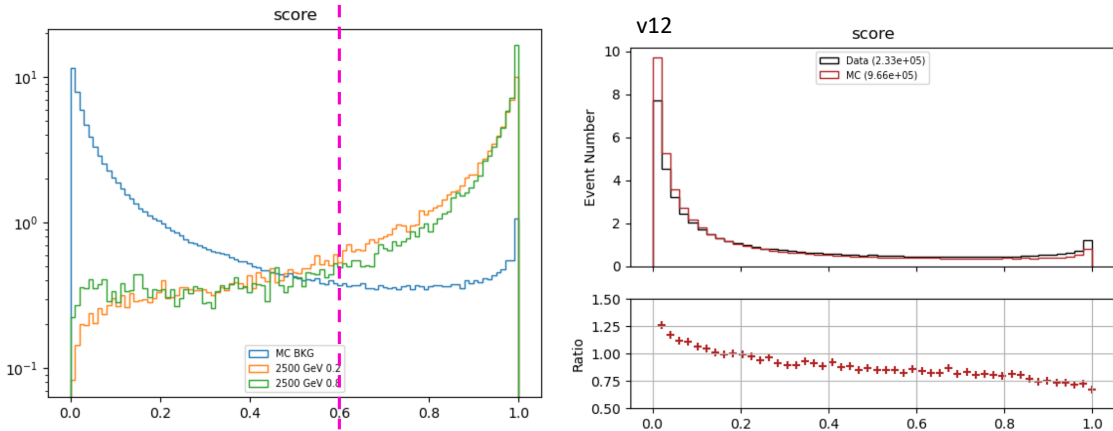


Figure 7.13: PFN score for two signals and the total background MC (top), and between data and MC (bottom). The difference between data and MC efficiency is minimal (< 5%).

1444 7.1.2 ANTELOPE (Semi-supervised)

1445 The semi-supervised analysis approach broadens the discovery sensitivity of the search through  
1446 the use of semi-supervised ML, where training of the model is data-driven and labels are only  
1447 partially provided during training. While broad sensitivity is a general key goal of LHC searches,  
1448 it is particularly motivated in the case of dark QCD models, which can lead to widely varying  
1449 topologies depending on the values of model parameters. In the case of SVJs, the  $R_{inv}$  fraction in  
1450 the jet can dramatically vary the  $E_T^{\text{miss}}$ , shower shape, and other key features, making it difficult to  
1451 find a single standard analysis variable that can distinguish all signal topologies from QCD.

1452 **Architecture Fundamentals**

1453 The model-independent search region of this analysis is implemented with a novel ML ap-  
1454 proach that builds on the ANTELOPE architecture to construct a tool that is capable of performing  
1455 low-level anomaly detection with permutation-invariant inputs. This tool, referred to as **ANomaly**  
1456 **deTEction on particLe flOw latent sPacE (ANTELOPE)**, is a custom solution designed for this  
1457 analysis.

1458 ANTELOPE uses the supervised signal vs. background training of the PFN network described  
1459 in the previous section to generate a permutation invariant latent space that is representative of the  
1460 original input variables, encodes the input events into these latent space variables  $O$ , and trains a  
1461 *variational autoencoder* (VAE) over the events modeled as PFN latent space variables. A VAE  
1462 is a common architecture used for anomaly detection and data-driven ML training. It has been  
1463 used in previous ATLAS searched to model jet level information, such as the search presented  
1464 in [71] using the recurrent architecture described in [70]. One of the limitations of a recurrent  
1465 architecture is the need to order the low level inputs, which affects the performance of the tool. Jet  
1466 constituent information is intrinsically unordered, and therefore a permutation invariant approach  
1467 removes this element of arbitrary decision making from the modeling process. A visual example  
1468 of the ANTELOPE inputs is given in Figure 7.14.

1469 The input to the model is the same 6 track variables for the leading 160 tracks of the leading

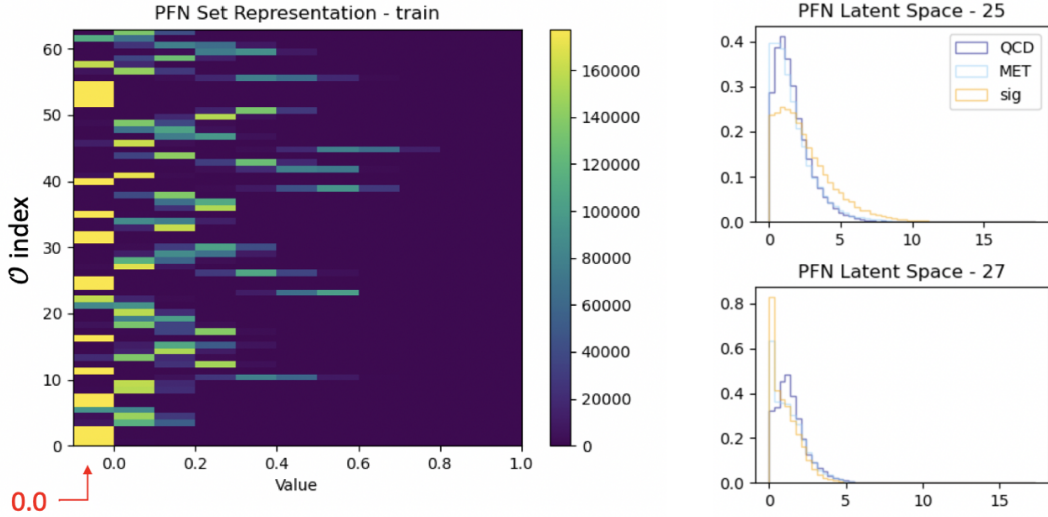


Figure 7.14: A visual representation of the 64 PFN latent space variables which create the input of the VAE component of ANTELOPE. The left shows a 2D histogram of the PFN latent space index (0-63) versus the value assumed by that index. The right shows 1D histograms of two particular PFN latent space variables.

1470 two jets, as presented in Section 7.1.1. The track information is encoded to the PFN  $\Phi$  latent  
 1471 space using the pre-trained  $\Phi$  network (trained according to the steps outline in Section 7.1.1. The  
 1472 resulting  $\Phi$  basis is summed to created the fixed length symmetric representation  $O$ . The VAE is  
 1473 then trained in an unsupervised way using inputs encoded to  $O$  from data events only. The VAE is  
 1474 given no knowledge of the signal model during training. It is able to perform anomaly detection  
 1475 through an encoder stage which does a lossy compression on the input to a lower-dimensional  
 1476 latent space, and a decoder stage that samples from that latent space and generates an output of the  
 1477 original dimensionality. By using the reconstruction error as a loss, this process enables the VAE  
 1478 to develop a knowledge of the underlying data structure, thereby isolating new out-of-distribution  
 1479 events by their high reconstruction error. This strategy is semi-supervised because the tool has  
 1480 some knowledge of correct labels (eg. through the PFN latent space embedding) but is followed  
 1481 by a data-driven unsupervised stage.

1482 Figure 7.15 provides a diagram of the ANTELOPE architecture.

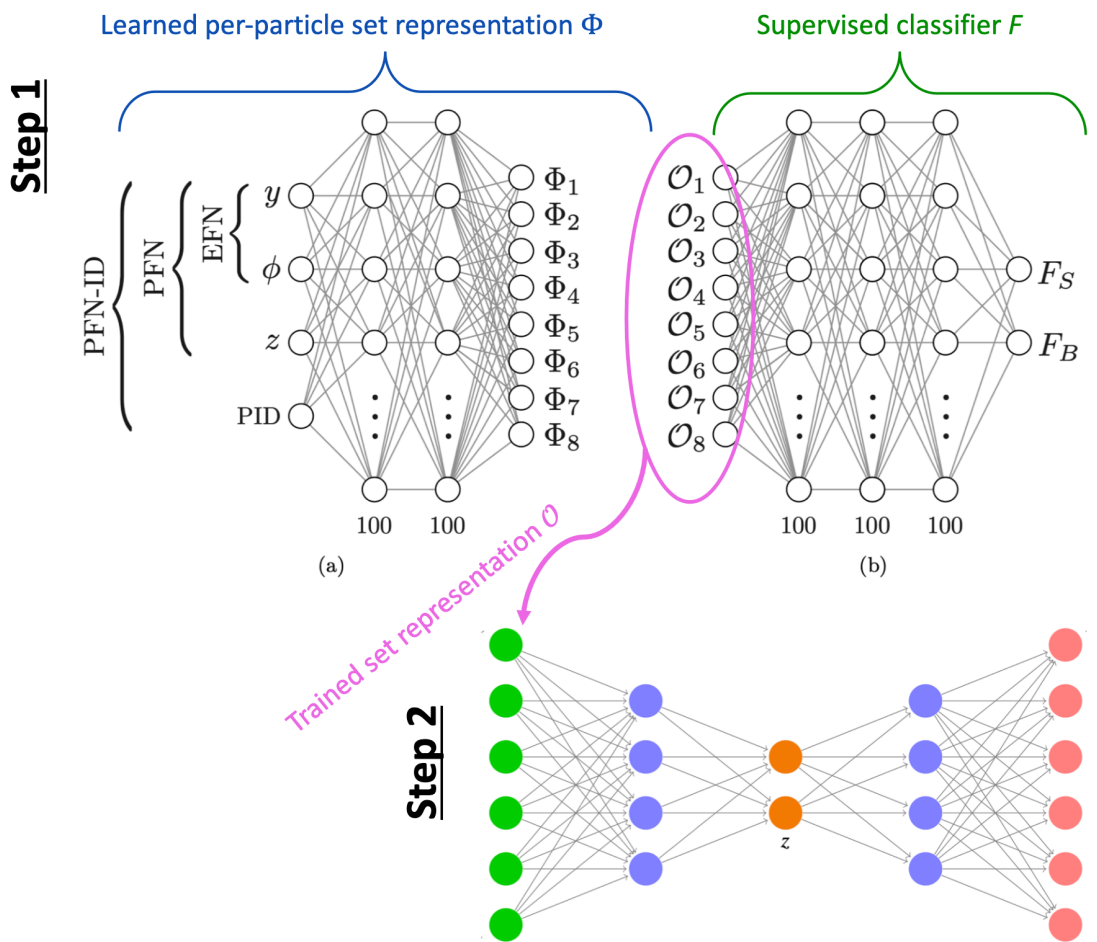


Figure 7.15: An annotated diagram of the ANTELOPE architecture.

1483 **Training**

1484 The VAE stage of the ANTELOPE network is trained directly over a subset of data events  
1485 at preselection (6.7 million available, 500,000 used, with a 80% / 20% training/test split). The  
1486 input dimensionality of the VAE has to match the encoded  $\Phi$  dimension of the PFN, in this case  
1487 64. The encoder has an encoding layer that brings the dimensionality to 32, and a final layer that  
1488 compresses to the latent space dimension of 12. The network is trained for 50 epochs, with a  
1489 learning rate of 0.00001. The loss  $\mathcal{L}$  is the sum of two terms, the mean-squared error (MSE) of  
1490 input-output reconstruction, and the Kullback-Leibler divergence (KLD).

$$\mathcal{L} = \sum_i L_i = \sum_i |\Phi_i^2 - \Phi'_{\ell i}|^2 + \lambda D_{\text{KL}} \quad (7.2)$$

1491 As the PFN inputs are sufficiently normalized to remove any spurious information from train-  
1492 ing, no additional normalization is applied to the PFN encoded inputs. The final ANTELOPE score  
1493 used in the analysis is produced by applying a log + sigmoid transformation function to the total  
1494 evaluated loss  $\mathcal{L}$ .

Figure 7.16 shows the loss during training.

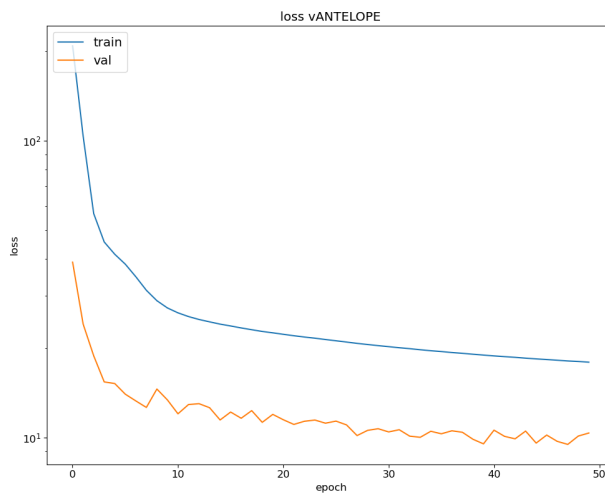


Figure 7.16: ANTELOPE architecture loss during training as a function of epoch.

1495

1496 **Performance**

1497 As with the PFN, the ANTELOPE performance is assessed via the area-under-curve (AUC) of  
1498 the receiver operating characteristic (ROC) associated to evaluating the ANTELOPE on the test  
1499 set of signal and background events. Figure 7.17 shows the output score distribution in data and  
1500 total background MC, showing a very flat ratio and motivating the use of MC for studies of the  
1501 ANTELOPE score.

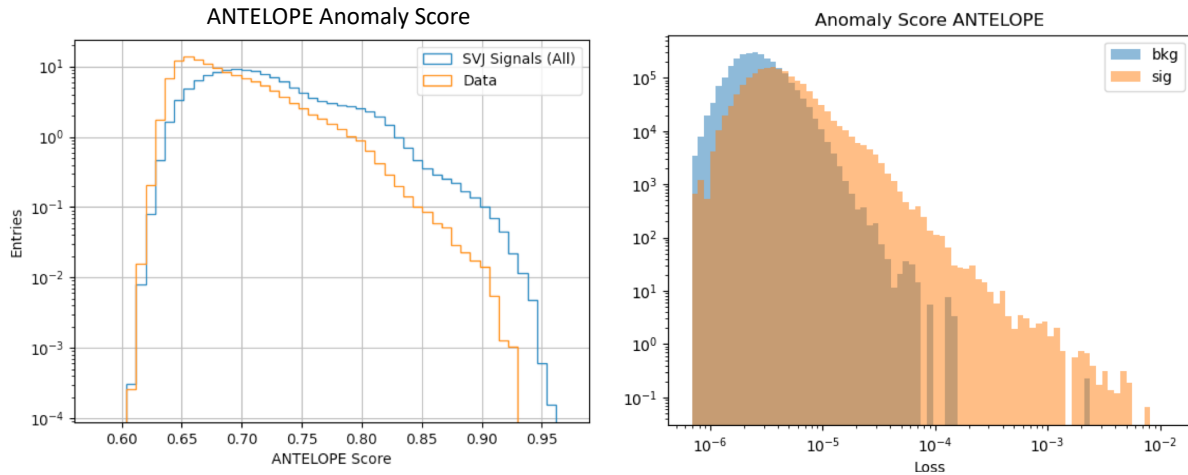


Figure 7.17: ANTELOPE score distribution comparing data and the total background MC (left), with good agreement observed between data and simulated background, and comparing all background MC to signals (right), revealing good discrimination power.

1502 Figure 7.18 shows the AUC of the ANTELOPE across the SVJ signal grid, demonstrating  
1503 strong discrimination capability even in the varying corners of phase space. Compared to the  
1504 supervised PFN method, the ANTELOPE is not as performant (as expected due to the absence of  
1505 signal model in training). However, a selection on events with high ANTELOPE score nonetheless  
1506 provides a 10-40% increase in signal significance by removing background and isolating the long  
1507 tail of anomalous events.

1508 **Model Independence** The unsupervised component of training the ANTELOPE network is ex-  
1509 pected to give it a more generalized sensitivity to new physics with  $E_T^{\text{miss}}$  and jet activity, beyond  
1510 the scope of the SVJ grid. To assess this, alternative signal models are evaluated with the trained

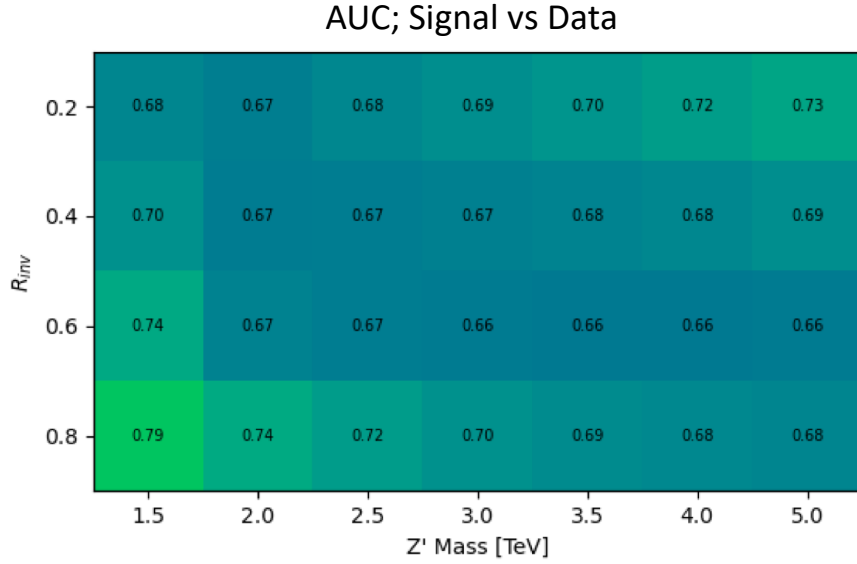


Figure 7.18: AUC from the ANTELOPE score for each signal in the SVJ grid.

1511    ANTELOPE network, as optimized for the SVJ grid, and their sensitivity in the analysis selection  
 1512    is evaluated.

1513    The following alternate signal models were considered:

- 1514    •  $Z' \rightarrow t\bar{t}$
- 1515    •  $W' \rightarrow WZ$
- 1516    • Gluino pair production  $\rightarrow$  R-hadron + LSP ( $E_T^{\text{miss}}$ ) with gluino masses 2000/3000 GeV, LSP  
 1517    mass 100 GeV, and lifetime 0.03 ns (LSP = *lightest supersymmetric particle*)
- 1518    • Emerging jets s-channel with mass 1000 GeV and lifetime 1ns

1519    Figure 7.19 shows the distribution of these signals in the PFN score and the ANTELOPE score.  
 1520    This comparison reveals that ANTELOPE is sensitive to  $E_T^{\text{miss}}$  in the event; it classifies signals  
 1521    with no real  $E_T^{\text{miss}}$ , like the all-hadronic  $Z'$  and  $W'$  decays (given our imposed lepton veto) as  
 1522    data-like, but the distributions for signals with  $E_T^{\text{miss}}$  such as SVJs, R-hadrons, and emerging jets  
 1523    have distributions with higher anomaly score tails.

1524    Figure 7.20 shows a comparison of the sensitivity of the PFN and ANTELOPE regions across  
 1525    a variety of signals, including the combined SVJ signal used to train the PFN. The benefit of the

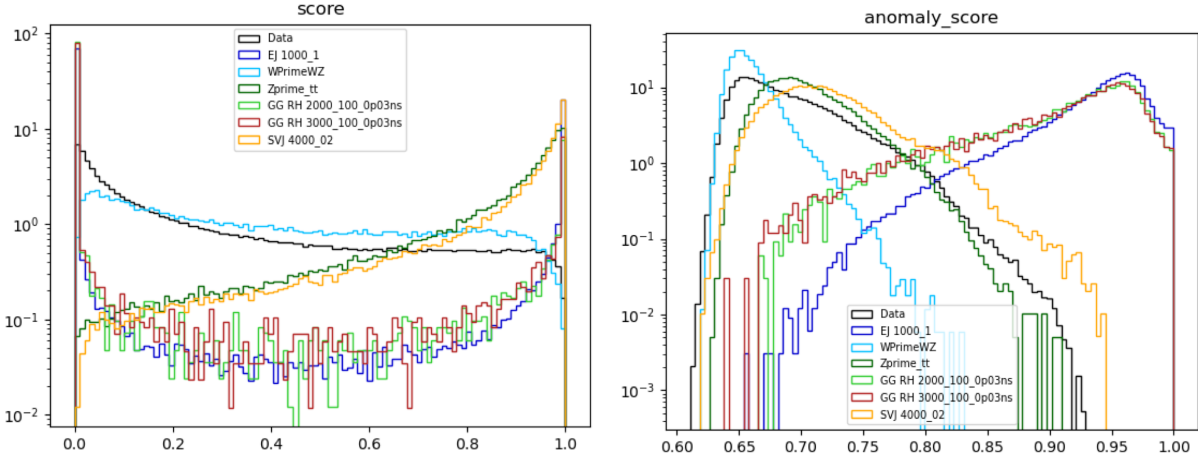


Figure 7.19: Comparing data and the alternate signal models for the PFN score (left) and ANTELOPE score (right). The emerging jet signal is an example of the gain of the model-independent ANTELOPE approach, where it has a bimodal shape in PFN score but is clearly tagged as anomalous by ANTELOPE.

1526 unsupervised stage of ANTELOPE in enhancing model independence is clearly seen through the  
 1527 boost in performance for other signal models, namely the gluino and emerging jet signals, which  
 1528 have more  $E_T^{\text{miss}}$  than the  $W'$  and  $Z'$  signals (all-hadronic) that were also tested. As commented  
 1529 above, the PFN outperforms ANTELOPE as expected, because it was designed explicitly for the  
 1530 task of classifying SVJs from background, demonstrating the power of supervised learning for the  
 1531 model-specific approach.

$\text{sig eff} / \sqrt{\text{bkg eff}}$  for respective score cut (0.6 PFN, 0.7 ANTELOPE)

	EJ 1000	WprimeWZ	Zprime tt	GG RH 2000	GG RH 3000	SVJ
PFN	0.57	0.65	1.92	0.30	0.32	1.97
ANTELOPE	1.73	0.07	0.84	1.72	1.72	1.13

Figure 7.20: Comparing data and the alternate signal models in terms of sensitivity ( $S/\sqrt{B}$ ) for the PFN and ANTELOPE tools, applying the selection that is used in the analysis. The ANTELOPE network is found to provide significant added sensitivity to alternate signals such as the gluino→R-hadron and emerging jets, which have higher  $E_T^{\text{miss}}$  than the SVJs.

1532 Studies on the ANTELOPE architecture and comparisons to other methods can be found in  
 1533 Appendix B.1.

1534

1535

## Chapter 8: Analysis Strategy

1536 This chapter will present the strategies used to isolate ATLAS data events most consistent with  
1537 the SVJ model and to estimate the relevant background. The data and MC samples discussed in  
1538 Chapter 6 are studied to create the analysis strategy, and the ML scores discussed in Chapter 7  
1539 are used to isolate the most signal like events. A *preselection* selects events consistent with the  
1540 SVJ topology based on basic features of the jets and  $E_T^{\text{miss}}$ . Preselected events are then split into  
1541 a *control region* (CR), *validation region* (VR), and *signal region* (SR). The CR is used to estimate  
1542 the estimate the background and the VR is used to validate that estimation. The SR is blinded  
1543 during the development of the analysis strategy, and only unblinded to make the final measurements  
1544 presented in Chapter 9. The final result is a polynomial fit of the *transverse mass* ( $m_T$ ) spectrum  
1545 in the SR. The preselection, region definitions, and polynomial fit will be discussed in detail in the  
1546 following sections.

1547 **8.1 Preselection**

1548 The preselection isolates the phase space of events that most closely match the SVJ signal  
1549 topology. Each cut was determined to reduced the background and enhance signal sensitivity. The  
1550 list of preselection cuts and the motivation behind each cut are as follows. Here “jets” refer to  
1551 anti- $k_t$  R=0.4 jets, as discussed in Chapter 5.

- 1552 • At least 2 jets; in order to reconstruct the resonance mass  
1553 • Leading jet  $p_T > 450$  GeV; to ensure the use of the trigger in its efficiency plateau  
1554 • Subleading jet  $p_T > 150$  GeV; to mitigate the presence of non-collision background (Ap-  
1555 pendix B.7.1)

- 1556     •  $|\eta_{j1,j2}| < 2.1$ ; to ensure jets are fully within the tracker
- 1557     •  $\Delta Y < 2.8$  (difference in rapidity between the two leading jets); to ensure central production  
1558                 associated to hard scatter
- 1559     •  $E_T^{\text{miss}} > 200 \text{ GeV}$ ; to focus phase space on events with dark particles
- 1560     •  $m_T > 1.2 \text{ TeV}$ , to ensure a smoothly falling  $m_T$  distribution for fitting (Section 8.4)
- 1561     • At least 3 tracks for each of the two leading jets; to ensure good modeling
- 1562     •  $\Delta\Phi(j_1, j_2) > 0.8$ ; to mitigate the presence of non-collision background (Appendix B.7.1).

A cutflow showing the impact of these cuts in data and signal is shown in Figure 8.1.

Data			Signals - All		
Cut	Statistics	Rel. Efficiency	Cut	Statistics	Rel. Efficiency
Initial	1.71E+10		Init	6.66E+05	
Trigger	3.45E+08	0.0202	Trigger	2.83E+05	0.4245
N. jets $\geq 2$	2.84E+08	0.8233	N. jets $\geq 2$	2.80E+05	0.9896
Leading Jet Pt $> 450 \text{ GeV}$	1.49E+08	0.5235	Leading Jet Pt $> 450 \text{ GeV}$	2.21E+05	0.7900
Lead Jet Eta $< 2.1$	1.42E+08	0.9528	Lead Jet Eta $< 2.1$	2.19E+05	0.9922
Subleading Jet Eta $< 2.1$	1.33E+08	0.9432	Subleading Jet Eta $< 2.1$	2.12E+05	0.9661
$dY < 2.8$	1.29E+08	0.9628	$dY < 2.8$	2.11E+05	0.9934
MET $> 200$	7.07E+05	0.0055	MET $> 200$	1.13E+05	0.5370
$mT > 1200$	5.38E+05	0.7613	$mT > 1200$	7.94E+04	0.7019
Jet2 pT $> 150$	5.03E+05	0.9343	Jet2 pT $> 150$	6.14E+04	0.7739
$d\Phi(j_1, j_2) > 0.8$	4.97E+05	0.9890	$d\Phi(j_1, j_2) > 0.8$	5.83E+04	0.9494

Figure 8.1: Preselection cutflow for data (left) and signal (right).

1563

1564     With the exception of the cuts necessary to reduce the non-collision background, all cuts were  
1565     verified to enhance signal sensitivity by improving  $s/\sqrt{b}$ , a standard estimate of discovery sensi-  
1566     tivity, where  $s$  is the number of signal events and  $b$  is the number of background events. The cuts  
1567     on  $\Delta Y$  and  $E_T^{\text{miss}}$  were optimized to enhance  $s/\sqrt{b}$ , and the other cuts were informed by the physics  
1568     motivations provided above.

1569     Vetos are applied to reject any events where an error for a subdetector is flagged. This covers  
1570     Tile/LAr calorimeter errors, single event upsets in the SCT, and incomplete events. To reject non-  
1571     collision backgrounds (NCB), such as calorimeter noise, beam halo interactions, or cosmic rays,

1572 the standard ATLAS event cleaning procedure is applied. As this analysis is very dependent on  
1573  $E_T^{\text{miss}}$  associated to jets, the TIGHT event cleaning working point is applied. Tight cleaning requires  
1574 jets to pass a stricter set of quality requirements compare to the LOOSE cleaning option. Due to  
1575 the alignment between jets and  $E_T^{\text{miss}}$  in this phase space, it was found that two additional cuts  
1576 (indicated above) are needed to remove NCB. The process for selecting these cuts is presented in  
1577 Appendix B.7.1.

1578 The two leading in  $p_T$  jets in the event are considered as the dark quark candidates. This choice  
1579 was determined by truth studies matching the dark quark to reconstructed jets in simulation, which  
1580 indicate that the leading  $p_T$  assignment allows for high accuracy in  $\Delta R$  matching to dark quarks.  
1581 These studies can be found in Appendix C.

1582 Figure 8.2 and Figure 8.3 show the distribution of signal and background MC in several key  
1583 analysis variables after preselection is applied.

## 1584 **8.2 SVJ Fit and Discovery Analysis Strategies**

1585 As was introduced in Chapter 7 this analysis is interested in achieving dual goals: to make  
1586 the best possible measurement of the SVJ signal model generated for this analysis, and to broadly  
1587 search for any signals consistent with dark QCD behavior and inconsistent with a Standard-Model-  
1588 only background hypothesis. To this end, two parallel analysis strategies are developed.

1589 The SVJ Fit strategy uses the supervised PFN ML score in defining the signal region. Recall,  
1590 the PFN is trained over simulated MC background and a combination of all MC SVJ signals. This  
1591 gives this ML tool high sensitivity to the particular nuances of the SVJ shower predicted by the  
1592 modeled theory. In addition to using the supervised ML tool, the SVJ Fit analysis strategy sets  
1593 limits on the expected cross-section of each signal point in the SVJ signal grid. To achieve this, the  
1594 shape of the SVJ signals are considered in the final fit, as will be elaborated on Section 8.5.1. The  
1595 combination of the supervised PFN ML score and the signal-shape-sensitive fitting strategy allows  
1596 for the greatest possible sensitivity to the modeled signal process, thus allowing the analysis the  
1597 best chance at discovery of this model, or enabling the analysis to set the best possible limits on

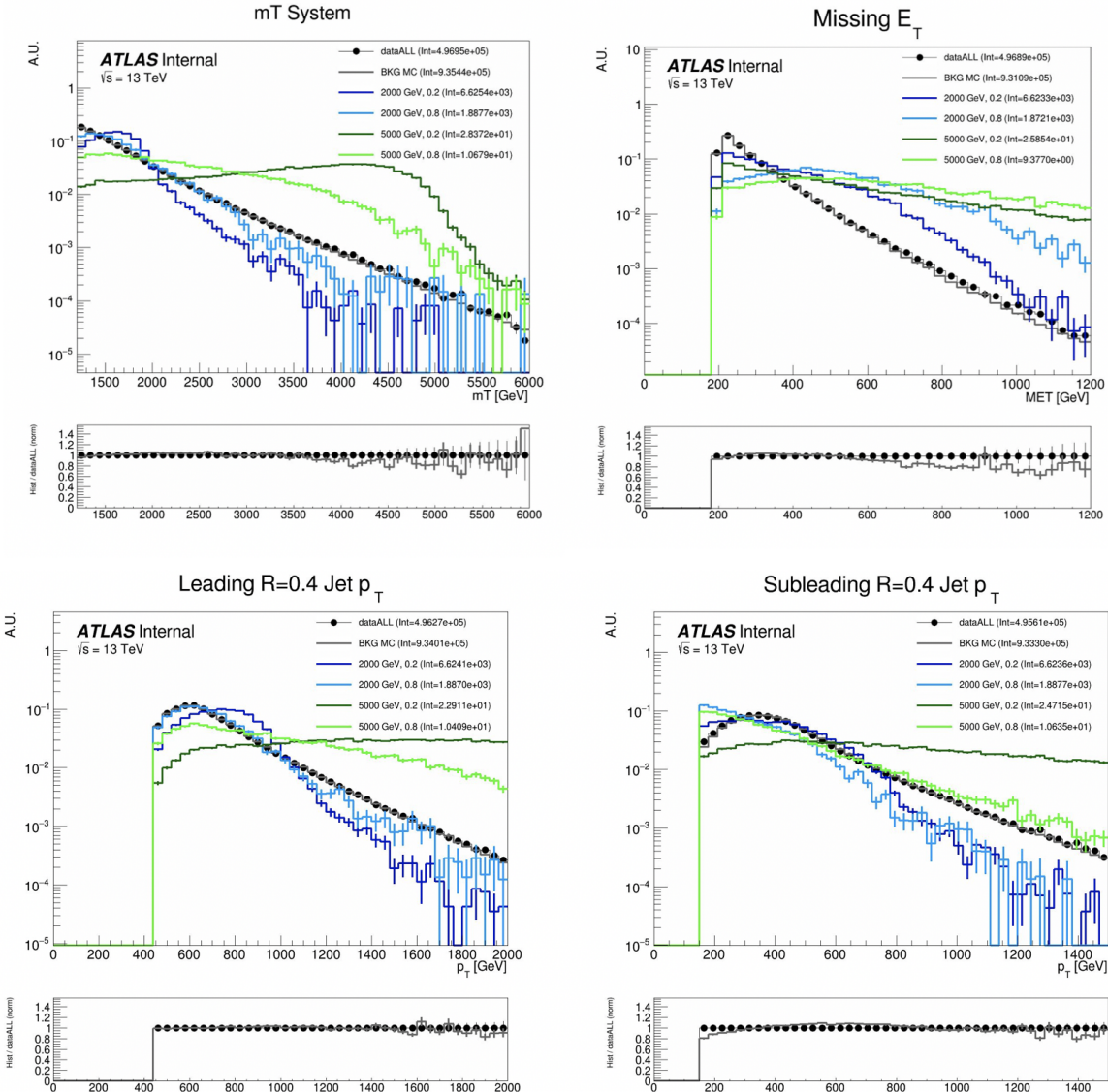


Figure 8.2: Energy and momentum analysis variables at preselection, for data, all background MC and representative signal models.  $m_T$  is the key fit variable, and this plot illustrates the smoothly falling background in comparison to the resonant shape of the signals.  $m_T$  is further illustrated in Figure 8.9.

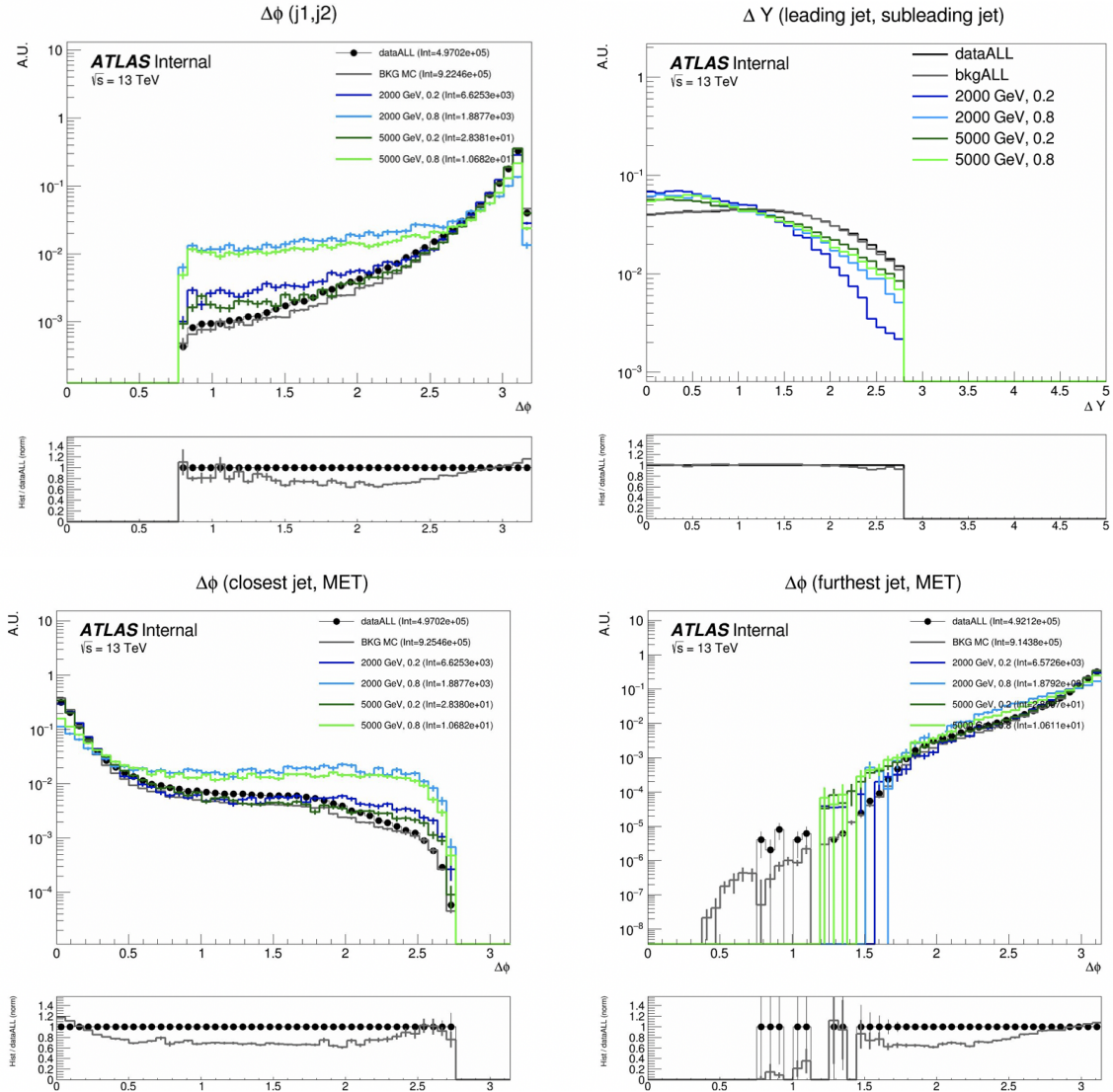


Figure 8.3: Orientation analysis variables at preselection, for data, all background MC and representative signal models. While  $\Delta\phi(E_T^{\text{miss}}, j)$  variables are not used explicitly in the analysis flow, they help create a picture of the event.

1598 the observed cross-section.

1599 In contrast, the Discovery analysis strategy attempts to design a more general search, which  
1600 could be sensitive to SVJs, but also to other possible hidden valley dark QCD models, such as  
1601 fully dark jets or emerging jets [21]. The Discovery analysis strategy uses the semi-supervised  
1602 ANTELOPE ML score in defining the signal region. Recall, the ANTELOPE is trained over AT-  
1603 LAS data only, with no explicit knowledge of the SVJ signal behavior. The Discovery fit strategy  
1604 is also signal model agnostic, by employing a bump hunt [**bumphunt**] strategy, which searches a  
1605 smoothly falling template for any bumps inconsistent with a background only hypothesis. There-  
1606 fore any signal which could present a resonant signature in  $m_T$  could show up as an excess in this  
1607 strategy.

1608 The details of both strategies will be explored in the follow sections which detail the design  
1609 of the signal regions and fit strategies. A diagram demonstrating the analysis flows can be seen in  
Figure 8.4. Details on each selection and region can be found in the following subsections.

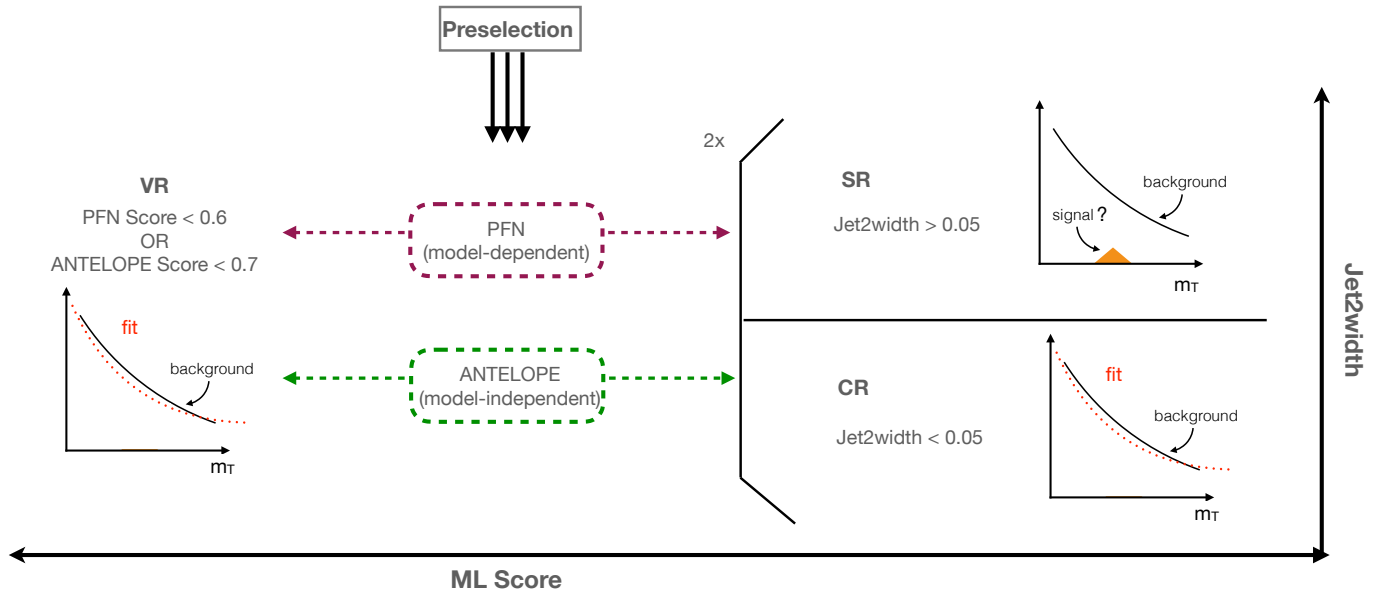


Figure 8.4: Flow of analysis selections, regions, and background estimation/validation fitting strat-  
egy.

1610

## 1611 8.3 Analysis Regions

### 1612 8.3.1 Control and Validation Regions

1613 The final background estimation will come from a polynomial fit to the  $m_T$  distribution in the  
 1614 signal region. The control and validation regions are needed to develop and test this fit in data.

1615 To define the CR selection, a variable is needed that isolates background from all signals across  
 1616 the  $(R_{inv}, m_Z)$  grid, which is challenging due to the varying nature of the signal models in quantities  
 1617 such as  $E_T^{\text{miss}}$  and  $p_T$  balance, as illustrated in Figure 8.2. The variable *jet width* is chosen, which  
 1618 is the calorimeter measurement of the width of a small-R jet as defined by the distance between the  
 1619 cluster and the jet axis scaled by the jet energy [**jetwidth**]. Figure 8.5 shows this variable specif-  
 1620 ically for the subleading jet width, both in data vs. MC at preselection, and for background vs.  
 1621 signals, indicating this broad discrimination power. The leading jet width, which was determined  
 1622 to be less useful for isolating signal from background is also shown. The subleading jet is more  
 1623 likely to be the jet aligned with MET, which is why the signal jet width is consistently wider in the  
 1624 subleading jet, but not the leading jet. A selection of **jet2width < 0.05** is chosen for the CR, with  
 1625 the VR and SR therefore having a selection of  $\text{jet2width} > 0.05$ . TODO: put diff jet2width plot  
 1626 here, remove from presel

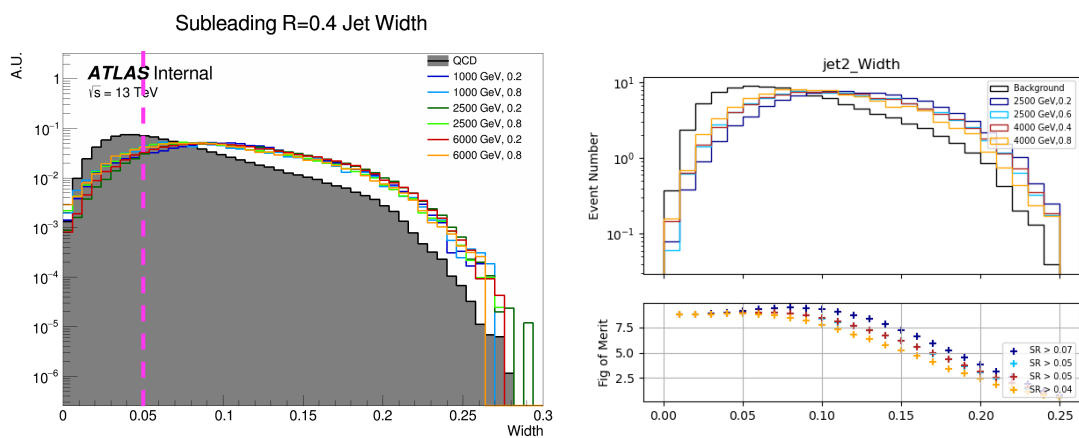


Figure 8.5: Distributions of the subleading jet width **jet2width** in data vs. background MC and signals at preselection (left) and background vs. representative signal models following the PFN score selection (right). Background MC comprises the samples listed in Appendix ???. Demonstrates that jet2width remains a discriminating variable after ML tool selection is made.

While the CR was used to develop the polynomial strategy, and is the primary region used in many of the fit studies, a validation region is used as an additional check of the estimation strategy in data. The VR is defined using the region of events with low ML score by either the PFN or ANTELOPE networks. Here the analysis strategy splits into the two parallel strategies presented in Section ??: the SVJ fit strategy and the dis A selection of `textbf{PFN}` score  $\leq 0.6$  & `jet2width`  $\geq 0.05$  defines the SVJ fit VR, while `textbf{ANTELOPE}` score  $\leq 0.7$  & `jet2width`  $\geq 0.05$  defines the discovery VR.

There are therefore three variables that are crucial to the analysis strategy: **jet2width, PFN/ANTELOPE score, and  $m_T$** . Figure 8.6 shows the correlations of all three variables to one another. Any outstanding correlations are shown in Figure 8.7 to not sculpt the  $m_T$  distribution and only affect its slope, making these variables trustworthy for extrapolation across background/signal regions and final fitting procedures.

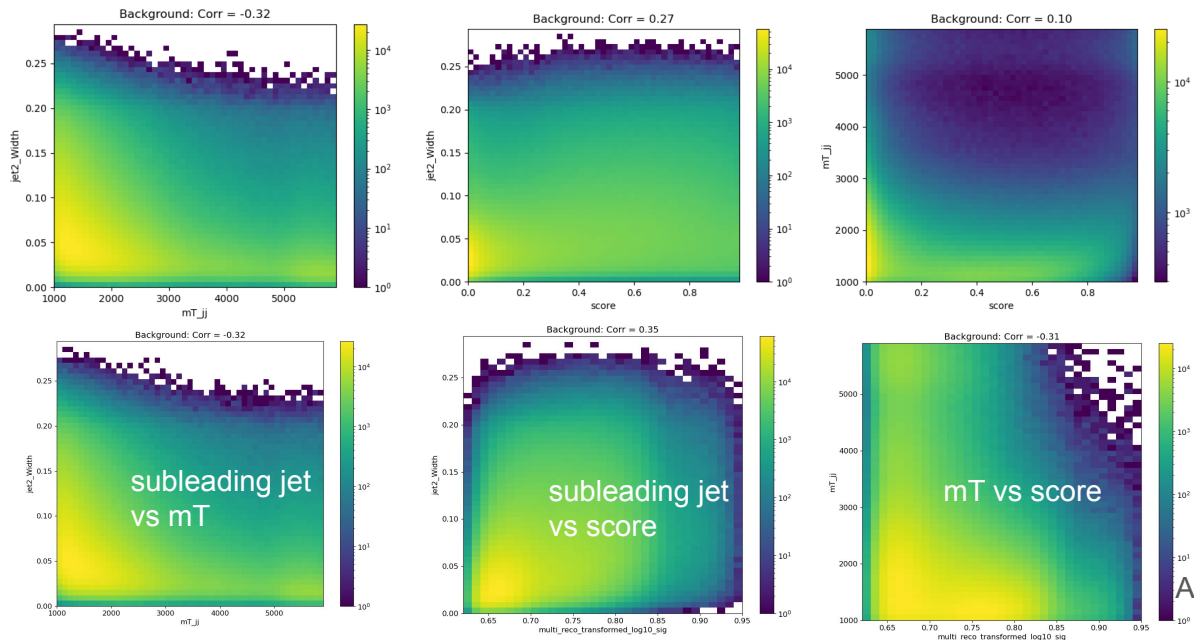


Figure 8.6: 2D plots revealing correlations between `jet2width` and  $m_T$  (left), `jet2width` and ML score (middle), and  $m_T$  with ML score (right). For the top row, the ML score is the PFN score, and for the bottom three, the ML score is the ANTELOPE score. Minimal correlations are observed and are shown to not sculpt  $m_T$ , validating these variables for analysis region construction and statistical treatment.

1638

The most important variable for shape robustness across the CR, VR, and SR is  $m_T$ , as this is the

variable that is fit for the statistical results. Figure 8.7 shows the distribution of  $m_T$  across the CR, VR, and SR, for both the PFN (supervised) and ANTELOPE (semi-supervised) strategies. Some slope is observed in the ratio of the CR to the VR/SR shapes; however, the chosen background estimation strategy of polynomial fitting is expected to accommodate this slope. Further, the ability of the background polynomial to fit both tail shapes will flex the fit framework in a way that will generate higher confidence in the final ability to fit the SR. No significant bumps or sculpting are observed.

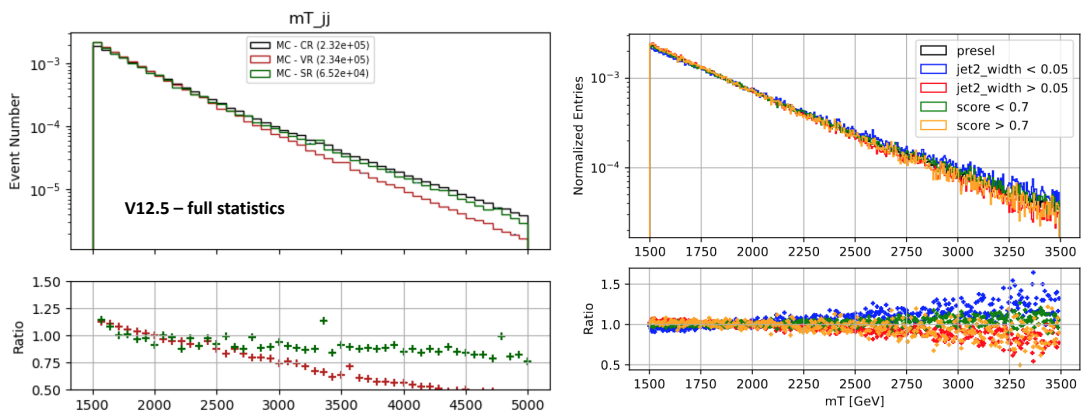


Figure 8.7:  $m_T$  in simulation across the CR, VR, and SR for both PFN (left) and ANTELOPE (right) selections.

Plots of the  $\phi$  shape variables in the CR and VR, and correlations of these variables with ML score are available in Appendix B.4.

### 8.3.2 Signal Region

A selection of **PFN score > 0.6 (ANTELOPE score > 0.7)** is made to provide the primary signal-to-background enrichment, as motivated by Section 7.1.1. Subsequently, the selection of **jet2width > 0.05** is made to enrich signal across the  $(R_{inv}, m_Z)$  grid and orthogonalize the SR to the CR. Note that the PFN and ANTELOPE regions are not orthogonal; this is because the two analysis flows serve different purposes, their statistical treatments are different, and they will not be combined.

A summary of the SR, CR, and VR definitions can be seen in Figure 8.8, along with the relative

data statistics in each region.

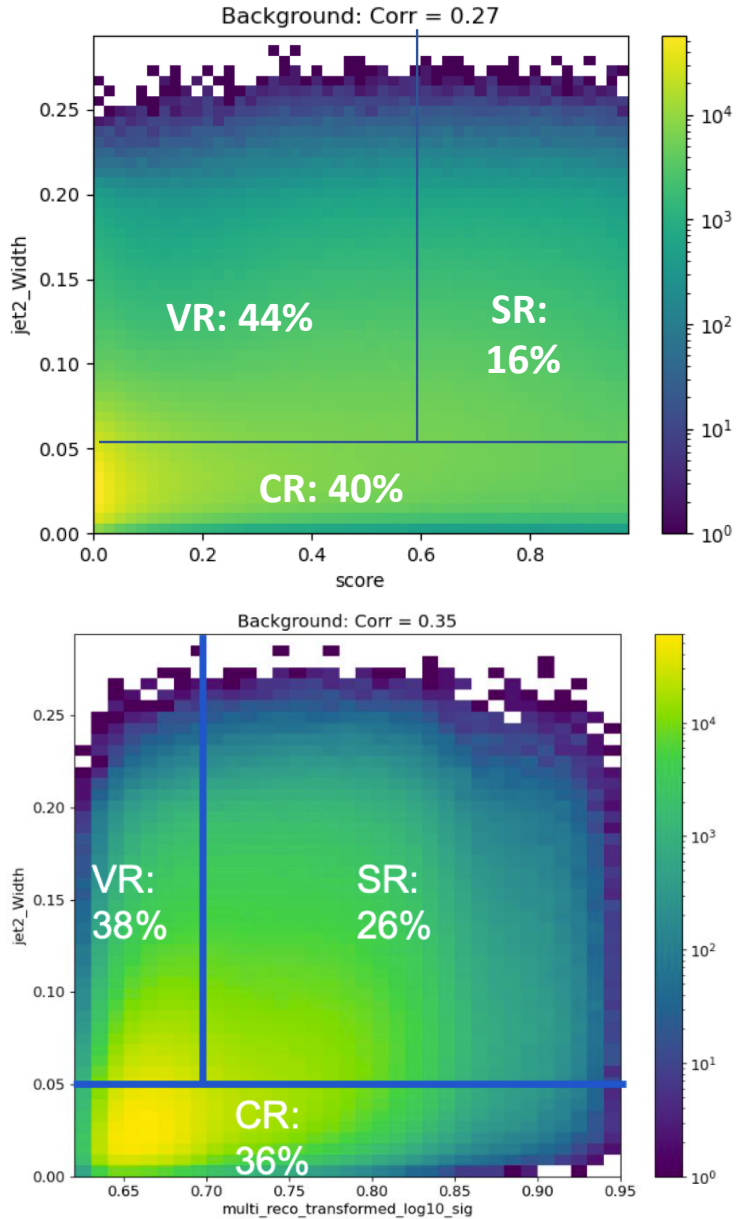


Figure 8.8: Definition of CR, VR, and SR regions using JET2WIDTH and the PFN score, along with the population of each region in data statistics for the PFN (top) and ANTELOPE (bottom) analyses.

1657

1658 **8.4 Background Estimation**

1659 The transverse mass  $m_T$  is chosen as the search variable due to the potential for the SVJ signal  
1660 to create a resonant shape around the mass of the  $Z'$ .  $m_T$  is the total transverse mass of the two

1661 leading jets and the  $E_T^{\text{miss}}$ , expressed in Equation 8.1 as:

$$m_T^2 = [E_{T,jj} + E_T^{\text{miss}}]^2 - [\vec{p}_{T,jj} + \vec{p}_T^{\text{miss}}]^2 \quad (8.1)$$

1662 where  $E_{T,jj}$  is the transverse energy of the dijet system. We take  $E_{T,jj} = m_{jj}^2 + |\vec{p}_{T,jj}|^2$ , where  
 1663  $m_{jj}^2$  is the invariant mass of the two leading jets, and  $\text{vec } p_{T,jj}$  is the vector sum of the  $p_T$  of the two  
 1664 leading jets.  $m_T$  is selected as the search variable in place of simpler invariant mass  $m_{jj}$  because  
 1665 substantial energy from the  $Z'$  decay is captured in the  $E_T^{\text{miss}}$ . Therefore incorporating  $E_T^{\text{miss}}$  into  
 1666  $m_T$  improves the resonance around the mass of the  $Z'$ .

Figure 8.9 illustrates the resonance in  $m_T$  of the SVJ signals.

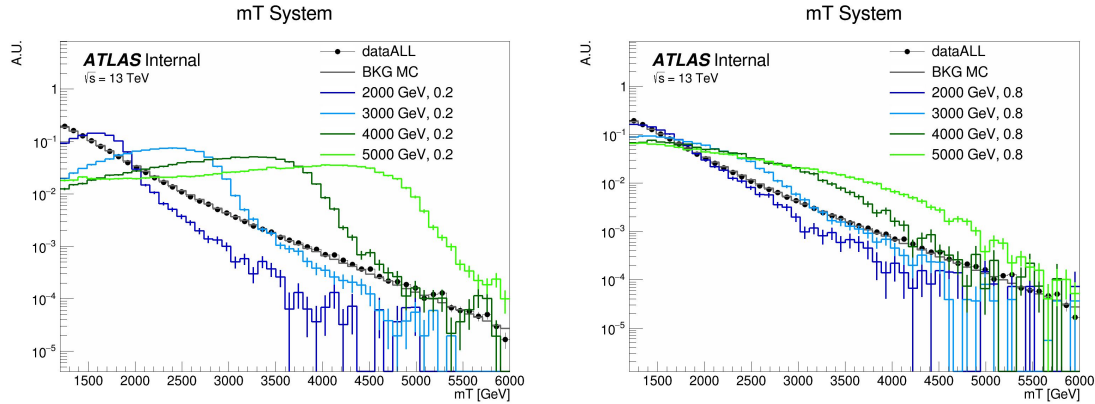


Figure 8.9: The resonant shape of the SVJ signals in  $m_T$ , in contrast to the smoothly falling  $m_T$  background. The high  $R_{inv}$  signals (right) boast a wider shape, making them more difficult to detect, while the low  $R_{inv}$  signals(left) produce a more narrow resonance in  $m_T$ .

1667

1668 The SM background in the SR is predominantly composed of QCD events, and due to the poor  
 1669 modeling of QCD at high energies by MC, it is estimated in a fully data-driven way. An empirical  
 1670 functional form is used for the background shape of  $m_T$ . The ability of this function to model  
 1671 the background behavior is tested both the CR and the VR for each analysis strategy. The shape  
 1672 parameters are left free in all the fits.

1673 The fits are performed for  $1500 \text{ GeV} < m_T < 6000 \text{ GeV}$ . The polynomial chosen is a standard  
 1674 5-parameter function used in several similar dijet search analyses such as [72] [73] [74] and shown

1675 in Equation 8.2:

$$f(x) = p_1(1 - x)^{p_2}x^{p_3+p_4\ln x+p_5\ln^2 x} \quad (8.2)$$

1676 Here  $x = m_{jj}/\sqrt{s}$  and the  $p_i$  are free parameters. The fit function is required to be fully positive, and  
1677 the  $m_T$  distribution is fit to 90 even-width bins. The resulting fit shape is used as the background  
1678 estimation for both the SVJ Fit strategy and the Discovery strategy. Validation of the fit and its  
1679 ability to both model the background and detect signal are shown in Section 8.5. Higher order  
1680 polynomials were also considered, but an F-test was performed and the five parameter function  
1681 was determined to be adequate and optimal for capturing the shape of the background.

1682 **8.5 Fit Strategy and Validation**

1683 **8.5.1 SVJ Fit Strategy**

1684 **Background Only Fits**

1685 Three validations are used for the background fit polynomial: MC across all analysis regions,  
1686 data in the CR and VR, and pseudo-data in the CR and VR.

1687 Figure 8.10 shows the post-fit values of the fit parameters and their uncertainties for the exclusion  
1688 (PFN-based) CR and VR.

Parameter	CR		VR	
	Value	Error	Value	Error
$N_{bkg}$	5.3097E+04	3.35E+02	5.3064E+04	3.33E+02
p2	1.7800E+01	7.92E-01	1.7244E+01	9.73E-01
p3	1.3883E+01	3.90E-01	1.3234E+01	4.40E-01
p4	7.3108E+01	1.07E-01	7.9501E+01	1.17E-01
p5	1.1808E+00	3.19E-02	1.4061E+00	3.48E-02

Figure 8.10: Post-fit parameters for the PFN CR and VR.

1688

1689 Figure 8.11 shows the ability of this polynomial to fit the smoothly falling  $m_T$  background in

1690 simulation across all 3 analysis regions (CR, VR, SR). The  $m_T$  spectrum is fit in 90 even bins.  
 1691 These distributions are obtained by downsampling the MC statistics to match the relevant statis-  
 1692 tics of the data region, in accordance with the MC weights. The high background-only  $p$ -value  
 indicates a good fit.

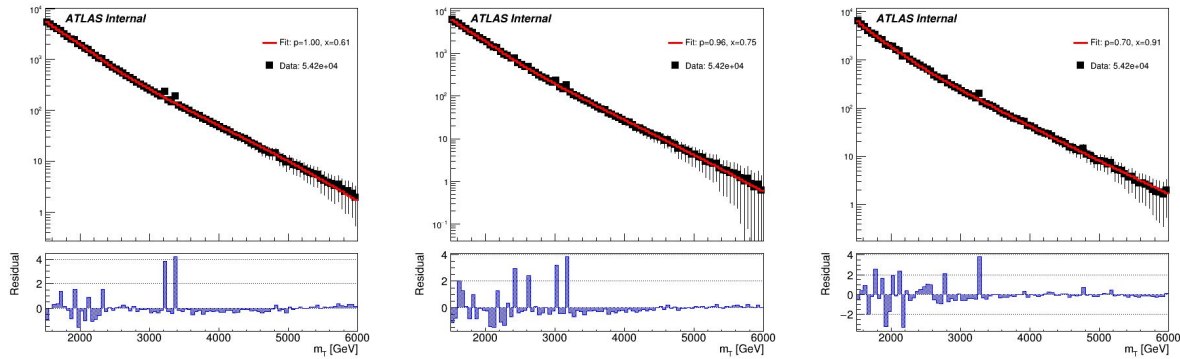


Figure 8.11: Background-only  $m_T$  fits using representative MC in the CR (left), VR (middle), and SR (right).

1693  
 1694 After verifying the background modeling in all analysis regions in simulation, it is tested in  
 1695 two data regions, the CR (low jet2width) and the VR (low ML score) which are orthogonal to the  
 1696 blinded SR. Each  $m_T$  histogram fit is obtained from randomly downsampling the original statistics  
 1697 in the CR/VR until a *statistically identical* sample is obtained. Three downsampled histograms are  
 1698 provided for each region, each with a random selection of events to match the expected SR event  
 1699 yields. Figure 8.12 shows both of these regions, with high background only  $p$ -values indicating  
 1700 good compatibility. For closure, Figure 8.13 shows the same fit performed to the full statistics CR  
 1701 and VR regions.

1702 To further validate the fit in more instances, pseudo-data is created from the CR/VR data dis-  
 1703 tributions. It is created following the Asimov prescription with smoothing to accommodate fluctu-  
 1704 ations in the high  $m_T$  tail. The smoothing applied follows the procedure for functional decomposi-  
 1705 tion described in Ref. [edgar2018functional]. Figure 8.14 shows the impact of smoothing on the  
 1706 source data distribution in the CR. Toys are then thrown from the smoothed distribution.

1707 Figure 8.15 shows the resulting  $p$ -values after an ensemble of 100 fits to varying pseudo-data  
 1708 distributions sourced from the data CR. A flat distribution is observed, indicating good statistical

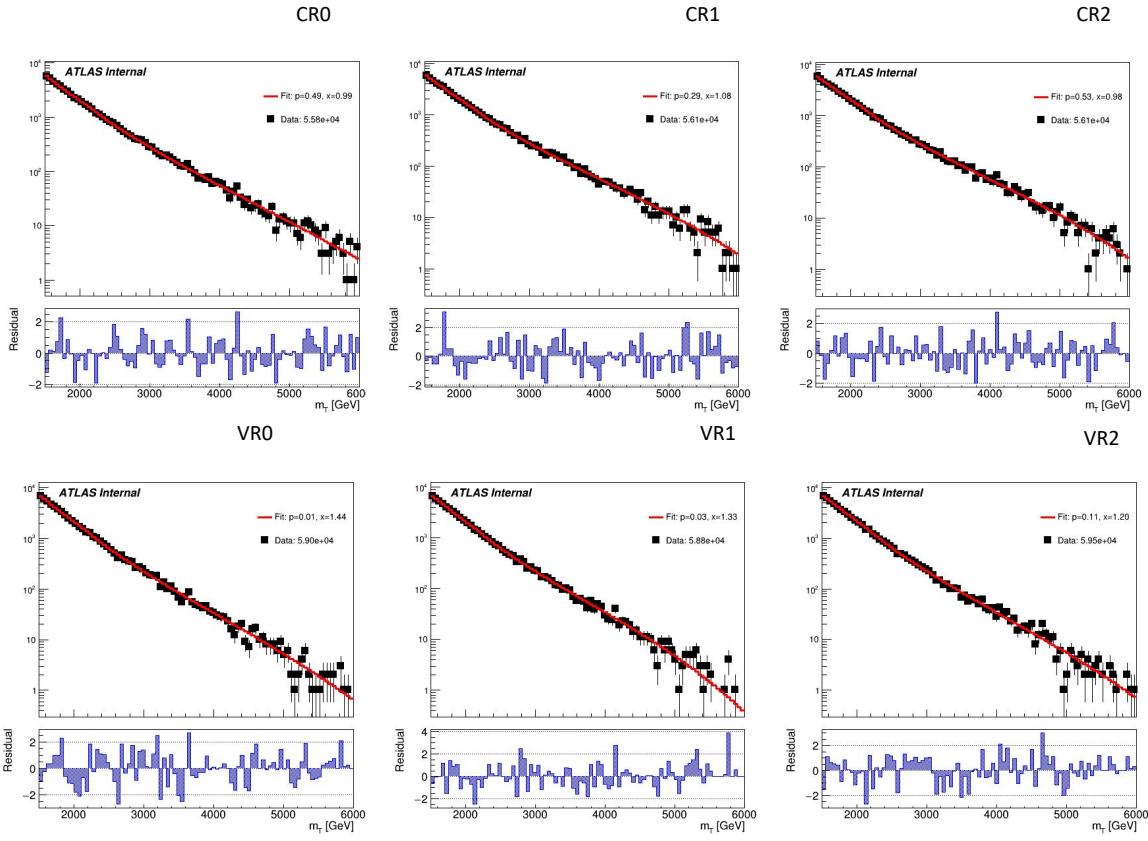


Figure 8.12: Background-only  $m_T$  fits using data in orthogonal but statistically identical samples to the SR, obtained by downsampling the CR/VR statistics, for the CR (top) and VR (bottom).

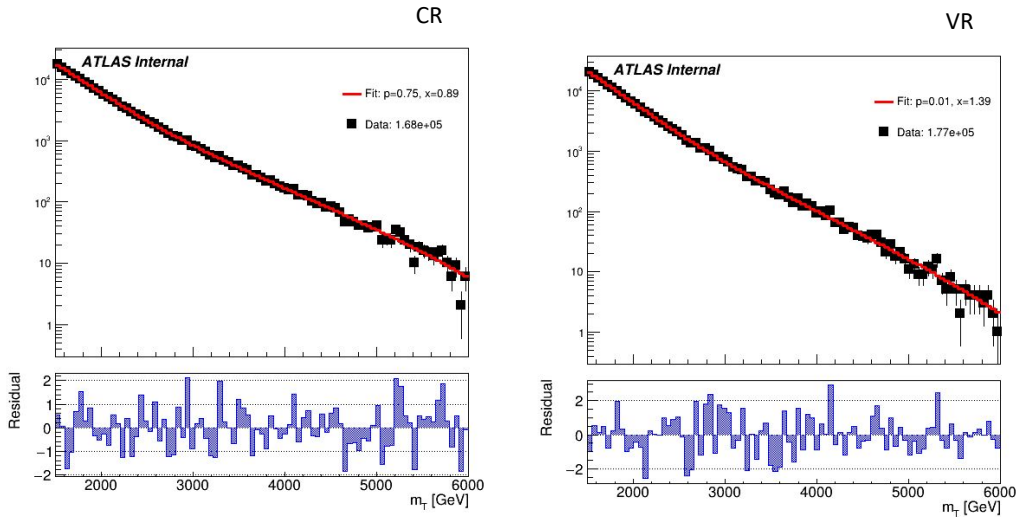


Figure 8.13: Background-only  $m_T$  fits using data in the full statistics CR and VR regions.

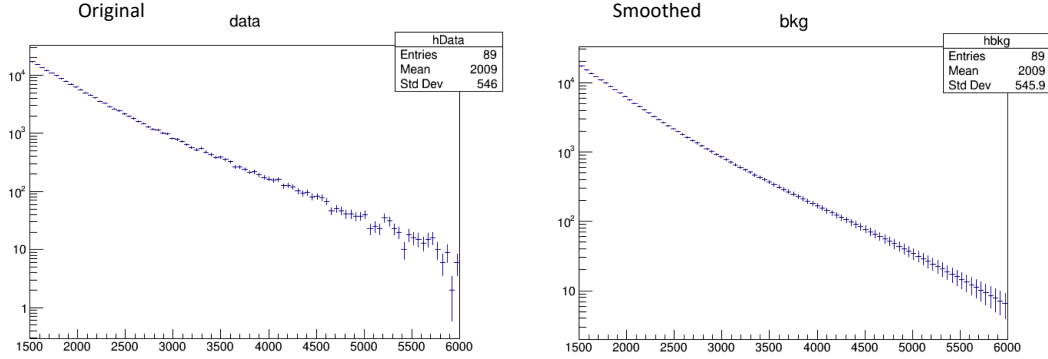


Figure 8.14:  $m_T$  distribution in the data CR, before (left) and after (right) smoothing.

behavior.

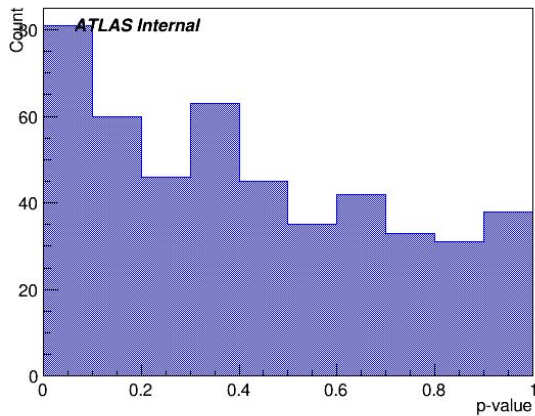


Figure 8.15:  $p$ -value histograms from 500 fits to Asimov data in the CR.

1709

## 1710 Signal + Background Fits

1711 Figure 8.16 shows some examples of S+B fits on the background-only distribution for a variety  
 1712 of signal hypotheses across the ( $R_{inv}$ , mass) grid.

1713 **Spurious Signal** The spurious signal fits are done using S+B fits on signal-depleted regions.  
 1714 These fits performed in pseudodata derived from a smoothed CR template are used to calculate the  
 1715 spurious signal uncertainty, as described in Section ??.

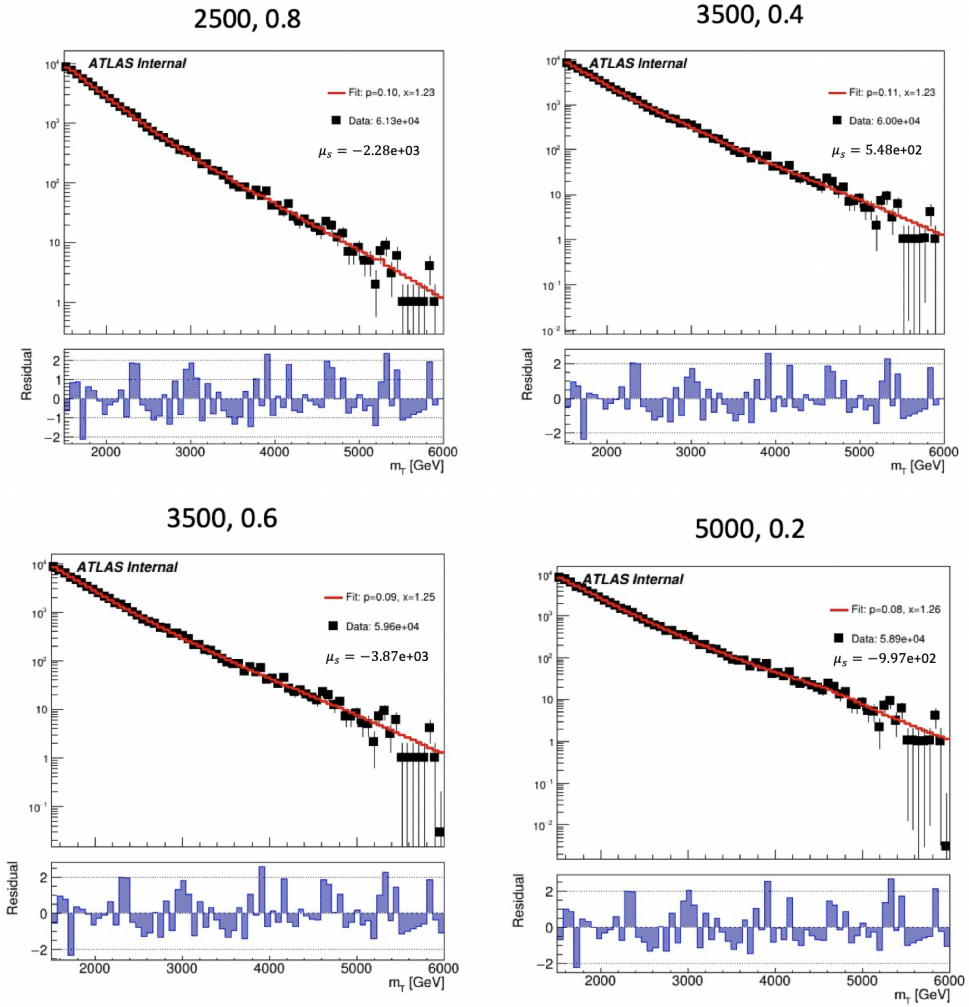


Figure 8.16: Example S+B fits on background only spectrum (without systematics) for a variety of signal points.

1716 **Signal Injection in CR Template** Figure 8.17 shows an example of an injected signal into the  
 1717 exclusion region  $m_T$  spectrum, and the ability of the fit framework to accurately fit the number of  
 signal events.

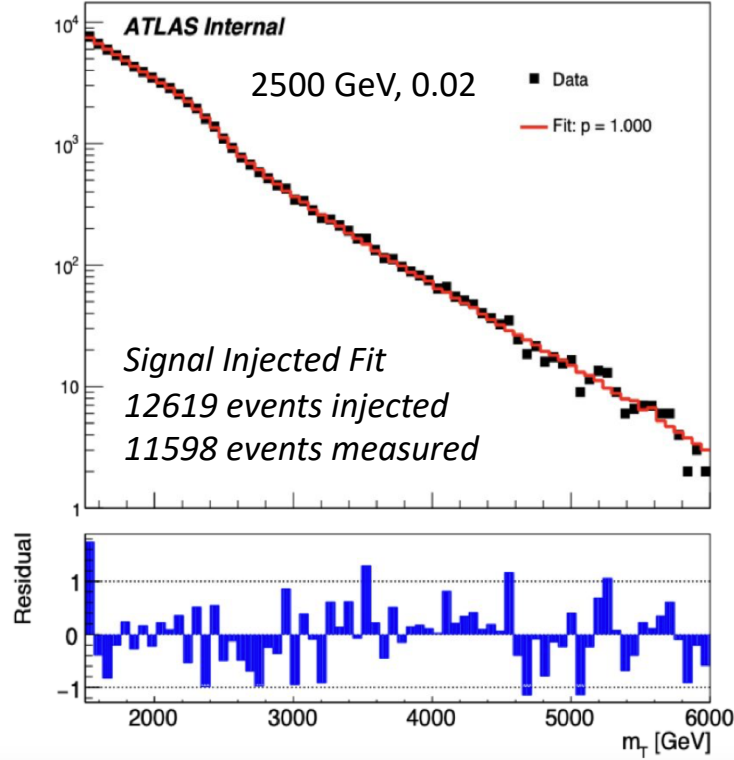


Figure 8.17: Example S+B fits on a background  $m_T$  spectrum with injected signal from the point (2500 GeV,  $R_{inv}=0.2$ ).

1718  
 1719 Figure 8.18 shows the linearity of the fitted signal as a function of the size of the injected signal,  
 1720 for all 4  $R_{inv}$  categories and several  $Z'$  masses. No uncertainties on the signal model are included.  
 1721 These fits are done in a single template of the CR, making the fitted signal prone to fluctuations in  
 1722 the underlying template, motivating the use of toys to better capture the behavior of the S+B fit in  
 1723 finding a signal.

1724 **Signal Injection in Asimov Data** To better understand the correlations of fit errors in the above  
 1725 single-template injection test and avoid drawing conclusions from a single scenario, signal in-  
 1726 jection tests using Asimov data will be performed before unblinding. Criteria for this check are

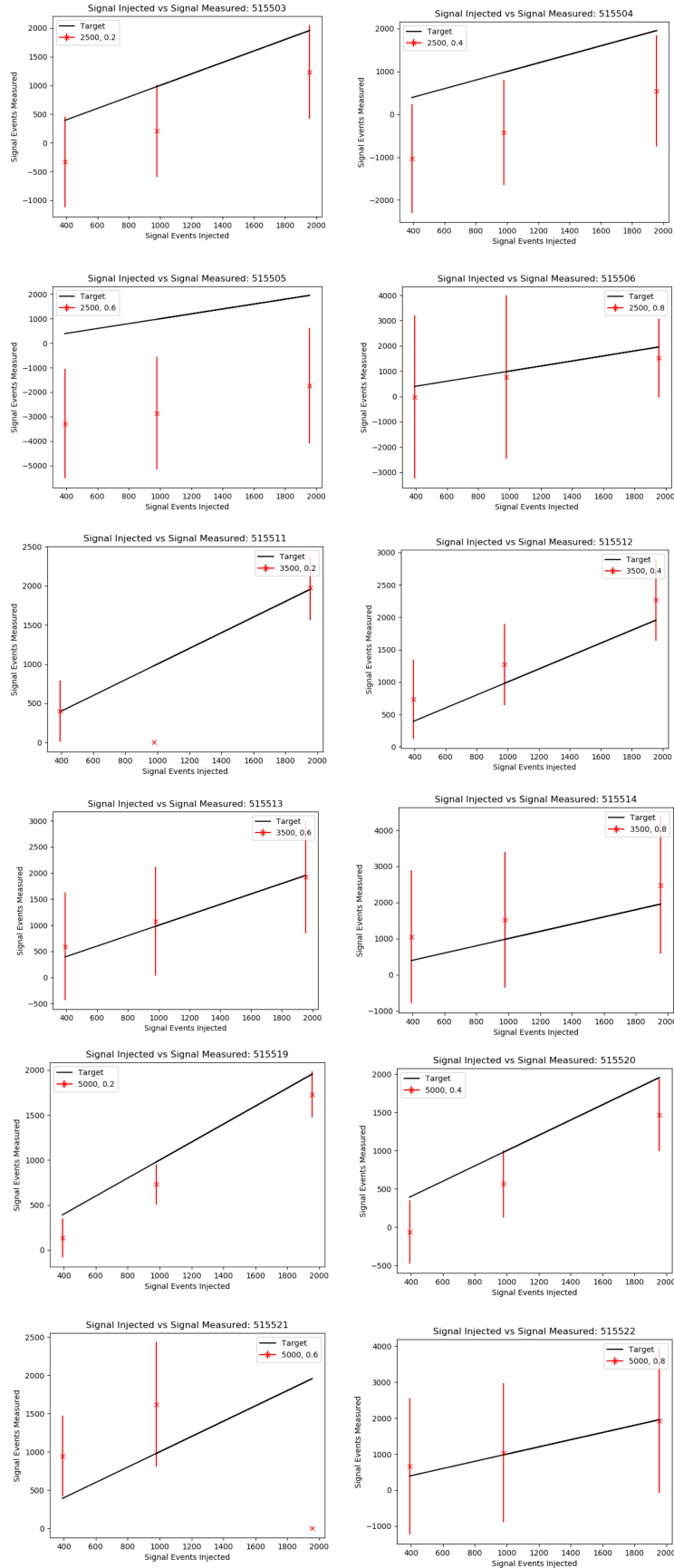


Figure 8.18: Linearity of fitted vs. injected signal across  $m_T$ , for signal points with  $R_{inv}=0.2, 0.4, 0.6$ , and  $0.8$ , with several  $Z'$  masses (2500 GeV, 3500 GeV, and 5000 GeV top to bottom) for a single CR template with no systematics.

adapted from the Run 2 dijet TLA analysis <sup>1</sup>. 50 Asimov trials are run for representative signal points across  $Z'$  mass and  $R_{inv}$ . Specifically, we will take the difference between fitted and injected signal events as a spurious signal and require it to be less than 10% of the original injected signal yield, or its absolute value to be less than 50% of the fitted signal RMS:

$$S_{\text{spur}} = S_{\text{fit}} - S_{\text{inj}} < 0.1S_{\text{inj}} \text{ OR } < 0.5\sigma_{\text{fit}} \quad (8.3)$$

Figure 8.19 provides tabular results of these tests, assessing both  $S_{\text{spur}}$  from Equation 8.3. Figure 8.20 displays the measured  $S_{\text{spur}}/\sigma_{\text{fit}}$  for each signal point to assess the criterion from Equation 8.3. We find that all but 1 of the tested signal points and signal injection sizes ( $m_{Z'} = 4000$  GeV,  $R_{inv}=0.2$  at  $5\sigma$  significance) pass the criteria in Equation 8.3. While ( $m_{Z'} = 4000$  GeV,  $R_{inv}=0.2$ ) generally gives the highest  $S_{\text{spur}}$  of all points, the one injected size that violates the test criterion is close to 0.5 and within a trend shared by all points.

---

<sup>1</sup><https://cds.cern.ch/record/2632454>, Section 10.4

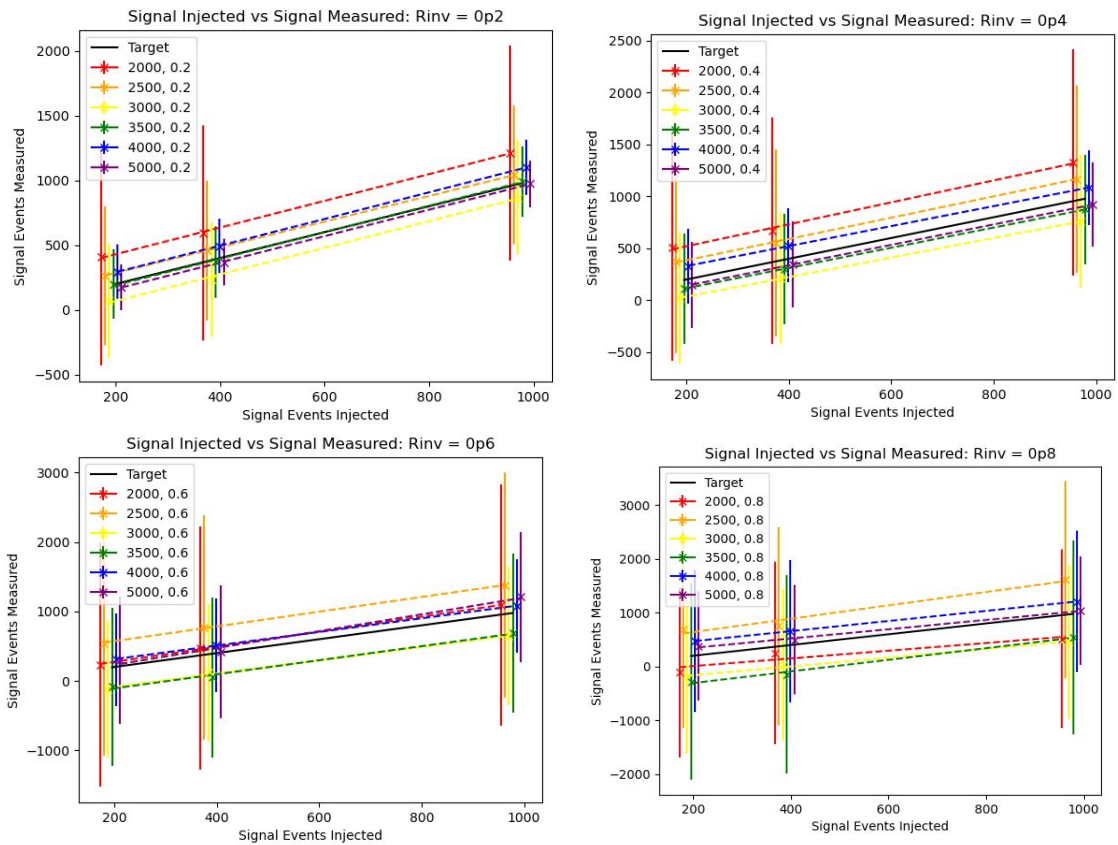


Figure 8.19: Spurious signal at a variety of injected values (1, 2, and  $5\sigma$  significant), for all signal points in the grid,  $R_{inv}=0.2$  (top left), 0.4 (top right), 0.6 (bottom left), and 0.8 (bottom right). i

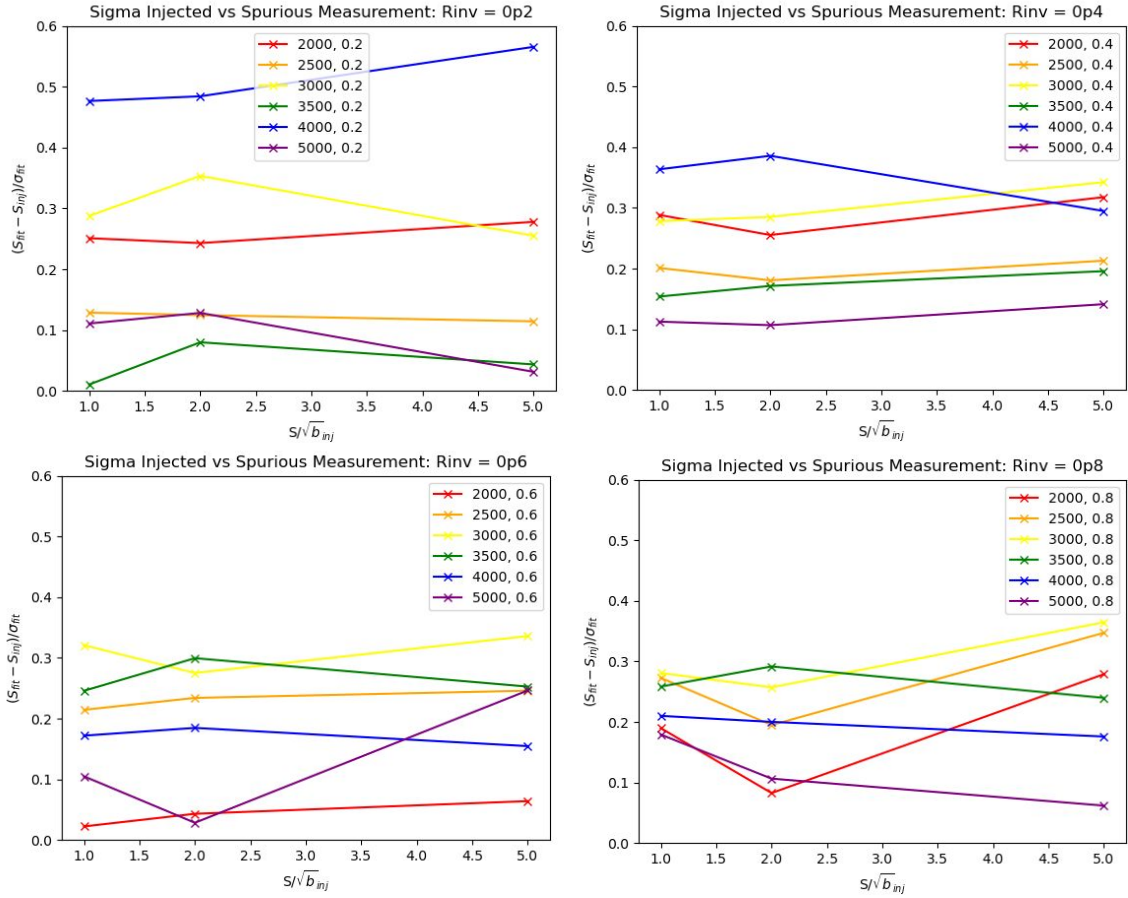


Figure 8.20:  $S_{\text{spur}}/\sigma_{\text{fit}}$  at a variety of injected values (1, 2, and 5 $\sigma$  significant), for all signal points in the grid,  $R_{\text{inv}}=0.2$  (top left), 0.4 (top right), 0.6 (bottom left), and 0.8 (bottom right). i

## 1737 Expected Sensitivity

1738 Limits are obtained by determining the cross section of the signal that can be excluded to 95%  
1739 confidence. Figure 8.21 shows the expected limits obtained from S+B fits to statistically identical  
1740  $m_T$  spectra from the CR region (which is closest in  $m_T$  shape to the SR according to MC studies).

1741 Considerable exclusion power is predicted for low  $R_{inv}$  signal points, with the higher  $R_{inv}$  points  
1742 presenting more difficulty due to the very broad signal bump. A similar trend is observed in the  
1743 CMS s-channel search [[cms\\_schan](#)].

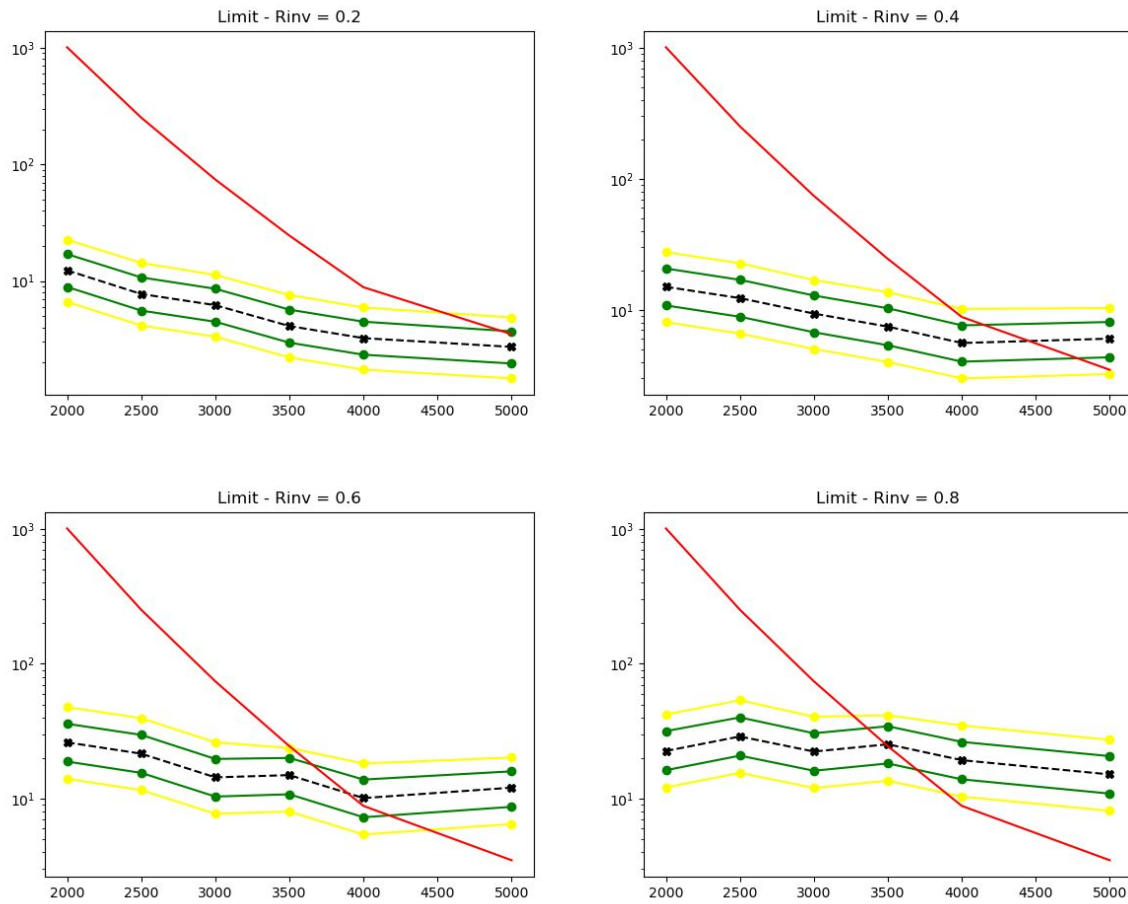


Figure 8.21: 95% C.L. upper limits for signal models across  $Z'$  mass, for four different  $R_{inv}$  fractions, from the CR region (without systematics).

1744 A 2D limit presentation is also being considered, in the  $(R_{inv}, \text{mass})$  plane.

1745 8.5.2 Discovery Strategy)

1746 Model-independent fits for the discovery region will be performed using pyBumpHunter. The  
1747 strategy will consist of comparing the data in a given  $m_T$  spectrum of interest to a background  
1748 estimation derived by performing the polynomial fit and sampling from the post-fit function into  
1749 a histogram. The polynomial fit is done to an  $m_T$  distribution with 180 bins (25 GeV wide). To  
1750 keep the trials factor moderate, a rebinning will be performed based on the signal mass resolution in  
1751  $m_T$ (Section 8.5.2) to best assess the significance of BumpHunter results. This is under development  
1752 with preliminary studies shown in Appendix ??.

1753 Figure 8.22 shows the post-fit values of the fit parameters and their uncertainties for the discov-  
1754 ery (ANTELOPE-based) CR and VR. Figure 8.23 shows the resulting functions and residuals with  
1755 respect to the CR and VR data. These results indicate good ability of the 5-parameter polynomial  
to also model the ANTELOPE selected region.

Parameter	CR		VR	
	Value	Error	Value	Error
$N_{bkg}$	8.8299E+04	4.27E+02	8.8312E+04	4.27E+02
p2	3.6804E+01	3.97E+00	3.8490E+01	4.29E+00
p3	4.2925E+01	5.06E+00	4.3432E+01	4.81E+00
p4	1.9080E+01	1.95E+00	1.9626E+01	1.78E+00
p5	2.9298E+00	2.86E-01	3.0527E+00	2.62E-01

Figure 8.22: Post-fit parameters for the ANTELOPE CR and VR.

1756

1757 **Signal Mass Resolution  $m_T$  Binning**

1758 In the discovery region, a binning for  $m_T$  is determined that is based on the expected signal  
1759 width. This is done to improved the BumpHunter performance. The signal mass resolution for a  
1760 given point is determined with a double-sided Crystal Ball fit to the mass. These fits are performed  
1761 across Z' mass, and a linear fit to these values is performed to determine the optimal bin width

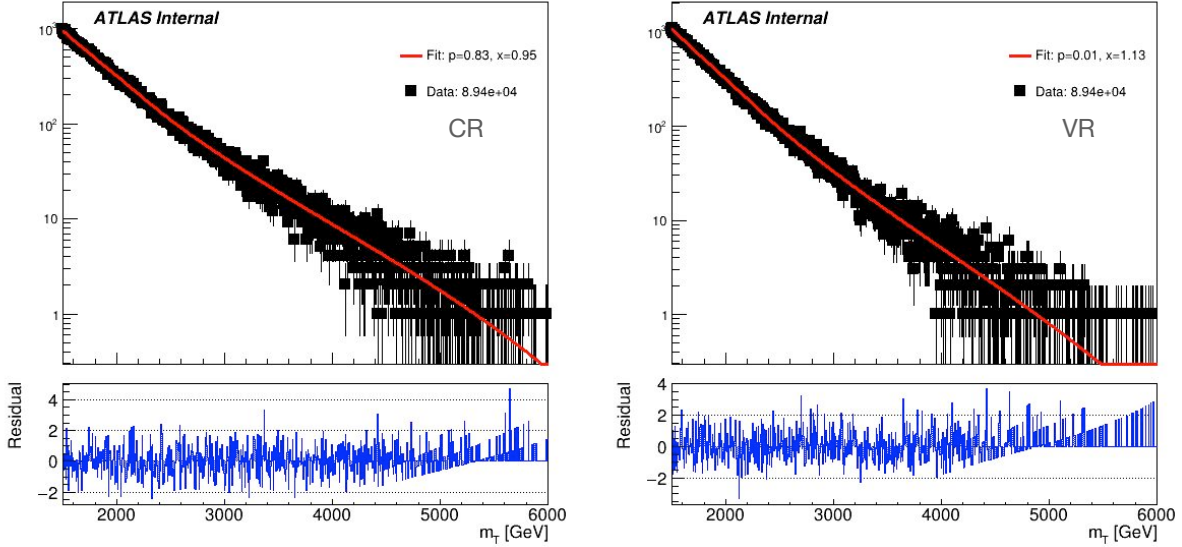


Figure 8.23: Post-fit function and residuals for the ANTELOPE CR and VR.

1762 across  $m_T$ .

1763 The x-axis value used is a data-driven way to determine the appropriate value of  $m_T$  for a  
 1764 given signal, given that the considerable  $E_T^{\text{miss}}$  from the dark particles means that the truth Z'  
 1765 mass does not well approximate the peak  $m_T$  value. As the  $E_T^{\text{miss}}$  in the final state means that the  
 1766  $m_T$  is always an underestimate of the Z' mass, the truth Z' mass can be used as an upper bound. An  
 1767 integral is then performed backwards from that value until 60% of the total signal yield is included.  
 1768 This window is referred to as the 60% mass window; the mean of this window then provides an  
 1769 approximate localization of the signal mass peak in  $m_T$ . Figure 8.24 shows some examples of this  
 1770 algorithm on several signal points of varying  $R_{\text{inv}}$  and mass.

1771 Figure 8.25 shows the result of this linear fit for the four  $R_{\text{inv}}$  values considered in the signal  
 1772 grid. As expected, the resolution is considerably different for low and high  $R_{\text{inv}}$  points.

1773 A single  $m_T$  binning for the final SR plotting and BumpHunting is determined by selecting a  
 1774 harmonized binning at low  $m_T$ , and moving to wider bins at high  $m_T$ . As for higher  $R_{\text{inv}}$  signal  
 1775 points the mass resolution linear fit gives negative results, we require each bin to have a width of  
 1776 at least 100 GeV. Figure 8.26 shows the resulting bins for each  $R_{\text{inv}}$  category that comes from the  
 1777 mass resolution fits, with the addition of the minimum 100 GeV bin width requirement.

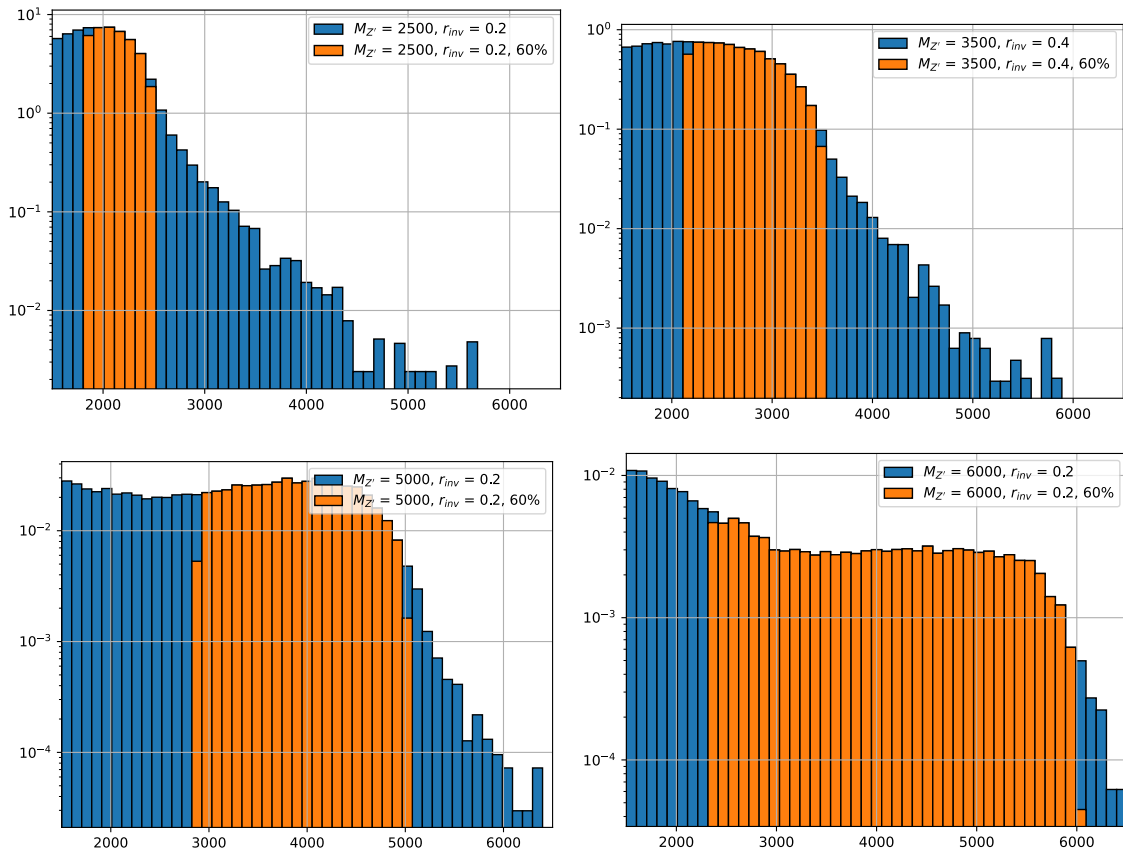


Figure 8.24: Example determinations of the 60% mass window means for several signal points.

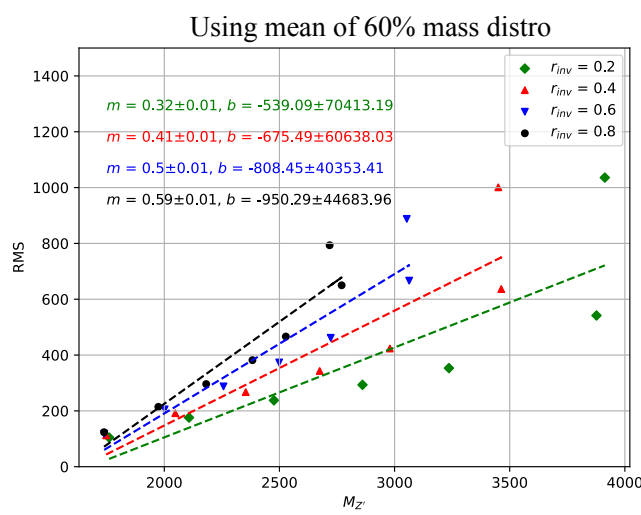


Figure 8.25: Signal mass resolution for  $m_T$  binning for the signal grid in  $(R_{inv}, \text{mass})$  space.

$r_{inv} = 0.2 \rightarrow$	[1500, 1600, 1700, 1800, 1904, 2029, 2177, 2356, 2569, 2824, 3128, 3493, 3929, 4451, 5075, 5822, 6715]
$r_{inv} = 0.4 \rightarrow$	[1500, 1600, 1700, 1800, 1910, 2053, 2238, 2477, 2787, 3187, 3704, 4374, 5240, 6361]
$r_{inv} = 0.6 \rightarrow$	[1500, 1600, 1700, 1800, 1919, 2087, 2321, 2650, 3110, 3755, 4659, 5925, 7698]
$r_{inv} = 0.8 \rightarrow$	[1500, 1600, 1700, 1800, 1927, 2117, 2400, 2823, 3455, 4400, 5811, 7918]

Figure 8.26:  $m_T$  bins based on the signal mass resolution and the minimum 100 GeV width requirement, for each  $R_{inv}$  signal category.

1778 In order to have a final  $m_T$  binning that is not highly model-dependent, we consolidate these  
 1779 four different bins into a single binning which is provided below:  
 1780 [1500, 1600, 1700, 1800, 1900, 2025, 2175, 2350, 2575, 2825, 3125, 3500, 3925, 4450, 5075,  
 1781 6000]  
 1782

## BumpHunter Fits

1783 Figure 8.27 shows the result of running BumpHunter over the CR and VR  $m_T$  spectra, binned  
 1784 according to the signal mass resolution binning described above. The background estimation here  
 1785 is derived by fitting the ANTELOPE regions with the polynomial fit function, and sampling from  
 1786 this function to create a binned histogram. We define a spurious signal as any BumpHunter fit find-  
 1787 ing an excess with p-value < 0.01 (taken from other dijet analysis eg. Ref. [ATLAS:2023azi]). No  
 1788 spurious signal is observed, and p-values indicate good agreement with the background estimation.  
 1789

1790 Figure 8.28 shows BumpHunter p-values over 100 Asimov trials. The same fit success criteria  
 1791 as the PFN region is applied: p-value > 0.001 and fit status succeeding (0 or 1). In both cases, no  
 1792 spurious signals are found (p-value < 0.01).

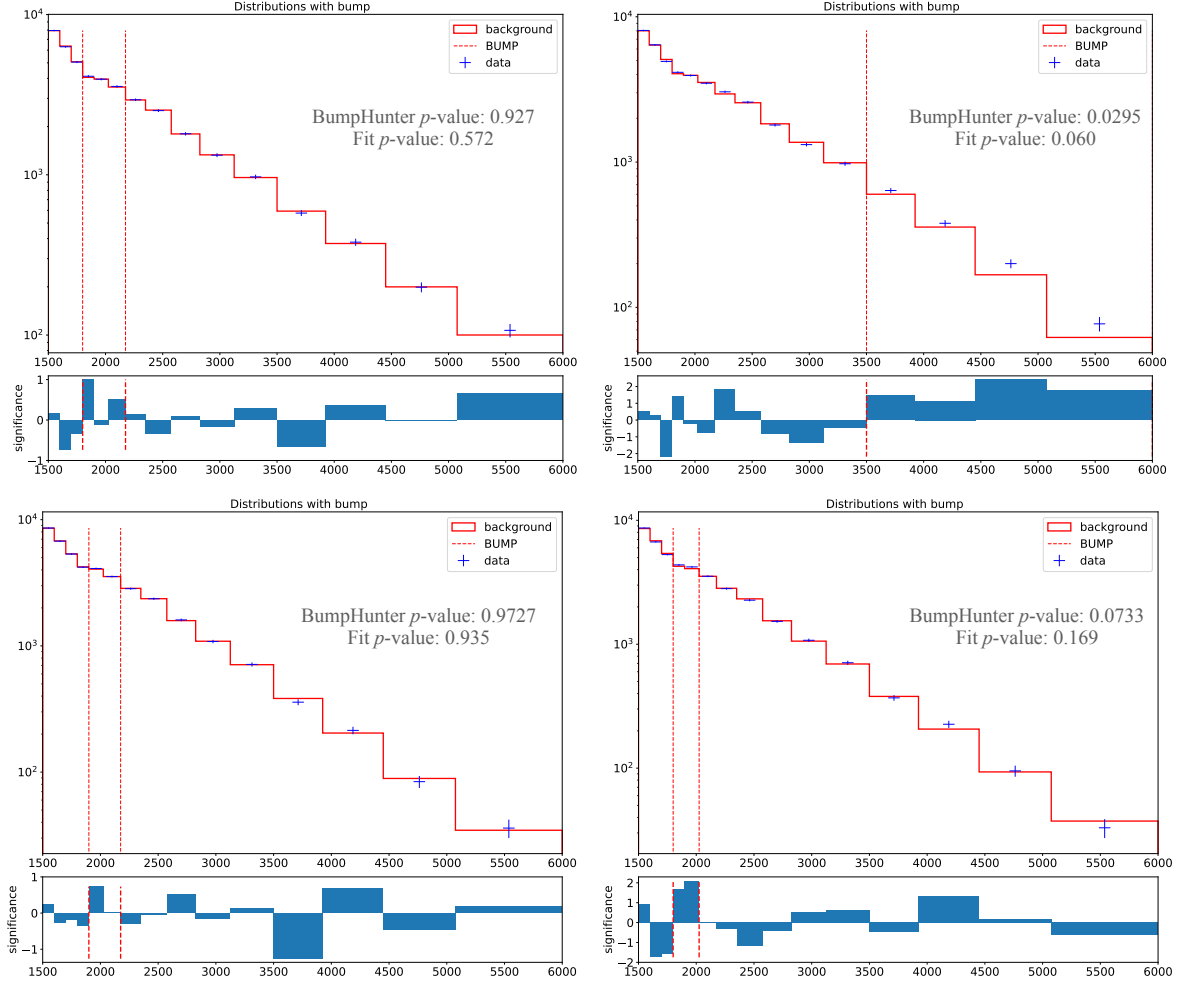


Figure 8.27: BumpHunter fits on the ANTELOPE  $m_T$  spectra for both the CR and VR. In a signal-depleted region, good agreement with the background estimation is observed.

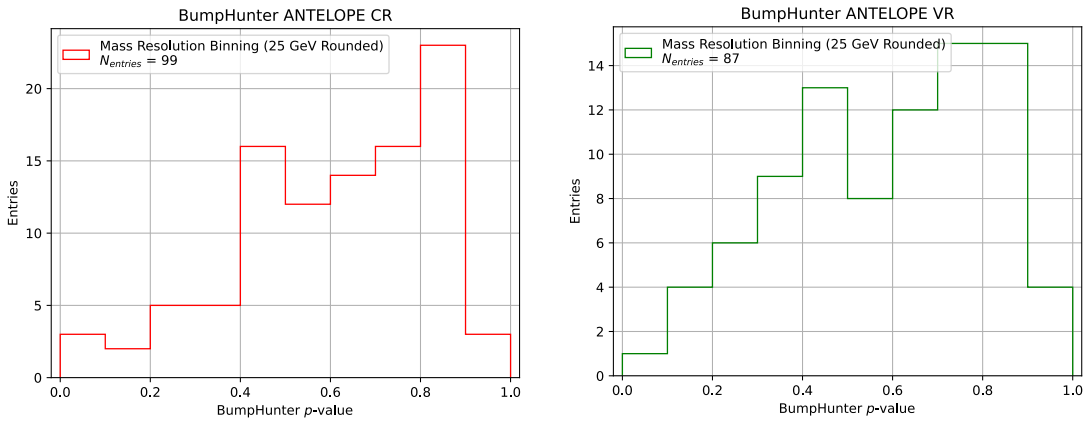


Figure 8.28: BumpHunter p-values extracted for 100 Asimov toys for both the ANTELOPE CR (top) and VR (bottom) showing the highest (left) and lowest (right) p-value fits. The number of events in the histogram deviates from 100 based on failed background-only fits.

1793

1794

## **Chapter 9: Results**

1795

## Conclusion or Epilogue

1796        Use this page for your epilogue or conclusion if applicable; please use only one of the titles  
1797      for this page. Otherwise, you may delete it. Use this page for your epilogue or conclusion if  
1798      applicable; please use only one of the titles for this page. Otherwise, you may delete it. Use this  
1799      page for your epilogue or conclusion if applicable; please use only one of the titles for this page.  
1800      Otherwise, you may delete it. Use this page for your epilogue or conclusion if applicable; please  
1801      use only one of the titles for this page. Otherwise, you may delete it. Use this page for your  
1802      epilogue or conclusion if applicable; please use only one of the titles for this page. Otherwise,  
1803      you may delete it. Use this page for your epilogue or conclusion if applicable; please use only one  
1804      of the titles for this page. Otherwise, you may delete it. Use this page for your epilogue or  
1805      conclusion if applicable; please use only one of the titles for this page. Otherwise, you may delete  
1806      it. Use this page for your epilogue or conclusion if applicable; please use only one of the titles for  
1807      this page. Otherwise, you may delete it. Use this page for your epilogue or conclusion if  
1808      applicable; please use only one of the titles for this page. Otherwise, you may delete it. Use this  
1809      page for your epilogue or conclusion if applicable; please use only one of the titles for this page.  
1810      Otherwise, you may delete it. Use this page for your epilogue or conclusion if applicable; please  
1811      use only one of the titles for this page. Otherwise, you may delete it. Use this page for your  
1812      epilogue or conclusion if applicable; please use only one of the titles for this page. Otherwise,  
1813      you may delete it. Use this page for your epilogue or conclusion if applicable; please use only one  
1814      of the titles for this page. Otherwise, you may delete it. Use this page for your epilogue or  
1815      conclusion if applicable; please use only one of the titles for this page. Otherwise, you may delete

1816 it. Use this page for your epilogue or conclusion if applicable; please use only one of the titles for  
1817 this page. Otherwise, you may delete it. Use this page for your epilogue or conclusion if  
1818 applicable; please use only one of the titles for this page. Otherwise, you may delete it. Use this  
1819 page for your epilogue or conclusion if applicable; please use only one of the titles for this page.  
1820 Otherwise, you may delete it. Use this page for your epilogue or conclusion if applicable; please  
1821 use only one of the titles for this page. Otherwise, you may delete it. Use this page for your  
1822 epilogue or conclusion if applicable; please use only one of the titles for this page. Otherwise,  
1823 you may delete it. Use this page for your epilogue or conclusion if applicable; please use only one  
1824 of the titles for this page. Otherwise, you may delete it. Use this page for your epilogue or  
1825 conclusion if applicable; please use only one of the titles for this page. Otherwise, you may delete  
1826 it. Use this page for your epilogue or conclusion if applicable; please use only one of the titles for  
1827 this page. Otherwise, you may delete it. Use this page for your epilogue or conclusion if  
1828 applicable; please use only one of the titles for this page. Otherwise, you may delete it. Use this  
1829 page for your epilogue or conclusion if applicable; please use only one of the titles for this page.  
1830 Otherwise, you may delete it. Use this page for your epilogue or conclusion if applicable; please  
1831 use only one of the titles for this page. Otherwise, you may delete it. Use this page for your  
1832 epilogue or conclusion if applicable; please use only one of the titles for this page. Otherwise,  
1833 you may delete it. Use this page for your epilogue or conclusion if applicable; please use only one  
1834 of the titles for this page. Otherwise, you may delete it. Use this page for your epilogue or  
1835 conclusion if applicable; please use only one of the titles for this page. Otherwise, you may delete  
1836 it. Use this page for your epilogue or conclusion if applicable; please use only one of the titles for  
1837 this page. Otherwise, you may delete it. Use this page for your epilogue or conclusion if  
1838 applicable; please use only one of the titles for this page. Otherwise, you may delete it. Use this  
1839 page for your epilogue or conclusion if applicable; please use only one of the titles for this page.  
1840 Otherwise, you may delete it. Use this page for your epilogue or conclusion if applicable; please  
1841 use only one of the titles for this page. Otherwise, you may delete it. Use this page for your  
1842 epilogue or conclusion if applicable; please use only one of the titles for this page. Otherwise,

1843 you may delete it. Use this page for your epilogue or conclusion if applicable; please use only one  
1844 of the titles for this page. Otherwise, you may delete it. Use this page for your epilogue or  
1845 conclusion if applicable; please use only one of the titles for this page. Otherwise, you may delete  
1846 it. Use this page for your epilogue or conclusion if applicable; please use only one of the titles for  
1847 this page. Otherwise, you may delete it. Use this page for your epilogue or conclusion if  
1848 applicable; please use only one of the titles for this page. Otherwise, you may delete it. Use this  
1849 page for your epilogue or conclusion if applicable; please use only one of the titles for this page.  
1850 Otherwise, you may delete it. Use this page for your epilogue or conclusion if applicable; please  
1851 use only one of the titles for this page. Otherwise, you may delete it. Use this page for your  
1852 epilogue or conclusion if applicable; please use only one of the titles for this page. Otherwise,  
1853 you may delete it. Use this page for your epilogue or conclusion if applicable; please use only one  
1854 of the titles for this page. Otherwise, you may delete it. Use this page for your epilogue or  
1855 conclusion if applicable; please use only one of the titles for this page. Otherwise, you may delete  
1856 it. Use this page for your epilogue or conclusion if applicable; please use only one of the titles for  
1857 this page. Otherwise, you may delete it. Use this page for your epilogue or conclusion if  
1858 applicable; please use only one of the titles for this page. Otherwise, you may delete it. Use this  
1859 page for your epilogue or conclusion if applicable; please use only one of the titles for this page.  
1860 Otherwise, you may delete it. Use this page for your epilogue or conclusion if applicable; please  
1861 use only one of the titles for this page. Otherwise, you may delete it. Use this page for your  
1862 epilogue or conclusion if applicable; please use only one of the titles for this page. Otherwise,  
1863 you may delete it. Use this page for your epilogue or conclusion if applicable; please use only one  
1864 of the titles for this page. Otherwise, you may delete it. Use this page for your epilogue or  
1865 conclusion if applicable; please use only one of the titles for this page. Otherwise, you may delete  
1866 it. Use this page for your epilogue or conclusion if applicable; please use only one of the titles for  
1867 this page. Otherwise, you may delete it. Use this page for your epilogue or conclusion if  
1868 applicable; please use only one of the titles for this page. Otherwise, you may delete it. Use this  
1869 page for your epilogue or conclusion if applicable; please use only one of the titles for this page.

1870 Otherwise, you may delete it. Use this page for your epilogue or conclusion if applicable; please  
1871 use only one of the titles for this page. Otherwise, you may delete it. Use this page for your  
1872 epilogue or conclusion if applicable; please use only one of the titles for this page. Otherwise,  
1873 you may delete it. Use this page for your epilogue or conclusion if applicable; please use only one  
1874 of the titles for this page. Otherwise, you may delete it. Use this page for your epilogue or  
1875 conclusion if applicable; please use only one of the titles for this page. Otherwise, you may delete  
1876 it. Use this page for your epilogue or conclusion if applicable; please use only one of the titles for  
1877 this page. Otherwise, you may delete it. Use this page for your epilogue or conclusion if  
1878 applicable; please use only one of the titles for this page. Otherwise, you may delete it. Use this  
1879 page for your epilogue or conclusion if applicable; please use only one of the titles for this page.  
1880 Otherwise, you may delete it. Use this page for your epilogue or conclusion if applicable; please  
1881 use only one of the titles for this page. Otherwise, you may delete it. Use this page for your  
1882 epilogue or conclusion if applicable; please use only one of the titles for this page. Otherwise,  
1883 you may delete it. Use this page for your epilogue or conclusion if applicable; please use only one  
1884 of the titles for this page. Otherwise, you may delete it. Use this page for your epilogue or  
1885 conclusion if applicable; please use only one of the titles for this page. Otherwise, you may delete  
1886 it. Use this page for your epilogue or conclusion if applicable; please use only one of the titles for  
1887 this page. Otherwise, you may delete it. Use this page for your epilogue or conclusion if  
1888 applicable; please use only one of the titles for this page. Otherwise, you may delete it. Use this  
1889 page for your epilogue or conclusion if applicable; please use only one of the titles for this page.  
1890 Otherwise, you may delete it. Use this page for your epilogue or conclusion if applicable; please  
1891 use only one of the titles for this page. Otherwise, you may delete it. Use this page for your  
1892 epilogue or conclusion if applicable; please use only one of the titles for this page. Otherwise,  
1893 you may delete it. Use this page for your epilogue or conclusion if applicable; please use only one  
1894 of the titles for this page. Otherwise, you may delete it. Use this page for your epilogue or  
1895 conclusion if applicable; please use only one of the titles for this page. Otherwise, you may delete  
1896 it.

## References

- [1] Jens Erler and Paul Langacker. “Electroweak model and constraints on new physics”. In: (July 2004). arXiv: hep-ph/0407097.
- [2] David J Griffiths. *Introduction to elementary particles; 2nd rev. version*. Physics textbook. New York, NY: Wiley, 2008.
- [3] M. Tanabashi et al. “Review of Particle Physics”. In: *Phys. Rev. D* 98 (3 2018), pp. 847–851.
- [4] E. Noether. “Invariante Variationsprobleme”. In: *Nachr. d. König. Gesellsch. d. Wiss. zu Göttingen, Math-phys. Klasse*, Seite 235–157 (1918). eprint: www.physics.ucla.edu/\sim\cwp/articles/noether.trans/german/emmy235.html.
- [5] J. H. Christenson et al. “Evidence for the  $2\pi$  Decay of the  $K_2^0$  Meson”. In: *Phys. Rev. Lett.* 13 (1964), pp. 138–140.
- [6] Michael Gronau. “CP Violation in B Meson Decays”. In: *Nuclear Physics B - Proceedings Supplements* 142 (May 2005), 263–270.
- [7] J. E. Augustin et al. “Discovery of a Narrow Resonance in  $e^+e^-$  Annihilation”. In: *Phys. Rev. Lett.* 33 (1974), pp. 1406–1408.
- [8] J. J. Aubert et al. “Experimental Observation of a Heavy Particle  $J$ ”. In: *Phys. Rev. Lett.* 33 (1974), pp. 1404–1406.
- [9] Martin L. Perl et al. “Evidence for Anomalous Lepton Production in  $e^+ - e^-$  Annihilation”. In: *Phys. Rev. Lett.* 35 (1975), pp. 1489–1492.
- [10] S. W. Herb et al. “Observation of a Dimuon Resonance at 9.5-GeV in 400-GeV Proton-Nucleus Collisions”. In: *Phys. Rev. Lett.* 39 (1977), pp. 252–255.
- [11] F. Abe et al. “Observation of top quark production in  $\bar{p}p$  collisions”. In: *Phys. Rev. Lett.* 74 (1995), pp. 2626–2631. arXiv: hep-ex/9503002.
- [12] S. Abachi et al. “Observation of the top quark”. In: *Phys. Rev. Lett.* 74 (1995), pp. 2632–2637. arXiv: hep-ex/9503003.
- [13] K. Kodama et al. “Observation of tau neutrino interactions”. In: *Phys. Lett. B* 504 (2001), pp. 218–224. arXiv: hep-ex/0012035.

- 1924 [14] G. Arnison et al. “Experimental Observation of Lepton Pairs of Invariant Mass Around 95-  
 1925 GeV/c\*\*2 at the CERN SPS Collider”. In: *Phys. Lett. B* 126 (1983), pp. 398–410.
- 1926 [15] P. Bagnaia et al. “Evidence for  $Z^0 \rightarrow e^+e^-$  at the CERN  $\bar{p}p$  Collider”. In: *Phys. Lett. B* 129  
 1927 (1983), pp. 130–140.
- 1928 [16] Serguei Chatrchyan et al. “Observation of a New Boson at a Mass of 125 GeV with the  
 1929 CMS Experiment at the LHC”. In: *Phys. Lett. B* 716 (2012), pp. 30–61. arXiv: 1207.7235  
 1930 [hep-ex].
- 1931 [17] Georges Aad et al. “Observation of a new particle in the search for the Standard Model  
 1932 Higgs boson with the ATLAS detector at the LHC”. In: *Phys. Lett. B* 716 (2012), pp. 1–29.  
 1933 arXiv: 1207.7214 [hep-ex].
- 1934 [18] K. G. Begeman, A. H. Broeils, and R. H. Sanders. “Extended rotation curves of spiral galaxies:  
 1935 Dark haloes and modified dynamics”. In: *Mon. Not. Roy. Astron. Soc.* 249 (1991), p. 523.
- 1936 [19] Y. Ashie et al. “Evidence for an oscillatory signature in atmospheric neutrino oscillation”.  
 1937 In: *Phys. Rev. Lett.* 93 (2004), p. 101801. arXiv: hep-ex/0404034.
- 1938 [20] C. Abel et al. “Measurement of the Permanent Electric Dipole Moment of the Neutron”. In:  
 1939 *Phys. Rev. Lett.* 124.8 (2020), p. 081803. arXiv: 2001.11966 [hep-ex].
- 1940 [21] Guillaume Albouy et al. “Theory, phenomenology, and experimental avenues for dark showers:  
 1941 a Snowmass 2021 report”. In: *The European Physical Journal C* 82.12 (Dec. 2022).
- 1942 [22] Timothy Cohen et al. “LHC searches for dark sector showers”. In: *Journal of High Energy  
 1943 Physics* 2017.11 (Nov. 2017).
- 1944 [23] Lyndon Evans and Philip Bryant. “LHC Machine”. In: *Journal of Instrumentation* 3.08  
 1945 (2008), S08001.
- 1946 [24] “The ATLAS Experiment at the CERN Large Hadron Collider”. In: *JINST* 3 (2008). Also  
 1947 published by CERN Geneva in 2010, S08003.
- 1948 [25] “The CMS experiment at the CERN LHC”. In: *Journal of Instrumentation* 3.08 (2008),  
 1949 S08004.
- 1950 [26] “The ALICE experiment at the CERN LHC”. In: *Journal of Instrumentation* 3.08 (2008),  
 1951 S08002.
- 1952 [27] “The LHCb Detector at the LHC”. In: *Journal of Instrumentation* 3.08 (2008), S08005.
- 1953 [28] Ana Lopes and Melissa Loyse Perrey. *FAQ-LHC The guide*. 2022.

- 1954 [29] Esma Mobs. “The CERN accelerator complex in 2019. Complexe des accélérateurs du  
1955 CERN en 2019”. In: (2019). General Photo.
- 1956 [30] *Pulling together: Super Conducting electromagnets*. <https://home.cern/science/engineering/pulling-together-superconducting-electromagnets>.  
1957 Accessed: 2024-01-05.  
1958
- 1959 [31] *The High-Luminosity LHC*. <https://voisins.web.cern.ch/en/high-luminosity-lhc-hl-lhc>. Accessed: 2024-01-05.  
1960
- 1961 [32] Aad G., et al. (ATLAS Collaboration and CMS Collaboration). “Combined Measurement of  
1962 the Higgs Boson Mass in pp Collisions at  $\sqrt{s} = 7$  and 8 TeV with the ATLAS and CMS  
1963 Experiments”. In: *Phys. Rev. Lett.* 114 (19 2015), p. 191803.
- 1964 [33] O. Aberle et al. *High-Luminosity Large Hadron Collider (HL-LHC): Technical design re-*  
1965 *port*. CERN Yellow Reports: Monographs. Geneva: CERN, 2020.
- 1966 [34] The ATLAS Collaboration. “The ATLAS Experiment at the CERN Large Hadron Collider”.  
1967 In: *Journal of Instrumentation* 3.08 (2008), S08003.
- 1968 [35] G Aad, B Abbott, and ATLAS Collaboration. “Performance of the reconstruction of large  
1969 impact parameter tracks in the inner detector of ATLAS”. In: *Eur. Phys. J. C Part. Fields*  
1970 83.11 (Nov. 2023).
- 1971 [36] Joao Pequenao. *Computer Generated image of the ATLAS calorimeter*. 2008.
- 1972 [37] *ATLAS liquid-argon calorimeter: Technical Design Report*. Technical design report. AT-  
1973 LAS. Geneva: CERN, 1996.
- 1974 [38] H A Gordon. “Liquid argon calorimetry for the SSC”. In: () .
- 1975 [39] Henric Wilkens and (on behalf of the ATLAS LArg Collaboration). “The ATLAS Liquid  
1976 Argon calorimeter: An overview”. In: *Journal of Physics: Conference Series* 160.1 (2009),  
1977 p. 012043.
- 1978 [40] *Technical Design Report for the Phase-II Upgrade of the ATLAS Tile Calorimeter*. Tech.  
1979 rep. Geneva: CERN, 2017.
- 1980 [41] “Technical Design Report for the Phase-II Upgrade of the ATLAS Muon Spectrometer”. In:  
1981 () .
- 1982 [42] L Pontecorvo. “The ATLAS Muon Spectrometer”. In: (2004). revised version number 1  
1983 submitted on 2003-07-27 16:31:16.

- 1984 [43] *ATLAS magnet system: Technical Design Report, 1*. Technical design report. ATLAS. Geneva:  
 1985 CERN, 1997.
- 1986 [44] Joao Pequenao. “Event Cross Section in a computer generated image of the ATLAS detector.” 2008.  
 1987
- 1988 [45] ATLAS Collaboration. “ATLAS Experiment Implements Heterogeneous Particle Recon-  
 1989 struction with Intel oneAPI Tools”. General Photo. 2023.
- 1990 [46] ATLAS Collaboration. “Electron and photon performance measurements with the ATLAS  
 1991 detector using the 2015–2017 LHC proton-proton collision data”. In: *Journal of Instrumen-*  
 1992 *tation* 14.12 (2019), P12006.
- 1993 [47] Chiara Deponte. “Studies on the properties of non-prompt photons at the ATLAS experi-  
 1994 ment”. Presented 16 Aug 2022. Technische Universitaet Dortmund (DE), 2022.
- [48] ATLAS Collaboration. “Muon reconstruction performance of the ATLAS detector in pro-  
 ton–proton collision data at  $\sqrt{s}$   
 1995  $s = 13 \text{ TeV}$ ”. In: *The European Physical Journal C* 76.5 (2016).
- 1996 [49] Sebastien Rettie. *Muon identification and performance in the ATLAS experiment*. Tech. rep.  
 1997 Geneva: CERN, 2018.
- 1998 [50] B. R. Webber. *Fragmentation and Hadronization*. 1999. arXiv: hep-ph/9912292 [hep-ph].
- 1999 [51] Eric M. Metodiev. *The Fractal Lives of Jets* | Eric M. Metodiev — ericmetodiev.com. https://  
 2000 //www.ericmetodiev.com/post/jetformation/. 2019, note = [Accessed 18-  
 2001 05-2024],
- 2002 [52] Matteo Cacciari, Gavin P Salam, and Gregory Soyez. “The anti-ktjet clustering algorithm”.  
 2003 In: *Journal of High Energy Physics* 2008.04 (Apr. 2008), 063–063.
- 2004 [53] Matteo Cacciari, Gavin P. Salam, and Gregory Soyez. “FastJet user manual: (for version  
 2005 3.0.2)”. In: *The European Physical Journal C* 72.3 (Mar. 2012).
- 2006 [54] Steven Schramm. *ATLAS Jet Reconstruction, Calibration, and Tagging of Lorentz-boosted  
 2007 Objects*. Tech. rep. Geneva: CERN, 2017.
- 2008 [55] ATLAS Collaboration. “Topological cell clustering in the ATLAS calorimeters and its per-  
 2009 formance in LHC Run 1”. In: *The European Physical Journal C* 77.7 (July 2017).
- 2010 [56] ATLAS Collaboration. “Jet reconstruction and performance using particle flow with the  
 2011 ATLAS Detector”. In: *The European Physical Journal C* 77.7 (July 2017).

- 2012 [57] Stephen D. Ellis and Davison E. Soper. “Successive combination jet algorithm for hadron  
2013 collisions”. In: *Physical Review D* 48.7 (Oct. 1993), 3160–3166.
- 2014 [58] M. Wobisch and T. Wengler. *Hadronization Corrections to Jet Cross Sections in Deep-*  
2015 *Inelastic Scattering*. 1999. arXiv: hep-ph/9907280 [hep-ph].
- 2016 [59] Gavin P Salam and Gr  gory Soyez. “A practical seedless infrared-safe cone jet algorithm”.  
2017 In: *Journal of High Energy Physics* 2007.05 (May 2007), 086–086.
- 2018 [60] Gavin P. Salam. “Towards jetography”. In: *The European Physical Journal C* 67.3–4 (May  
2019), 637–686.
- 2020 [61] *A Monte Carlo study of track association to jets for b-tagging*. Tech. rep. Geneva: CERN,  
2021.
- 2022 [62] *Flavor Tagging with Track Jets in Boosted Topologies with the ATLAS Detector*. Tech. rep.  
2023 All figures including auxiliary figures are available at <https://atlas.web.cern.ch/Atlas/GROUPS/PHYSICS/P>  
2024 PHYS-PUB-2014-013. Geneva: CERN, 2014.
- 2025 [63] ATLAS Collaboration. “Performance of missing transverse momentum reconstruction with  
2026 the ATLAS detector using proton-proton collisions at  $\sqrt{s} = 13$  TeV”. In: *Eur. Phys. J. C*  
2027 78.11 (2018), p. 903. arXiv: 1802.08168.
- 2028 [64] GEANT4 Collaboration, S. Agostinelli, et al. “GEANT4 – a simulation toolkit”. In: *Nucl.*  
2029 *Instrum. Meth. A* 506 (2003), p. 250.
- 2030 [65] Christian Bierlich et al. *A comprehensive guide to the physics and usage of PYTHIA 8.3*.  
2031 2022. arXiv: 2203.11601 [hep-ph].
- 2032 [66] J. Alwall et al. “The automated computation of tree-level and next-to-leading order differ-  
2033 ential cross sections, and their matching to parton shower simulations”. In: *JHEP* 07 (2014),  
2034 p. 079. arXiv: 1405.0301 [hep-ph].
- 2035 [67] Jon Butterworth et al. “PDF4LHC recommendations for LHC Run II”. In: *J. Phys. G* 43  
2036 (2016), p. 023001. arXiv: 1510.03865 [hep-ph].
- 2037 [68] Peter Skands, Stefano Carrazza, and Juan Rojo. “Tuning PYTHIA 8.1: the Monash 2013  
2038 Tune”. In: *Eur. Phys. J. C* 74.8 (2014), p. 3024. arXiv: 1404.5630 [hep-ph].
- 2039 [69] Patrick T. Komiske, Eric M. Metodiev, and Jesse Thaler. “Energy flow networks: deep sets  
2040 for particle jets”. In: *Journal of High Energy Physics* 2019.1 (2019).
- 2041 [70] A. Kahn et al. “Anomalous jet identification via sequence modeling”. In: *Journal of Instru-*  
2042 *mentation* 16.08 (Aug. 2021), P08012.

- 2043 [71] Georges Aad et al. “Anomaly detection search for new resonances decaying into a Higgs  
2044 boson and a generic new particle  $X$  in hadronic final states using  $\sqrt{s} = 13$  TeV  $pp$  collisions  
2045 with the ATLAS detector”. In: *Phys. Rev. D* 108 (2023), p. 052009. arXiv: 2306.03637  
2046 [[hep-ex](#)].
- 2047 [72] The ATLAS Collaboration. “Search for diboson resonances in hadronic final states in 139  
2048 fb-1 of  $pp$  collisions at  $\sqrt{s} = 13$  TeV with the ATLAS detector”. In: *Journal of High Energy*  
2049 *Physics* 2019.9 (Sept. 2019).
- 2050 [73] *Recommendations for the Modeling of Smooth Backgrounds*. Tech. rep. Geneva: CERN,  
2051 2020.
- 2052 [74] The CMS Collaboration. “Search for resonant production of strongly coupled dark matter  
2053 in proton-proton collisions at 13 TeV”. In: *Journal of High Energy Physics* 2022.6 (June  
2054 2022).

## Appendix A: Trigger Studies

2057 Both the lowest unprescaled  $E_T^{\text{miss}}$  and single small-R jet triggers were considered for this  
 2058 analysis. The  $E_T^{\text{miss}}$  trigger is observed to have higher efficiency for low mass, high  $R_{\text{inv}}$  points,  
 2059 while the single small-R trigger favors high mass, low  $R_{\text{inv}}$  points. Figure A.1 shows the yields  
 2060 and signal efficiencies across the grid for both these strategies.

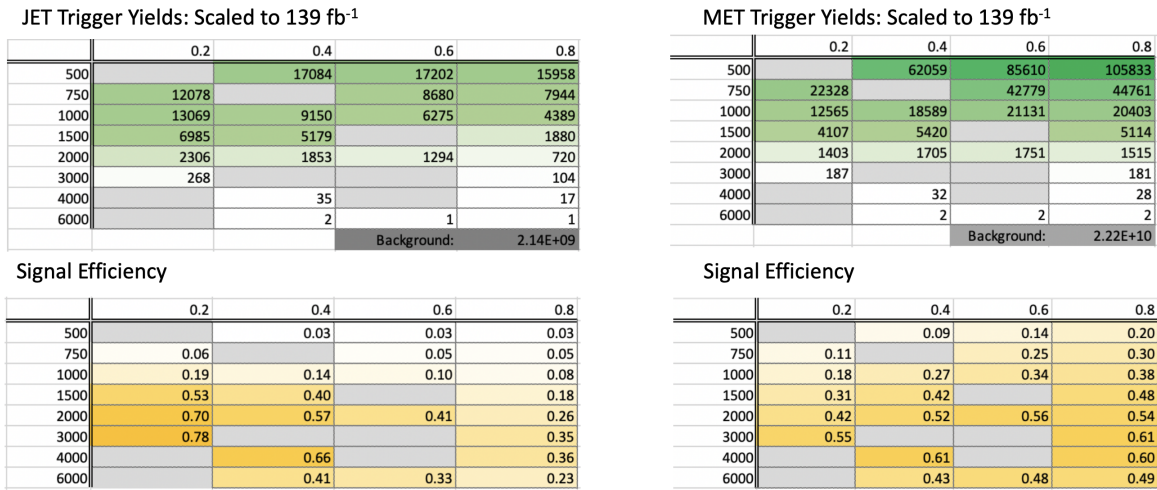


Figure A.1: Trigger yield and efficiency for both the MET trigger and small-R jet trigger approach. Each entry represent a signal point, labelled by the  $Z'$  mass and the  $R_{\text{inv}}$  fraction.

2061 The cross section is higher for the lower  $Z'$  mass signal points. As a result, our sensitivity  
 2062 to these points and ability to set limits on them is already naturally enhanced. Figure A.2 shows  
 2063 the factor of improvement in the inclusive  $S/\sqrt{B}$  using each trigger strategy. A cross-check was  
 2064 also done calculating  $S/\sqrt{B}$  in windows around the mT mass. The results of this cross-check  
 2065 confirmed the results shown in Figure A.2.

2066 Figure A.3 shows the ratio of  $S/\sqrt{B}$  across the signal grid for the jet trigger compared to the  
 2067  $E_T^{\text{miss}}$  trigger.

2068 This plot makes clear that the  $E_T^{\text{miss}}$  trigger favors the low mass, high  $R_{\text{inv}}$  signal points, while

$(\text{JET Trigger } S/\sqrt{B}) / (\text{Untriggered } S/\sqrt{B})$				
	0.2	0.4	0.6	0.8
500		1.26	1.43	1.53
750	2.99		2.52	2.68
1000	9.24	6.74	5.03	4.07
1500	26.45	20.15		8.83
2000	34.66	28.24	20.57	12.85
3000	39.05			17.35
4000		32.94		17.96
6000		20.57	16.55	11.53

$(\text{MET Trigger } S/\sqrt{B}) / (\text{Untriggered } S/\sqrt{B})$				
	0.2	0.4	0.6	0.8
500		1.43	2.21	3.15
750	1.72		3.86	4.69
1000	2.76	4.26	5.26	5.89
1500	4.83	6.56		7.47
2000	6.55	8.08	8.65	8.40
3000	8.46			9.38
4000		9.51		9.32
6000		6.68	7.43	7.59

Figure A.2: The factor of improvement in  $S/\sqrt{B}$  for each trigger method compared to the untriggered case.

	0.2	0.4	0.6	0.8
500		0.89	0.65	0.49
750	1.74		0.65	0.57
1000	3.35	1.58	0.96	0.69
1500	5.47	3.07		1.18
2000	5.29	3.49	2.38	1.53
3000	4.62			1.85
4000		3.46		1.93
6000		3.08	2.23	1.52

Figure A.3: The ratio of  $S/\sqrt{B}$  of jet trigger over  $E_T^{\text{miss}}$  trigger selection.

2069 the single jet trigger favors the high mass, low  $R_{inv}$  signal points. A number of considerations led  
2070 us to selecting the single jet trigger. First, Figure A.2 illustrates that the sensitivity enhancement is  
2071 greater for signals favored by the jet trigger than signals favored by the  $E_T^{\text{miss}}$  trigger. This indicates  
2072 we have more to gain from focusing on the region of our signal grid where the jet trigger is most  
2073 efficient. We combined this with the observation that the jet trigger is beneficial for high mass  
2074 points where the cross-section is lower and we need to maximize sensitivity to hope to set limits  
2075 on these points.

2076 Second, there are a number of analysis variables at our disposal which are more discriminant for  
2077 high  $R_{inv}$  signals than for low  $R_{inv}$  signals. A collection of these variables are shown in Figure A.4.  
2078 Given that we had multiple avenues available to enhance sensitivity to low  $R_{inv}$  signals through  
2079 analysis strategy cuts, we opted for a trigger strategy that benefitted the low  $R_{inv}$  signal points.  
2080 Additionally, we know  $E_T^{\text{miss}}$  is highly correlated with these discriminant analysis variables, and a  
2081  $E_T^{\text{miss}}$  trigger would reduce the effectiveness of these variables. Not implementing the  $E_T^{\text{miss}}$  trigger  
2082 allows us to explore other ways of leveraging  $E_T^{\text{miss}}$  in the analysis using a cut that is more finely  
2083 tuned to the specifics of the signal model than the  $E_T^{\text{miss}}$  trigger is.

2084 Third, we know that fitting the high  $R_{inv}$  mass points would be challenging given their very  
2085 broad shapes in the key analysis variable  $m_T$ . Given the analysis decision to do a search for  
2086 resonant features in  $m_T$ , we chose to design a search that emphasized maximizing sensitivity  
2087 to the signal points that we were mostly to appear as a resonant feature in  $m_T$ . The shape of  
2088  $m_T$  and our reduced ability to set limits on high  $R_{inv}$  points is demonstrated in the body of this  
2089 note. Another search strategy may be more optimal for setting limits on high  $R_{inv}$  semi-visible jet  
2090 signals, but it is currently outside the scope of this analysis.

2091 A jet or  $E_T^{\text{miss}}$  trigger was also considered, but abandoned due to concerns about sculpting  
2092 features in the smoothly falling  $E_T^{\text{miss}}$  or leading jet  $p_T$  distributions, as shown in Figure A.5.

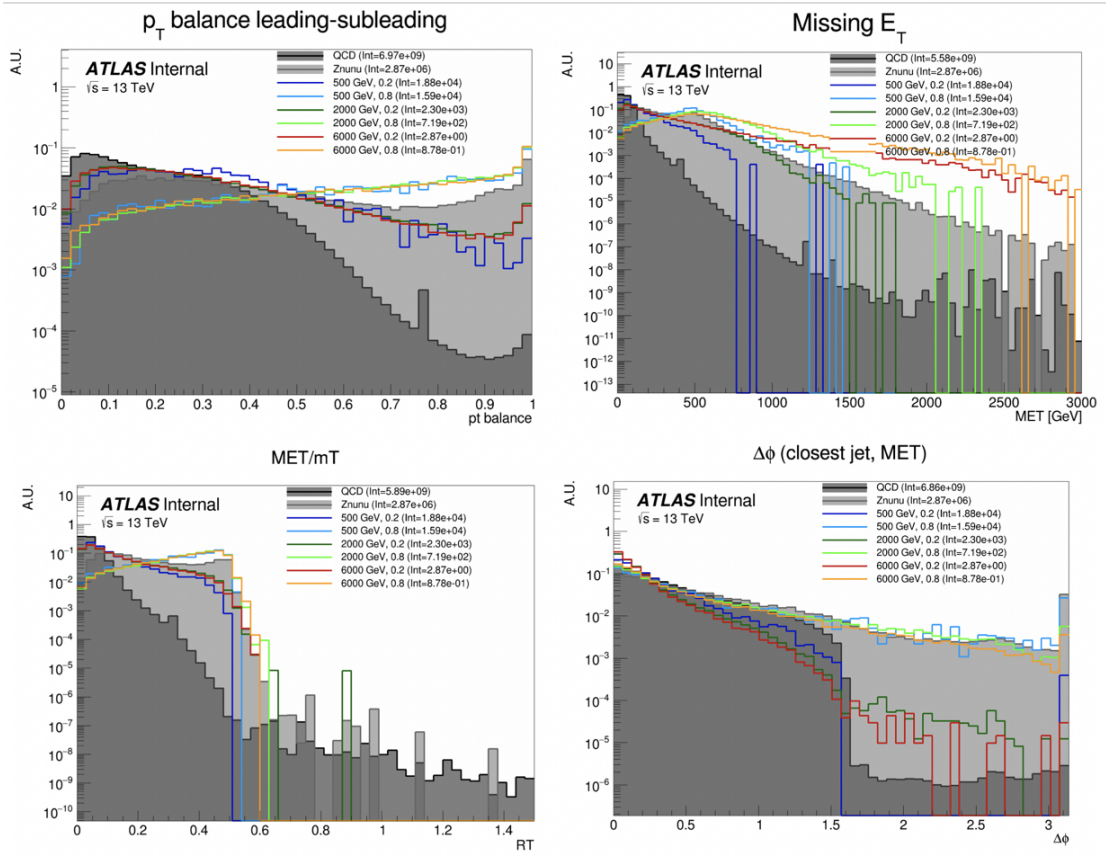


Figure A.4: Analysis variables where high  $R_{inv}$  signals a clearly distinct from background and low  $R_{inv}$  variables. On the contrary, leading jet  $p_T$  is one of the only variables where low  $R_{inv}$  signals are distinct from background.

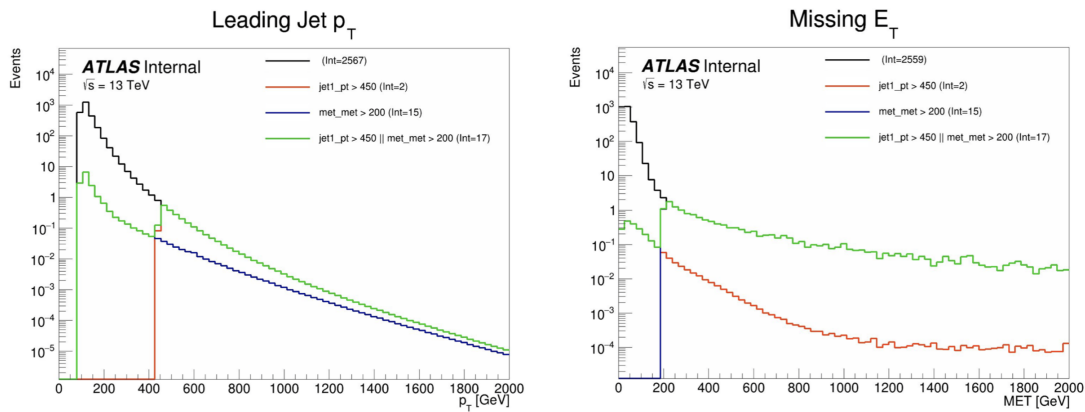


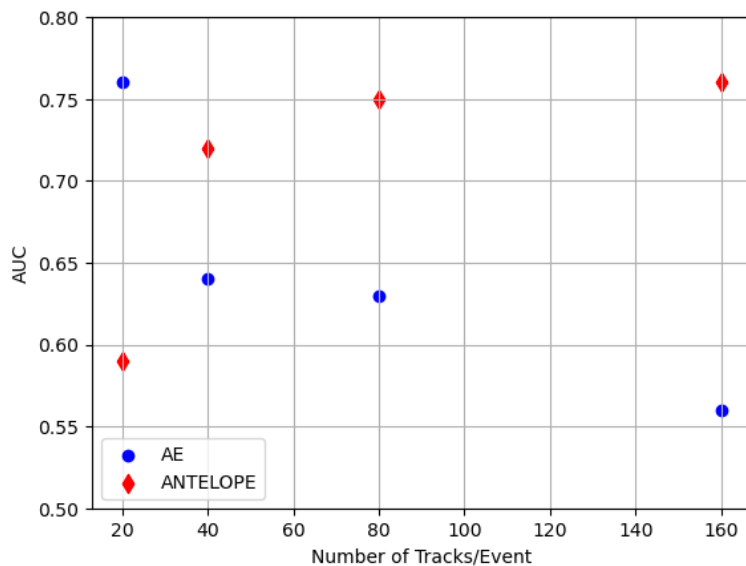
Figure A.5: OR of jet and  $E_T^{\text{miss}}$  triggers.

## Appendix B: Machine Learning Approaches

### 2095 B.1 Unsupervised: AE vs. ANTELOPE

2096 To understand the benefits of the semi-supervised ANTELOPE approach, we study the AN-  
 2097 TELOPE in comparison to a traditional anomaly detection architecture like an autoencoder. The  
 2098 autoencoder cannot accommodate variable length or permutation invariant inputs.

2099 Figure B.1 shows the AUC determined by each of these two tools as a function of number  
 2100 of tracks. The trend is that the AE suffers when more information is given, due to the presence  
 2101 of 0-padding. In contrast, the ANTELOPE architecture performs better with more information,  
 motivating the use of high dimensional input modelin with this method.

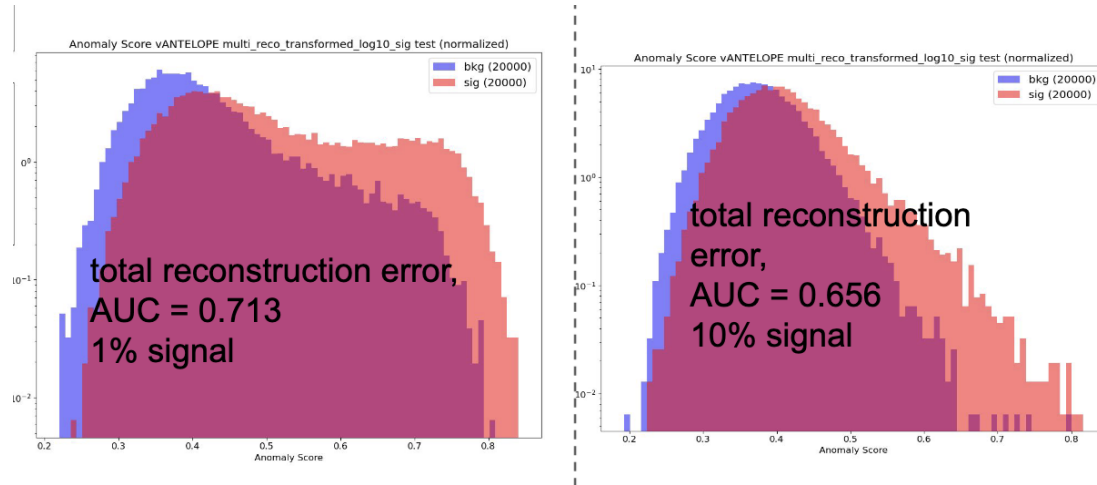


- Confirms that AE is negatively sensitive to zero padding while ANTELOPE sees a performance improvement as it sees more “information”

2102 Figure B.1

2103 **Signal Contamination**

2104 To understand the effect of signal contamination in training on the ANTELOPE score, we inject  
2105 a percent of signal events into the data used to train the ANTELOPE autoencoder stage and look  
2106 at the AUC on signals. Figure B.2 shows no variation in AUC with 1% contamination in training  
data, but a few % drop going up to 10%.



2107 Figure B.2

2108 **B.2 PFN Optimality Checks**

2109 The PFN is trained using QCD as the background. A study was done to compare the perfor-  
2110 mance of the tool in the analysis context if it trains against QCD or a representative MC background  
2111 considering the small fractions of other processes ( $V+jets$ , top) that would contribute at preselec-  
2112 tion. Figure B.3 shows the AUC across the grid for both training approaches, revealing better  
2113 performance if the tool focuses on learning QCD differences.

2114 Further studies were done to ensure the relatively optimality of the single PFN model, trained  
2115 over combined signals, across the grid. As the grid spans signals with a large range of  $E_T^{\text{miss}}$ , their  
2116 varying input features and background composition may be conducive to separate PFN models  
2117 trained on high and low  $E_T^{\text{miss}}$  signal points to better capture the signal-background differences.  
2118 Figure B.4 shows a comparison of the signal-inclusive PFN model performance and the perfor-

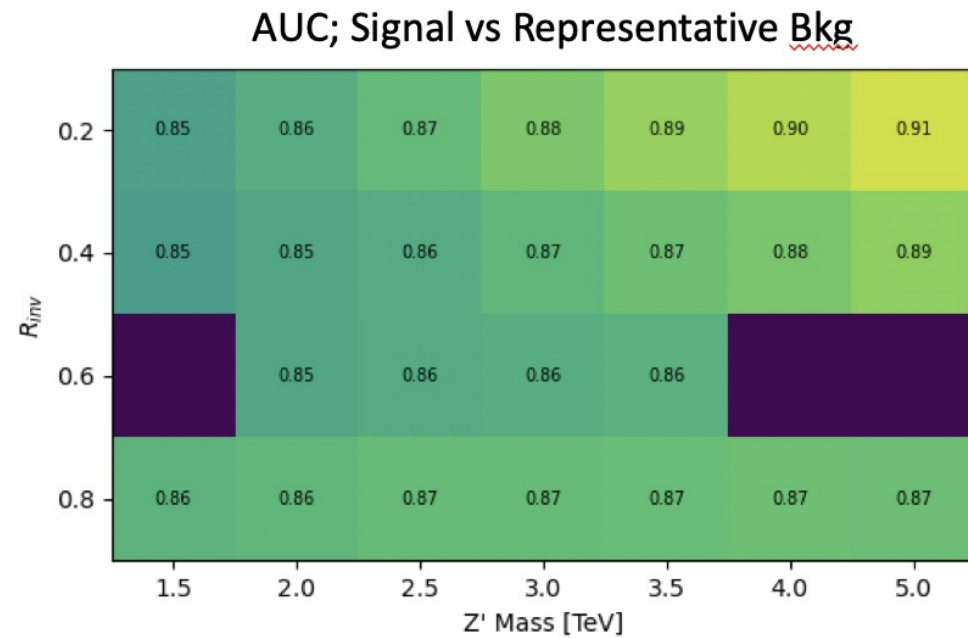
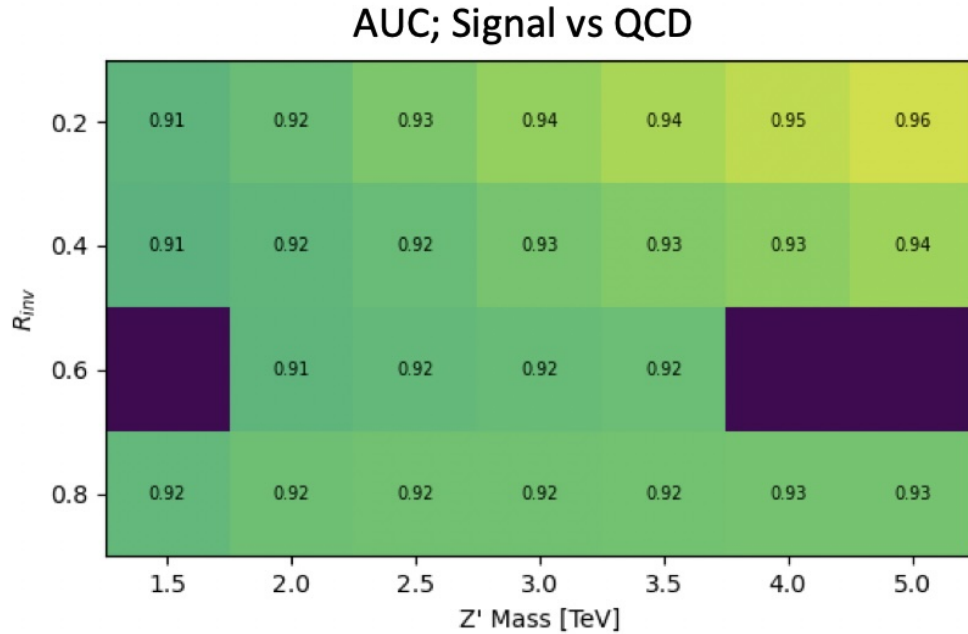


Figure B.3: AUC from the PFN score for each signal in the SVJ grid, shown versus the QCD-only training sample (top) and the total MC background (bottom). Note the three missing points will be added shortly - they were delayed due to a DAOD production mistake.

2119 mance of models separated into high and low  $R_{inv}$  signals in training. The most notable impact is  
 2120 found for the low  $R_{inv}$  and high mass points, indicating that the signal-inclusive PFN is learning  
 2121 morning about the distinction between high- $E_T^{\text{miss}}$  signals and backgrounds. However, these high  
 2122 mass points are also the most challenging to find due to their very wide resonance on top of  $m_T$ ,  
 2123 and in the final projected sensitivity in the  $m_T$  window the differences are  $< 10\%$  across the grid.  
 2124 To maintain a harmonized strategy with the ANTELOPE region we keep the inclusive PFN model  
 2125 as the final version.

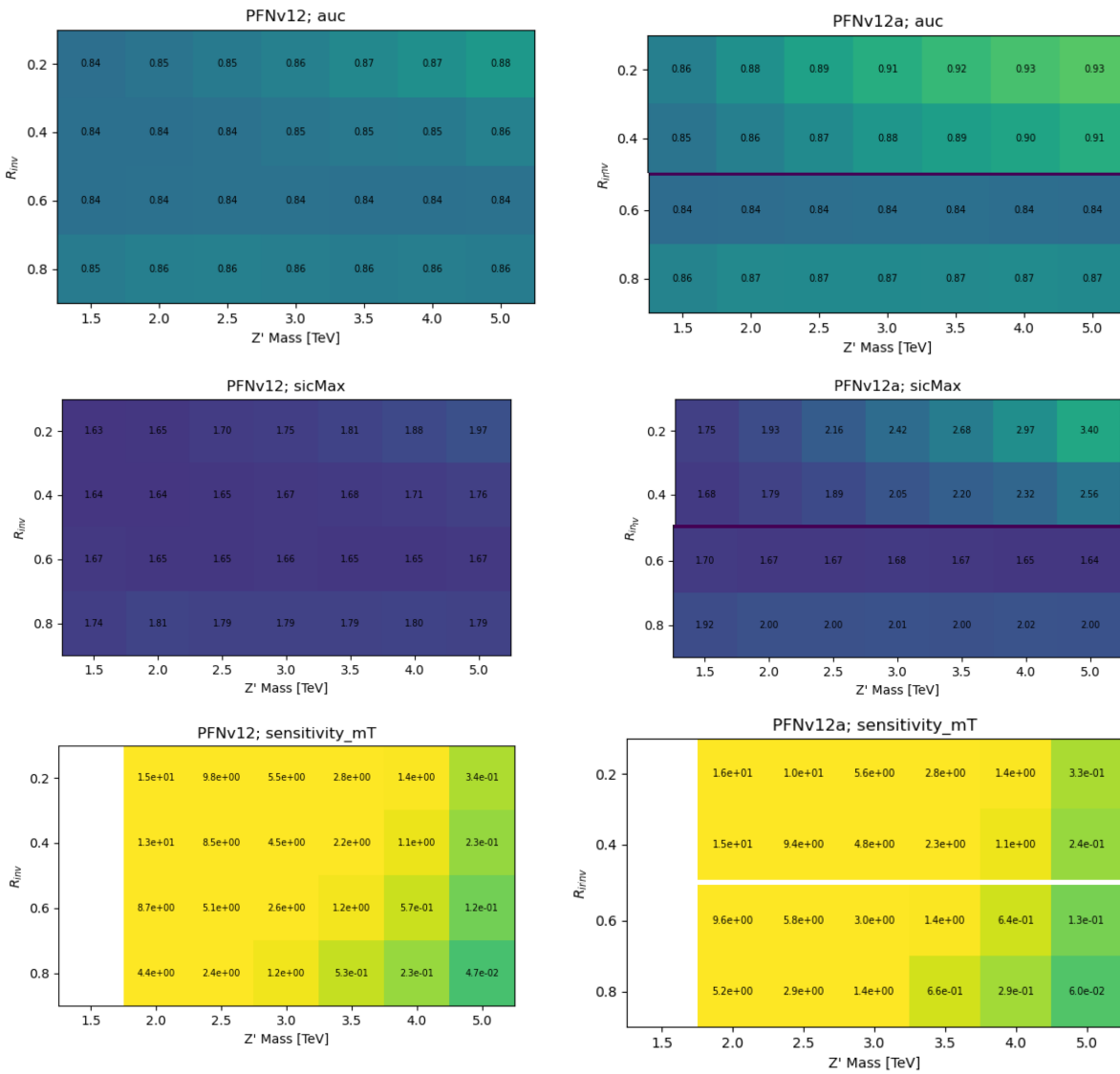


Figure B.4: Comparison of PFN AUC (top), SIC (middle), and sensitivity in the  $m_T$  mass window (bottom) for a single PFN model (left) vs. two models, trained on  $R_{inv} < 0.5$  and  $> 0.5$  separately.

2126      Figure B.5 shows the optimal cut on the PFN score for each point in the signal grid, motivating  
the loose inclusive choice used to define the SR.

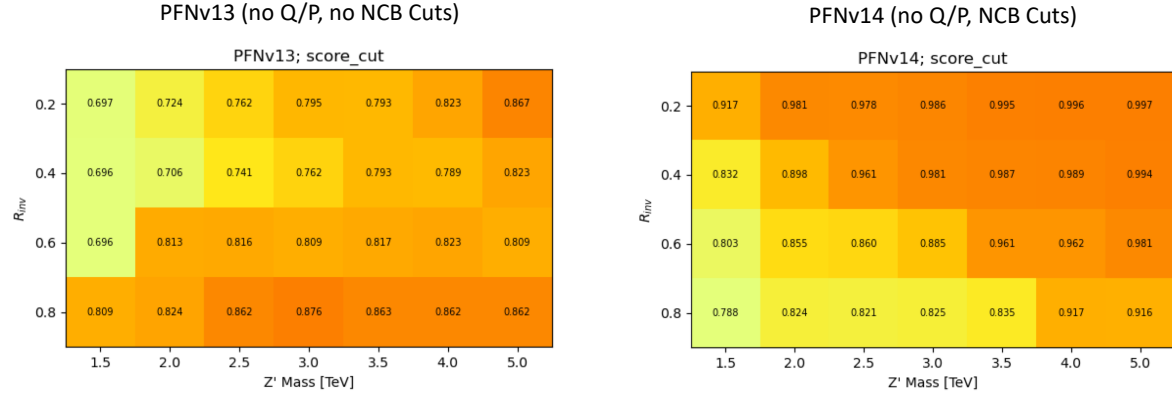


Figure B.5: Preferred cuts on the PFN score for each point in the grid, comparing the effect of adding the NCB preselection.

2127  
2128      Grid cans for optimality were also performed on the number of training epochs, number of  
2129      training events, batch size, learning rate, number of neurons, and dimension of the  $\Phi$  space. The  
2130      results of these scans are summarized in the tables in Figure B.6. The selected or default parameters  
2131      were found to be optimal, or close enough to optimal to justify not increasing the training time or  
2132      complexity of the network for negligible increases in performance.

### 2133      B.3 Supervised: BDT vs. PFN

2134      Studies of the BDT compared to the PFN performance, where training over events modeled  
2135      with jet-related HLVs (high-level track variables, etas, angles, etc.) are compared to events mod-  
2136      eled by the tracks of the 2 leading jets. Figure B.7 shows the performance of the BDT with and  
2137      without explicit use of energy scale variables.

### 2138      B.4 Supervised: Variable Correlations

2139      The correlation between the PFN score and analysis variables known to be unique to semi-  
2140      visible jets are studied, for the sake of better understanding the topology of the tool.  $\Delta\phi(j, E_T^{\text{miss}})$

	<b>default</b> s_events=500096 b_events=501396	s_events:49135 b_events: 48220 *	s_events:246205 b_events:245136
AUC	.905	.874	.892

	<b>default</b> n_neuro n 40	n_neuro n 150	phi_dim 32	phi_dim 128	learning rate 0.0005	learning rate 0.002	nepochs 50	nepochs 200*	
AUC	.905	.898	.906	.902	.906	.898	.905	.893	.909

	<b>default</b>	batchsize_pfn 250	batchsize_pfn 1000
AUC	.905	.903	.902

Figure B.6: Scans done to check for optimality of PFN training parameters.

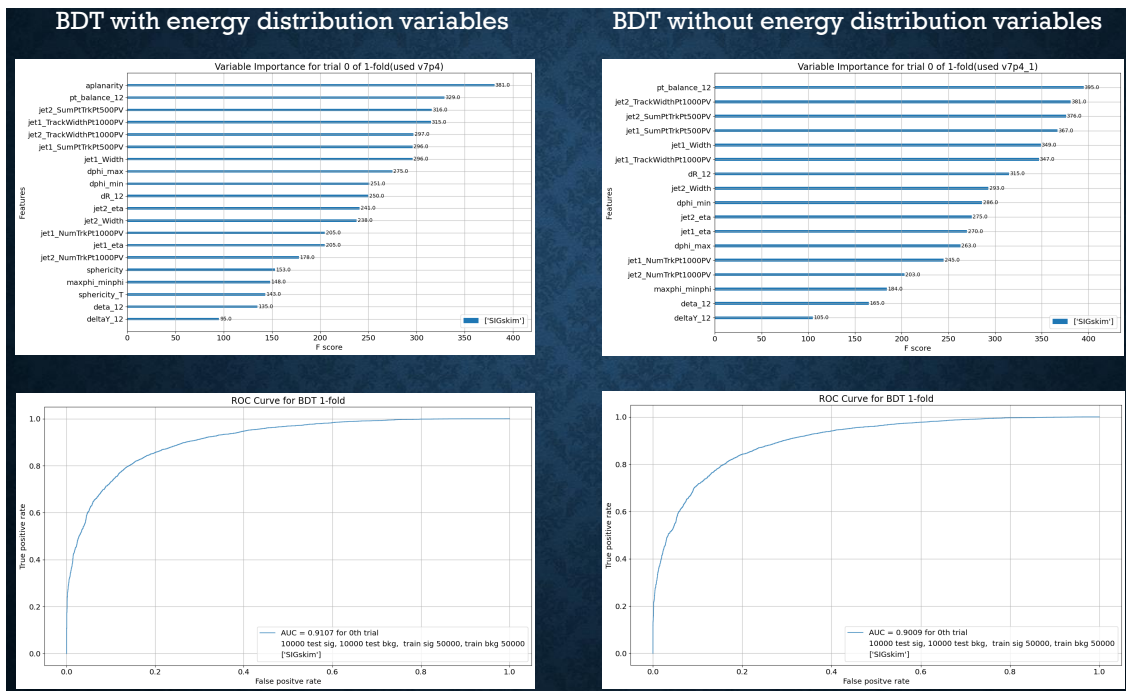


Figure B.7

2141 and  $\Delta\phi(j_1, j_2)$  in the CR and VR are highlighted in Figure B.8 (eg. in different bins of the PFN  
 2142 score), and 2D plots of the score with respect to the orientation variables are in Figure B.9.

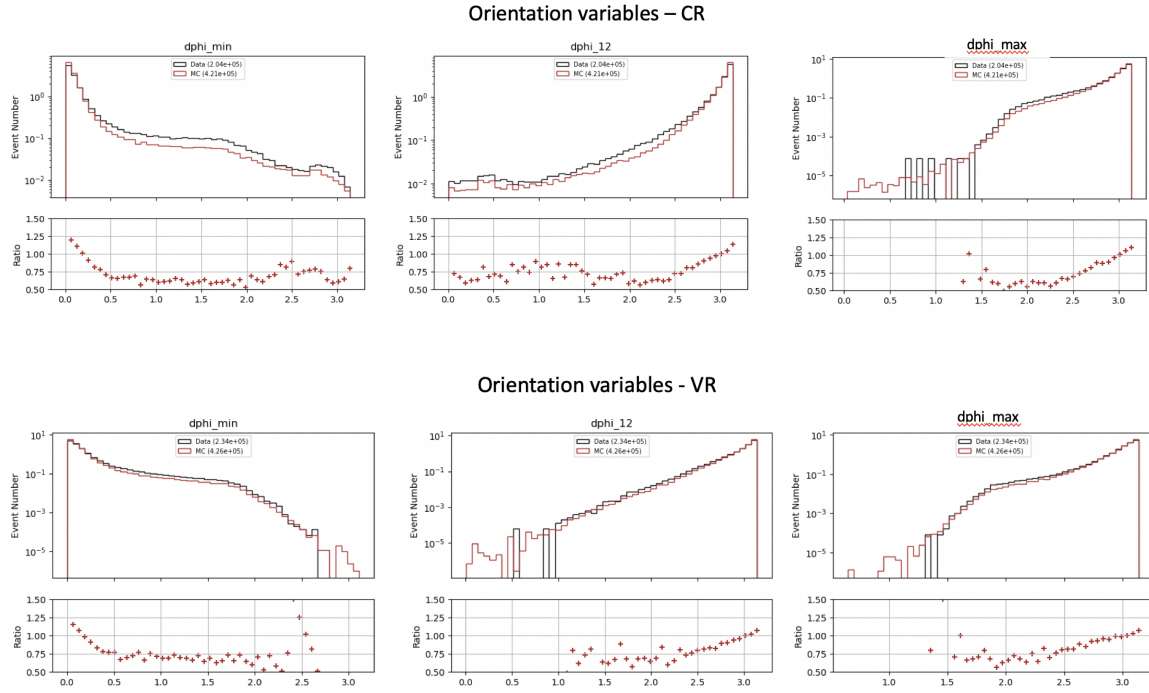


Figure B.8:  $\phi$  orientation variables in the CR and VR

## 2143 B.5 Single Jet vs Jet System ML Approach

2144 The analysis considered both a single jet and jet system ML approach. A jet system approach,  
 2145 where the leading two jets and their orientation with respect to each other was selected for a variety  
 2146 of reasons. The jet system approach captures the MET information which is crucial to identifying  
 2147 SVJs. In the topology where the dark quarks come from a heavy  $Z'$  decay and are back to back,  
 2148 the measurable MET will have to be aligned with one or the other.

2149 Additionally, the performance of both a supervised PFN approach and an unsupervised AE ap-  
 2150 proach was studied in the case of a single jet tagger. While the PFN approach was still performant  
 2151 on a single jet case, the unsupervised approach was significantly improved by using both jets. This  
 2152 is shown in Figure B.10.

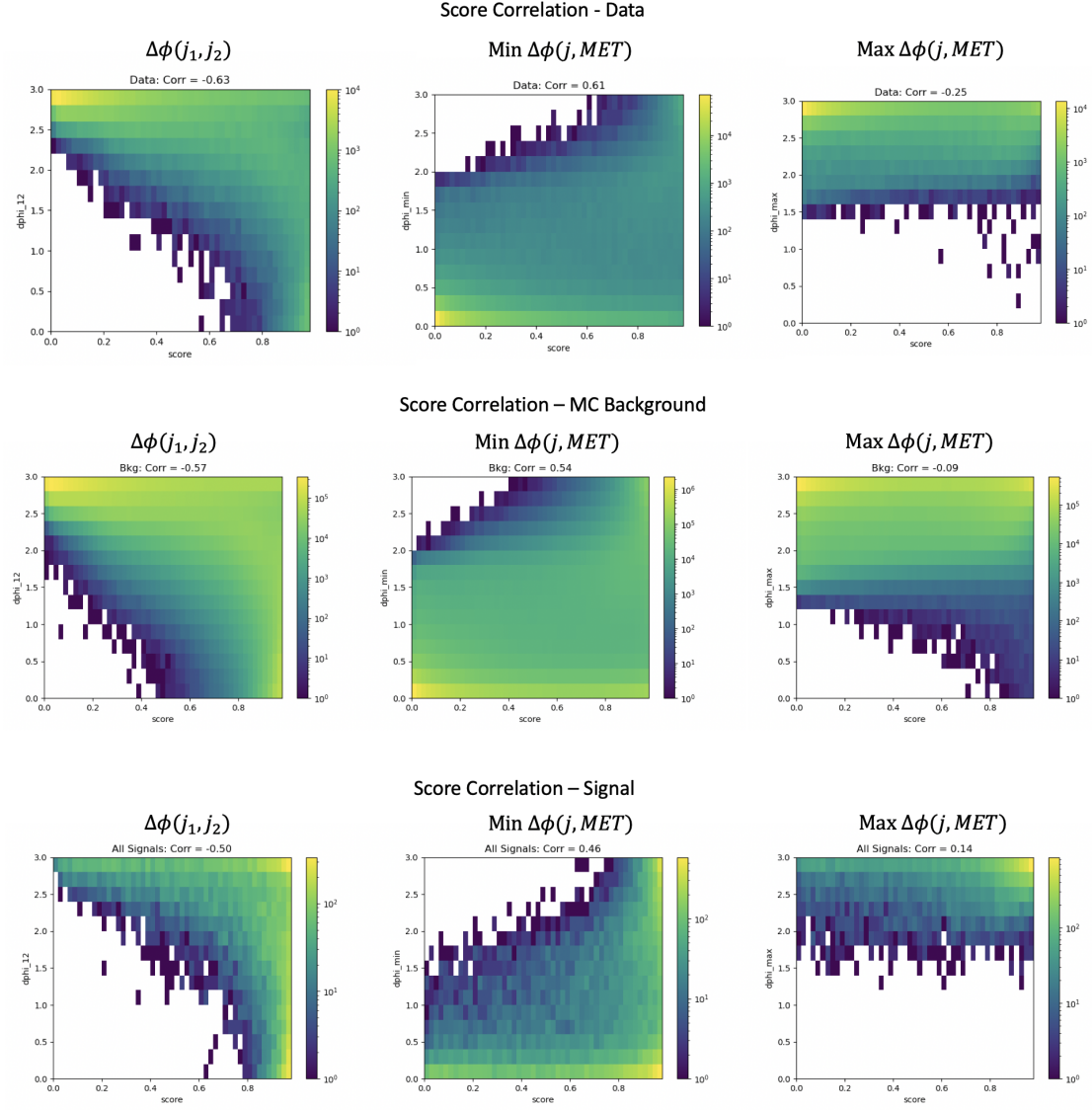


Figure B.9: Correlation between  $\phi$  orientation variables and PFN score

## 2153 B.6 PFN Training Composition

2154 The overall sensitivity and stability across the signal grid is observed to benefit by training  
 2155 the ML tool to reject only the dominant background, QCD. This is evidenced by the PFN re-  
 2156 sponse plots shown in Section 7.1.1 and the following AUC and sensitivity comparison plots in  
 2157 Figure B.11.

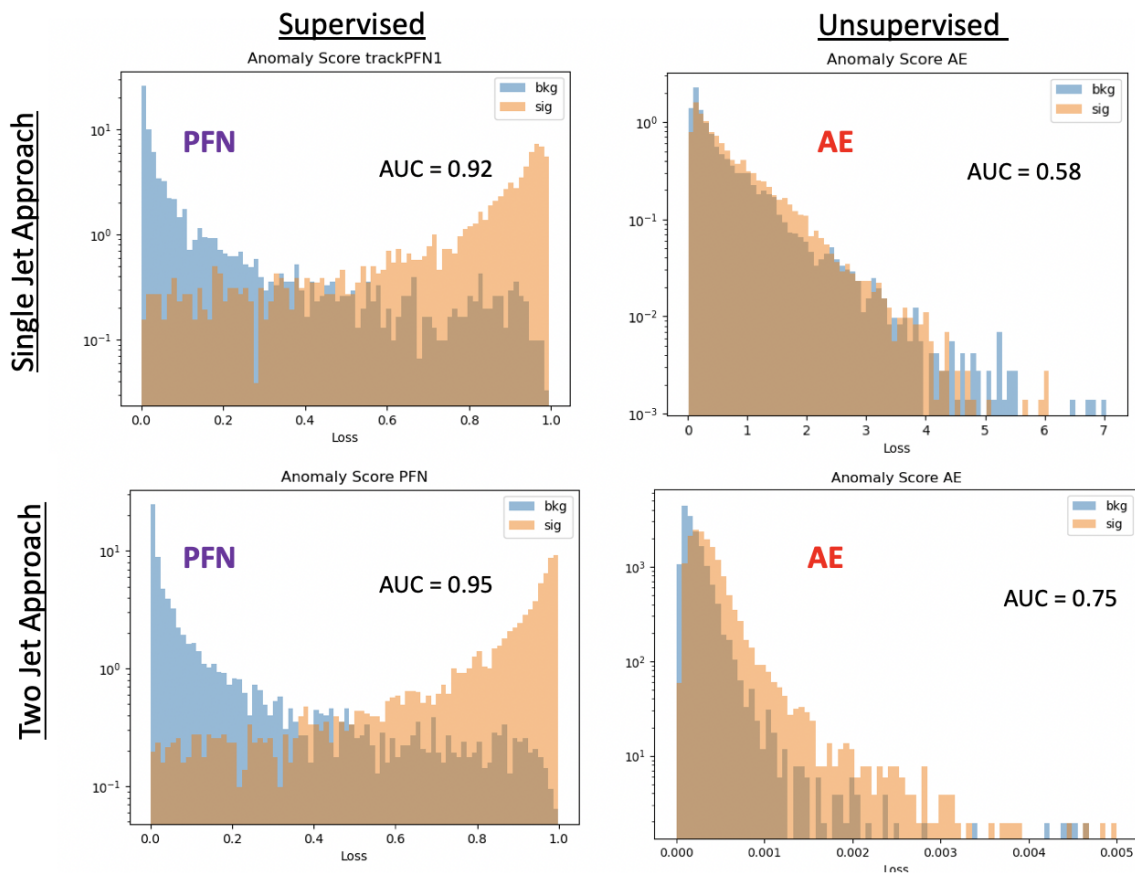


Figure B.10:  $\phi$  Performance comparison between single jet and jet system ML approach

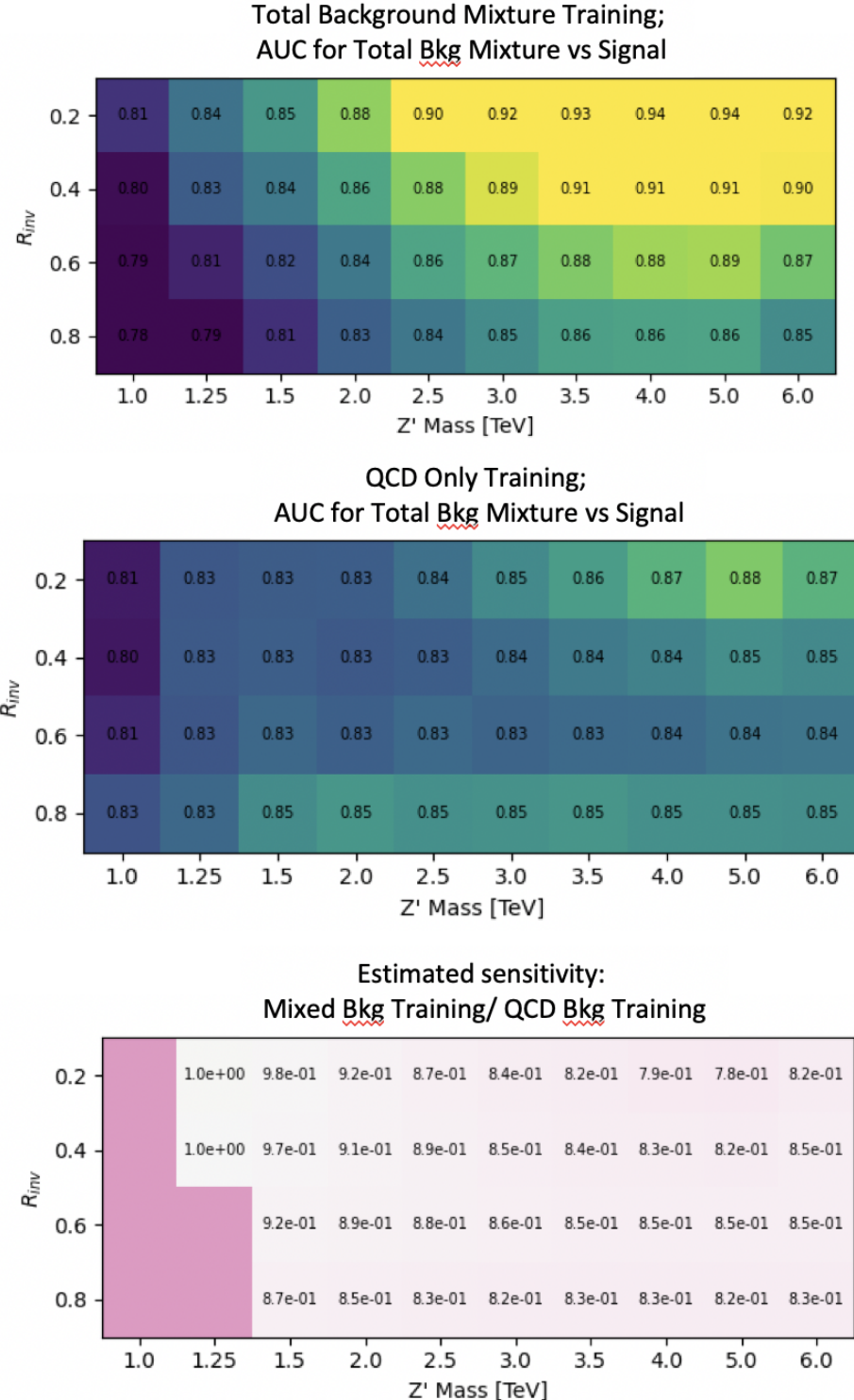


Figure B.11:  $\phi$  Comparison in the AUC score across the grid for the mixed background strategy vs the QCD only strategy. The bottom table highlights that the QCD only strategy gives superior sensitivity across the signal grid.

2158    **B.7  $E_T^{\text{miss}}$  and  $E_T^{\text{miss}}\phi$  Shapes**

2159    The Tight cleaning working point was found to be necessary due to the nature of our signal  
 2160    being  $E_T^{\text{miss}}$  and hadronic activity that are closely aligned, presenting a signature that is very af-  
 2161    fected by beam-induced background (BIB). As per the cleaning recommendations, any event with  
 2162    a jet that fails Tight criteria is rejected. Figure B.12 shows the effect of Tight cleaning on the shape  
 of  $E_T^{\text{miss}}$  in data, fixing a feature present in Loose cleaning only.

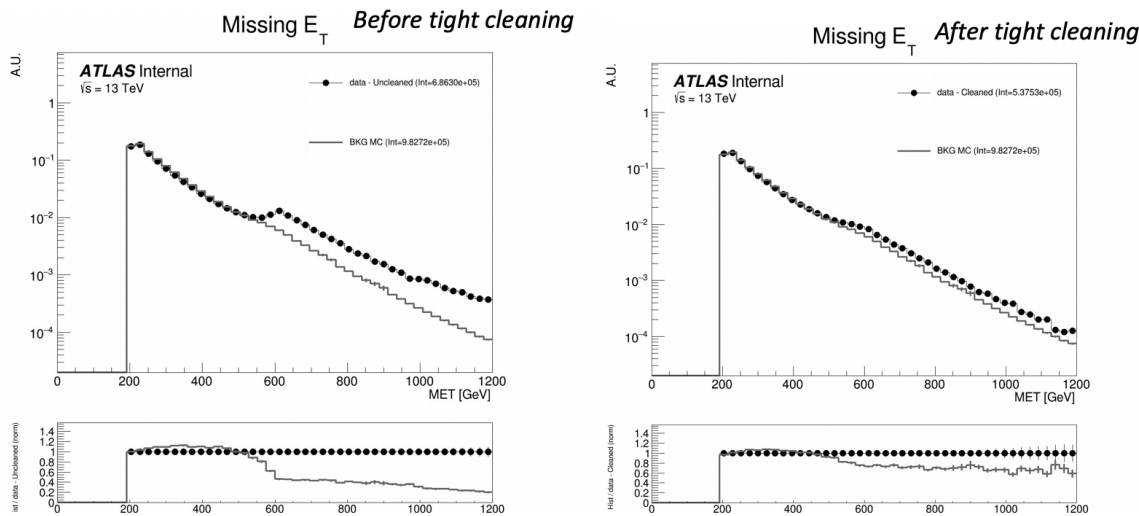


Figure B.12:  $E_T^{\text{miss}}$  in data before and after Tight event cleaning is applied.

2163  
 2164    Figure B.13 further illustrates the correlation between the excess events and the leading jet  $p_T$ ,  
 2165    and illustrates the impact of the tight cleaning in reducing this feature.

2166    Figure B.14 illustrates the 2D  $\eta$  vs  $\phi$  distribution of the leading and subleading jets before and  
 2167    after tight cleaning. No major spikes or hot areas are observed. One bright spot in the subleading  
 2168    jet map at  $\eta \approx 0$  and  $\phi \approx -1.0$  was studied and found to have no impact on the  $E_T^{\text{miss}}$  shape, indicating  
 2169    a likely missed spot in the Tile cleaning which does not affect  $E_T^{\text{miss}}$ .

2170    **B.7.1 NCB Preselection**

2171    A final preselection was derived to entirely remove the presence of non-collision background,  
 2172    particularly noted through its impact on the  $E_T^{\text{miss}}$  shape. Cuts are added on the subleading jet

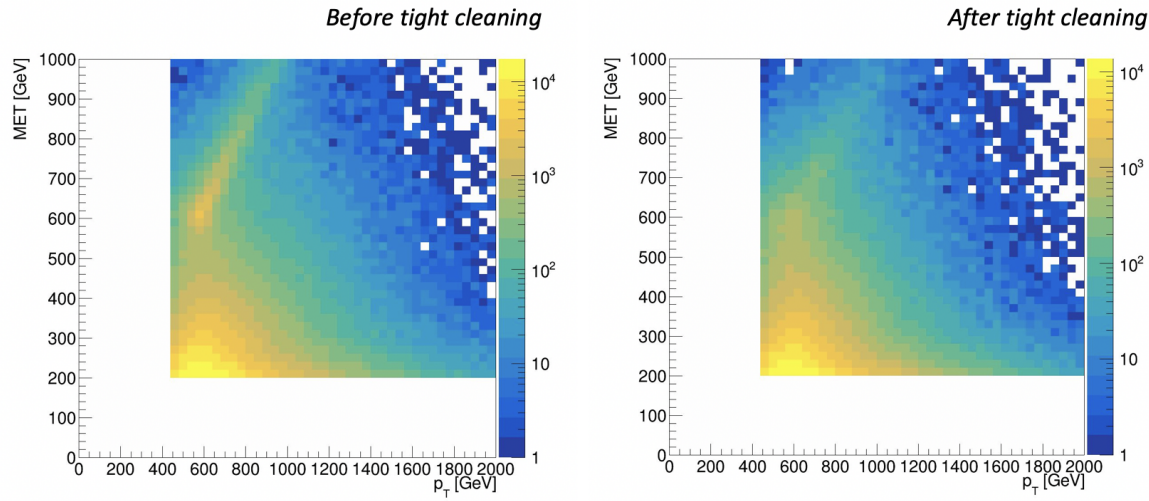


Figure B.13:  $E_T^{\text{miss}}$  vs jet1  $p_T$  in data before and after Tight event cleaning is applied.

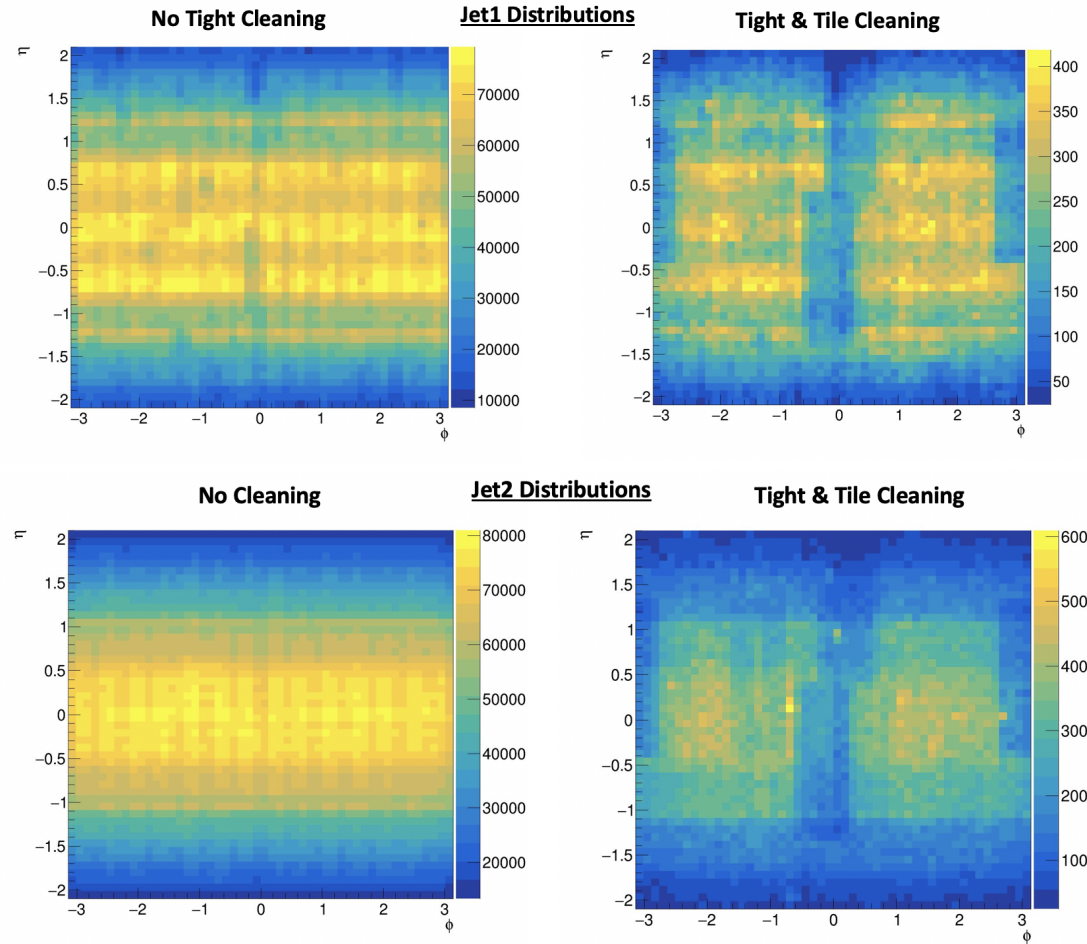


Figure B.14:  $\eta$  vs  $\phi$  for leading and subleading jets, before and after the application of tight cleaning.

2173  $p_T > 150$  GeV and  $\Delta\Phi(j1,j2) > 0.8$ . Figure B.15 shows the impact of these cuts to create a fully  
 2174 smoothly falling  $E_T^{\text{miss}}$  distribution. Figure B.16 shows the impact on the data yields in the CR and  
 2175 VR and several signals in the SR; the greatest inefficiencies are found for the signal points that are  
 2176 not sensitive in the analysis anyway. The reduction in background ultimately means that no impact  
 is noticed on the limits.

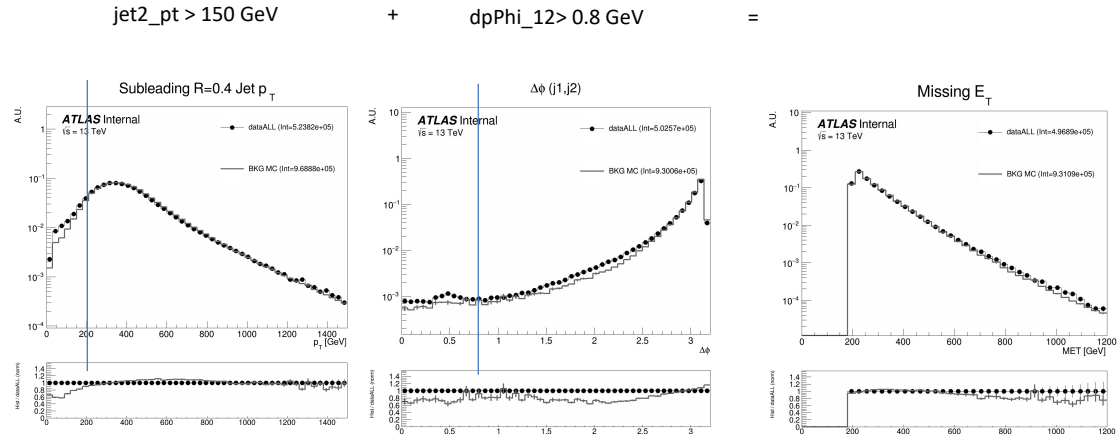


Figure B.15: Added NCB preselection and impact on  $E_T^{\text{miss}}$  shape.

2177  
 2178 Figure B.17 shows the impact of these cuts on the 2D  $E_T^{\text{miss}}$  vs jet1  $p_T$  distribution, where the  
 2179 feature is also observed to be smoothed.

2180 This strategy was discussed and signed off by the Jet/ $E_T^{\text{miss}}$  CP group<sup>1</sup>.

### 2181 B.7.2 TileCal Correction

2182 The  $E_T^{\text{miss}}\phi$  distribution was fixed through the implementation of an offline TileCal correction  
 2183 tool, which removes certain lumiblocks of certain runs based on poor functioning in TileCal mod-  
 2184 ules. Figure B.18 shows the  $E_T^{\text{miss}}\phi$  distribution in data across runs, before and after the application  
 2185 of the tool, showing the ability of the tool to remove spikes due to instrumental problems.

---

<sup>1</sup><https://indico.cern.ch/event/1413217/>

Region	Before Extra Cleaning Cuts	After Extra Cleaning Cuts	Efficiency
Data - CR	108957	107435	0.99
Data - VR	116917	116008	0.99
2500, 0.2 - SR	1921	1709	0.89
2500, 0.4 - SR	1819	1424	0.78
2500, 0.6 - SR	1150	735	0.64
2500, 0.8 - SR	543	251	0.46
5000, 0.2 - SR	21.5	20.3	0.94
5000, 0.4 - SR	22.3	19.4	0.87
5000, 0.6 - SR	16.0	11.6	0.73
5000, 0.8 - SR	8.1	4.1	0.51

Figure B.16: NCB preselection impact on data and signal yields.

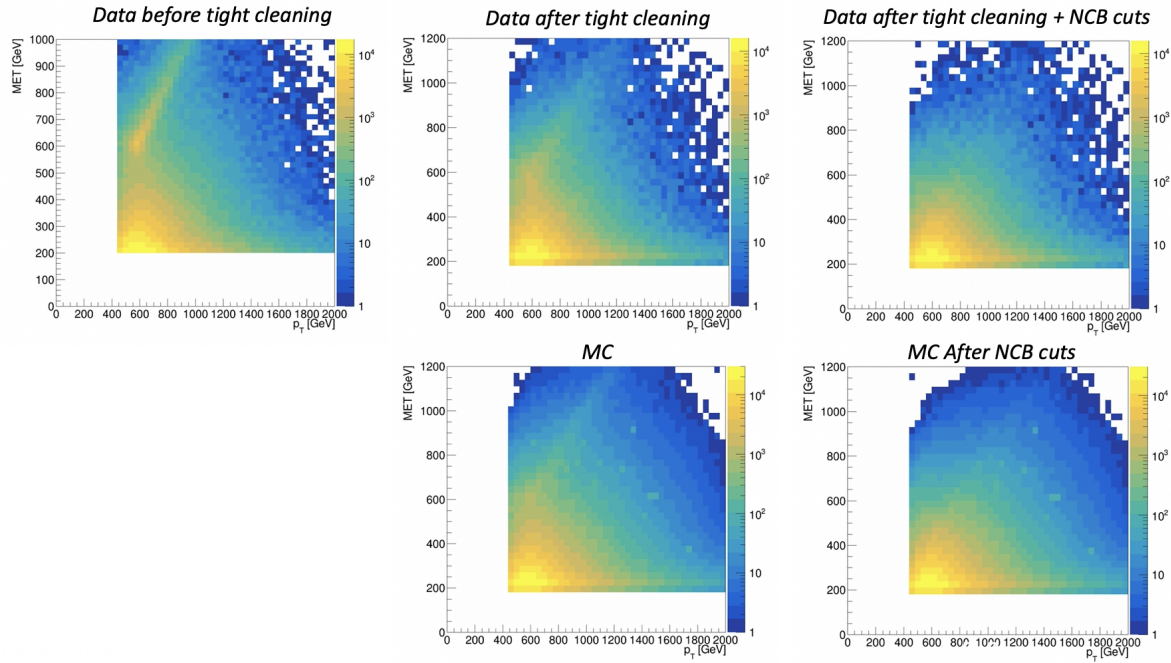


Figure B.17: Impact of tight cleaning and non-collision background preselection.

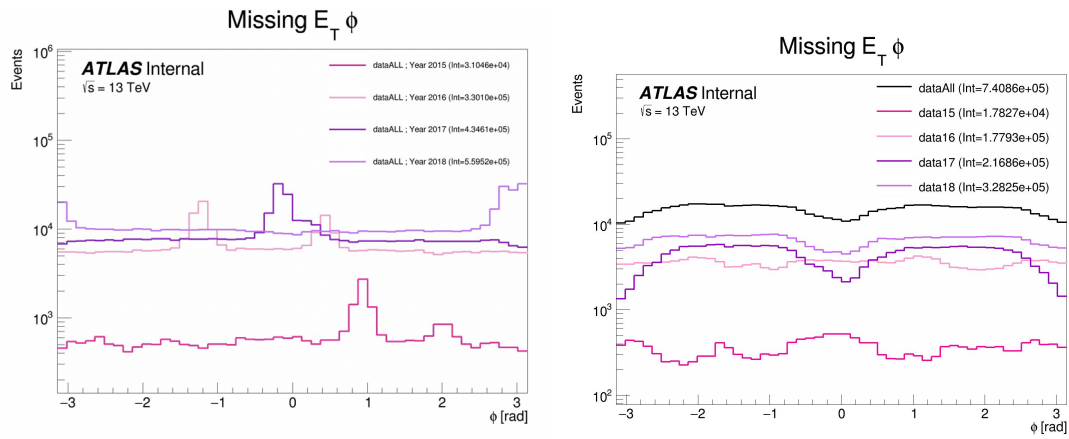


Figure B.18:  $E_T^{\text{miss}}\phi$  in data, before (left) and after (right) application of the TileCal correction tool.

2186

2187

## Appendix C: Truth Studies

### 2188 C.1 Jet dR Matching

2189 Figure C.1 demonstrates that the leading and subleading jet are overwhelmingly the most likely  
2190 jets to be matched to a dark quark.

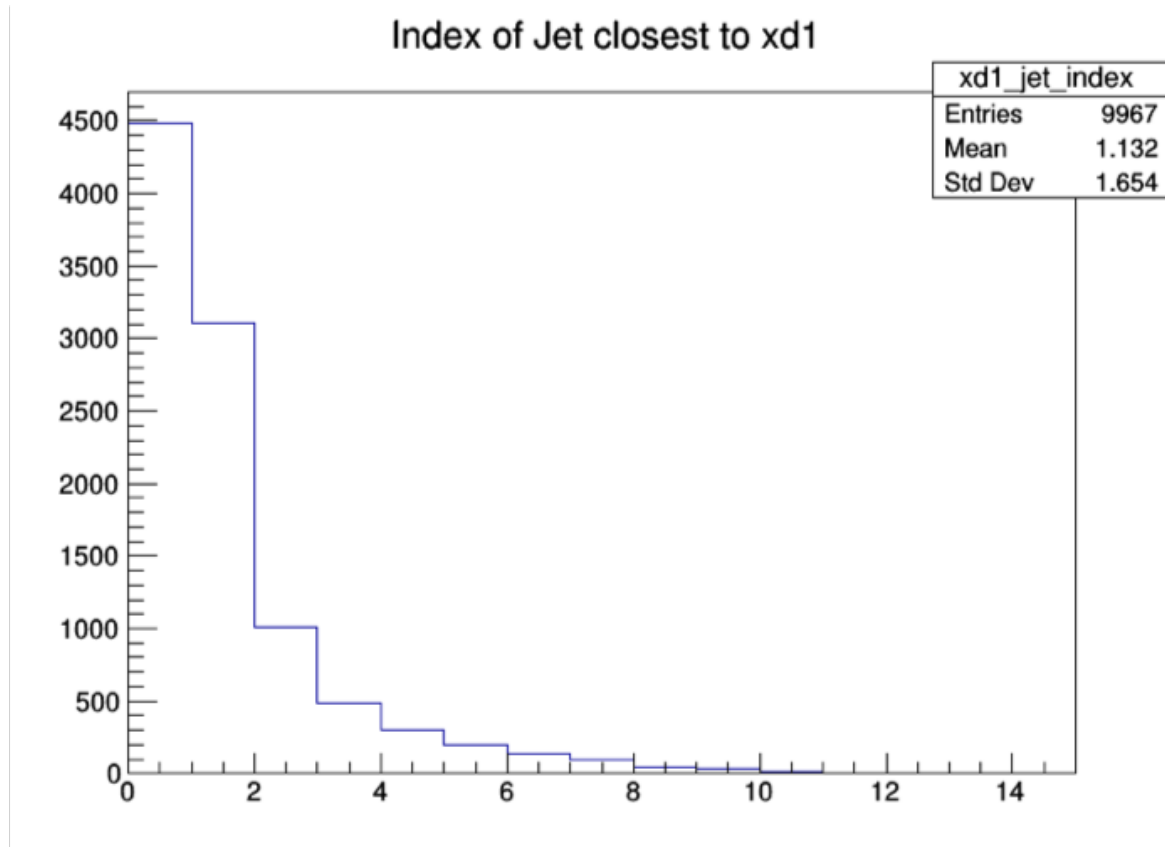


Figure C.1: Index of jets truth matched (by requirement of  $\Delta R < 0.4$ ) with dark quark.

2191 Other matching strategies were explored, such as choosing the jet most aligned with  $E_T^{\text{miss}}(\min$   
2192  $\Delta\phi(j, E_T^{\text{miss}}))$  and the jet most anti-aligned with  $E_T^{\text{miss}}(\max \Delta\phi(j, E_T^{\text{miss}}))$ . However, in most cases  
2193 these two measurements correspond to the subleading and leading jets respectively. Additionally,  
2194 as shown in Figure C.2 the leading/subleading strategy generally results in more matched jets than

2195 the  $E_T^{\text{miss}}$  aligned and  $E_T^{\text{miss}}$  anti-aligned strategy. Therefore the leading and subleading jets were  
 2196 chosen for consideration in this analysis.

<b>Signal (<math>M_{Z'}</math>, <math>r_{\text{inv}}</math>)</b>	<b>% Leading Jets <math>dR</math> Matched</b>	<b>% MET anti- aligned Jets <math>dR</math> matched</b>	<b>% Subleading Jets <math>dR</math> Matched</b>	<b>% MET aligned jets <math>dR</math> matched</b>
750 GeV, 0.2	<b>0.432883</b>	0.3567	<b>0.3777</b>	0.3504
750 GeV, 0.8	<b>0.187819</b>	0.1589	<b>0.1826</b>	0.1803
3500 GeV, 0.2	<b>0.692931</b>	0.5408	<b>0.5097</b>	0.4144
3500 GeV, 0.8	<b>0.344057</b>	0.2927	<b>0.2634</b>	0.2585
6000 GeV, 0.2	<b>0.647237</b>	0.5047	<b>0.4975</b>	0.3919
6000 GeV, 0.8	<b>0.345542</b>	0.2882	<b>0.2517</b>	0.249

Figure C.2: Percent of jets with  $\Delta R(j, E_T^{\text{miss}}) < 0.4$  comparing two jet identification strategies. Leading and subleading jets are seen to be the better metric for identifying jets associated with the dark quark decay.